



**FACULTÉ DES SCIENCES**  
**Institut d'Astrophysique et Géophysique de Liège**

# **COSMIC ANISOTROPIES FROM QUASARS**

## **FROM POLARIZATION TO STRUCTURAL-AXIS**

### **ALIGNMENTS**

Reading Committee:

Prof. Jean René Cudell (promoter)  
Dr. Damien Hutsemékers (co-promoter)  
Prof. Pierre Magain (president)  
Dr. Dominique Sluse (secretary)  
Dr. Maret Einasto  
Dr. Olaf Wucknitz

Année Académique 2015–2016

Dissertation présentée par  
Vincent PELGRIMS  
en vue de l'obtention du grade  
de Docteur en Sciences



*Je sais que, curieusement, ceci a un sens et qu'on peut  
s'amuser à voir jusqu'où on comprend,  
comme par-dessus les cols.*

ITO NAGA



# Contents

<b>Acknowledgments</b>	<b>vii</b>
<b>Résumé</b>	<b>ix</b>
<b>Abstract</b>	<b>xi</b>
<b>Introduction</b>	<b>1</b>
<b>1 Dedicated statistical methods</b>	<b>11</b>
1.1 The S and Z tests . . . . .	11
1.1.1 The S test . . . . .	11
1.1.2 The Z test . . . . .	13
1.1.3 One-free-parameter statistics and its physical interpretation . . . . .	15
1.1.4 Coordinate dependence of the S and Z test results . . . . .	17
1.1.5 Parallel transport for coordinate invariance . . . . .	18
1.1.6 Generation of simulated data sets . . . . .	22
1.2 The polarization cap test . . . . .	25
1.2.1 A new coordinate-invariant statistical test for polarization data . . . . .	27
1.2.2 Construction of the probability distribution . . . . .	29
1.2.3 A fast algorithm for generating the $P_n$ . . . . .	31
1.2.4 A first example . . . . .	34
1.2.5 Further refinements of the method . . . . .	35
1.2.6 The PC test: conclusion . . . . .	39
1.3 The Hawley–Peebles Fourier method . . . . .	40
<b>2 Analysis of quasar optical polarization alignments</b>	<b>43</b>
2.1 Full sample . . . . .	44
2.2 Redshift dependence . . . . .	45
2.2.1 Fine structure and best regions . . . . .	49
2.2.2 A possible cosmological alignment . . . . .	50
2.2.3 A naive interpretation . . . . .	50

2.3	Concluding remarks . . . . .	51
<b>3</b>	<b>A search for quasar radio polarization alignments</b>	<b>53</b>
3.1	Data sample . . . . .	54
3.2	Uniformity of radio-polarization PAs . . . . .	56
3.2.1	Regions of optical polarization alignments . . . . .	56
3.2.2	Full sky coverage . . . . .	59
3.2.3	Intermediate outcomes . . . . .	64
3.3	Identification of regions of aligned polarizations . . . . .	67
3.4	Interpreting the results . . . . .	72
3.4.1	Are the data contaminated? . . . . .	72
3.4.2	Are the polarization alignments real? . . . . .	76
3.5	Concluding remarks . . . . .	76
<b>4</b>	<b>Alignment of quasar polarizations with LSS</b>	<b>79</b>
4.1	Observations and polarization measurements . . . . .	81
4.2	Analysis of polarization alignments . . . . .	83
4.3	Conclusion on optical polarization alignments in LQGs . . . . .	88
<b>5</b>	<b>Quasar radio polarizations align with LQGs</b>	<b>91</b>
5.1	Data samples and premises . . . . .	92
5.1.1	Faraday contamination . . . . .	95
5.2	Position angles of LQGs . . . . .	97
5.3	Correlation between polarization and LQG PAs . . . . .	98
5.3.1	Morphological position angles and their uncertainties . . . . .	101
5.4	Discussion . . . . .	102
5.5	Concluding remarks . . . . .	105
	<b>Conclusion and outlook</b>	<b>111</b>
	<b>Bibliography</b>	<b>117</b>

# Acknowledgments

I would like to warmly thank my promoter Prof. Dr. Jean René Cudell, Associate Professor at the University of Liège, for his valuable cooperation and wisdom all along this exciting doctoral thesis. I am also particularly indebted to my co-promoter Dr. Damien Hutsemékers, Senior Researcher Associate at F.R.S.-FNRS, for his assistance and cooperation. It was a real pleasure to collaborate with them and with Dominique Sluse and Lorraine Braibant, whose own research in the field provided an invaluable resource. My thanks to them for their extended awareness and responsiveness.

I extend my sincere thanks to the members of my reading committee: Dr. Maret Einasto, Senior Research Fellow at Tartu Observatory, Prof. Dr. Pierre Magain, Professor at the University of Liège, Dr. Dominique Sluse, Post-doctoral Researcher at the University of Liège and Dr. Olaf Wucknitz, Scientific Staff at the Max-Planck-Institut for Radioastronomy in Bonn, for their careful reading of the text and the constructive criticism they will provide me with.

I am grateful to the scientific community of the Department of Astrophysics, Geophysics and Oceanography and especially the members of the Fundamental Interactions in Physics and Astrophysics group for inspiring discussions about physics and life during coffee breaks.

I further express my warmest gratitude to all the members of my (extended) family and my close friends for their enduring support. My final thanks go to my dear fiancée, Lou, for her immeasurable support, encouragement and comprehension.





# Résumé

La comparaison des orientations des vecteurs de polarisation de la lumière visible provenant de quasars séparés par des milliards d'années-lumière a mené à une découverte surprenante. Ces vecteurs sont alignés au lieu d'être orientés aléatoirement comme on pouvait s'y attendre. La découverte de ces corrélations qui impliquent des échelles de l'ordre du gigaparsec a été confirmée et renforcée par de nouvelles observations et de nouvelles analyses. À ce jour, cependant, aucun scénario n'a pu rendre compte de ces corrélations de manière satisfaisante.

Nous avons dédié cette thèse de doctorat à l'étude minutieuse de ces observations qui se révèlent être potentiellement en désaccord avec le modèle cosmologique actuel. Il nous a semblé important de confirmer de façon indépendante ces alignements à grande échelle qui n'avaient été caractérisés qu'à l'aide des deux mêmes méthodes statistiques. À cette fin, nous élaborons une nouvelle méthode statistique dans le Chapitre 1. Celle-ci est dédiée à l'analyse et à la caractérisation de la distribution de vecteurs axiaux perpendiculaires aux lignes de visée d'un échantillon de sources dispersées sur la sphère céleste. Cette nouvelle méthode statistique nous permet, dans le Chapitre 2, de confirmer indépendamment la présence des alignements à grandes échelles des vecteurs de polarisation optique des quasars, mais aussi de redéfinir objectivement les régions d'alignement. Nous dédions le Chapitre 3 à une analyse détaillée d'un échantillon de données polarimétriques obtenues en longueur d'onde radio. Celle-ci révèle le même genre d'alignement des vecteurs de polarisations. Les régions du ciel dans lesquelles se concentrent les alignements radio se trouvent au voisinage de celles définies dans le visible. Ceci suggère que les axes des quasars eux-mêmes pourraient être alignés. Afin d'explorer cette possibilité, nous analysons dans le Chapitre 4 de nouvelles données de polarisation obtenues pour des quasars se trouvant dans deux grands amas de quasars. En tenant compte du lien entre l'orientation des vecteurs de polarisation optique et l'orientation des quasars par rapport à la ligne de visée, nous concluons que les axes de rotation des trous noirs supermassifs situés au centre des quasars sont alignés avec la structure de l'amas auquel ils appartiennent. Dans le Chapitre 5, nous confirmons notre découverte en utilisant un échantillon d'amas de quasars et des mesures de polarisation radio. Nous observons également que l'orientation préférentielle des axes de rotation des trous noirs supermassifs dépend de la richesse de l'amas de quasars dans lequel ils sont contenus.

L'ensemble de ces résultats suggère que les alignements à très grandes échelles des vecteurs de polarisation des quasars soient liés aux corrélations au sein des amas de quasars.

Ces corrélations qui seraient elles-mêmes dues aux alignements des axes de rotation des trous noirs dans la toile cosmique.

# Abstract

The comparison of the orientations of the optical-polarization vectors of quasars that are separated by billions of light-years has led to the striking discovery that they are aligned instead of pointing in random directions as expected. This discovery has been confirmed and the significance of the correlations enhanced but no satisfactory scenario has been provided so far to account properly for the specificities of these gigaparsec-scale correlations.

We devoted this doctoral thesis to an in-depth analysis of these observations that may constitute an anomaly to the current cosmological paradigm. As the large-scale polarization alignments had always been characterized through the two same statistical methods, we found it important to independently confirm them. Therefore, in Chapter 1, we develop a new and independent statistical method which is dedicated to the study and the characterization of the distribution of the orientations of vectorial quantities that are perpendicular to the lines of sight of a set of sources spread on the celestial sphere. This allows us, in Chapter 2, to confirm independently the large-scale optical-polarization-vector alignments and, further, to refine the limits of the aligned regions through an unbiased characterization of the signal. In Chapter 3, we provide a detailed analysis of a large sample of polarization measurements made at radio wavelengths. We report on similar polarization-vector alignments. The regions of alignments of the quasar-radio-polarization vectors are found to be close to the regions of optical alignments. This suggests that quasar axes themselves could be aligned. Thus, in Chapter 4, based on new observations, we analyse the optical-polarization vectors of quasars that belong to two large groups. Taking into account the link between the optical-polarization vectors and the morphologies of the quasars, we find that the spin axes of the supermassive black holes located at the centres of quasars align with the axis of the large-quasar group to which they belong. We use radio-polarization data to reinforce our findings in Chapter 5 where we consider a sample of quasar groups drawn from the Sloan Digital Sky Survey. We additionally find that the preferred orientations of the spin axes of the supermassive black holes depend on the richness of their host large-quasar groups.

These results suggest that the very-large-scale alignments of quasar-polarization vectors and the correlations with the large-quasar groups could be due to the alignments of the supermassive black hole spin axes within the cosmic web.



# Introduction

Cosmology is the part of science that aims at the understanding of the working of the Universe as a whole. The main pillar of the current standard cosmological model, the cosmological principle, states that the Universe has to be isotropic and homogeneous when it is viewed at sufficiently large scales. The philosophical reason for this assumption is the generalized Copernican principle which states that there is no privileged observer in the Universe. This implies that the part of it which we can observe and study is a representative sample of its entirety and that its components, their properties and the physical laws at play have to apply throughout, whoever is observing from wherever. Fundamentally, the cosmological principle requires that the physics is the same in every reference frame. Naturally, general relativity has proven to be the favoured framework within which scientists can build a theory that fairly describes the Universe in its entirety. Provided with the cosmological principle, the Friedman-Lemaître-Robertson-Walker model stemmed from this theory and was shown to be the most suitable model to account for our world. Following this description, we live in a three-plus-one dimensional space filled with particles and radiation that interact with each other. Throughout the years, astronomers and astrophysicists have noticed that our Universe is expanding, emerging from a singularity called the Big-Bang, that it is mainly filled by unseen matter, the still elusive dark matter, and that its expansion is accelerated by a positive cosmological constant covering an unknown component of negative pressure acting as a vacuum energy, the dark energy.

Consequently, cosmologists and astrophysicists ended up with the standard cosmological model often referred to as the  $\Lambda$ CDM model, where the  $\Lambda$  stands for the cosmological constant and the CDM for the cold dark matter. Recent studies of the cosmic microwave background (CMB), the relic radiation of the hot and dense phase of the early Universe, have shown that this model works fairly well at explaining these data. However, given this representation of the cosmos, more than ninety five per cents of its energy content remain unknown. In a sceptical sense, the  $\Lambda$ CDM cosmological model turns out to be a very convincing parametrization of our ignorance and most of Nature is still part of our incomprehension.

In agreement with the theory and the cosmological principle, the relic CMB radiation is found to be very isotropic and amazingly homogeneous, but also seeded by sparse temperature fluctuations. Those mark small under- and over-densities of the early maelstrom. Under

the pull of gravity, these inhomogeneities have grown to form the voids and the clusters and superclusters of galaxies that we observe in our neighbouring Universe. The galaxies in the Universe are indeed not evenly distributed through space but rather form a cosmic web composed of filaments and clumps around huge voids where galaxies are scarce. This wonderful arrangement of the matter distribution forms what is called the large-scales structures of the Universe. However, when viewed on sufficiently large scales, i.e. when a sufficiently large fraction of the cosmos is considered, the cosmological principle tells us that the overall distribution has to be homogeneous and isotropic. The study of the (observable) matter distribution, which is highly inhomogeneous and anisotropic at small scales ( $\lesssim 100$  Mpc), also helps refine our understanding of the whole picture. However, as the samples of galaxies and other objects have become larger and deeper in the distant Universe, large-scale structures of a size comparable to that of the studied samples have always been found. These inhomogeneities are sometimes able to challenge the cosmological principle. These studies thus stress the importance of getting more complete and deeper data sets in order to examine robustly the distribution of matter and, perhaps, to refine our knowledge. However, the further away the galaxies, the fainter they appear, which makes the large-scale structures of the young –or distant– Universe difficult to study. In this regard, galaxies harbouring very bright active galactic nuclei, and especially quasars, are a promising tool as they can be observed at the far reaches of the cosmos and thus they could be used to trace the evolution of the matter distribution over very large scales. What makes the nuclei of certain galaxies active, i.e. very luminous, is the accretion of the inner material of these galaxies into the massive black hole located at their centre. Quasars are the most energetic members of this class of extragalactic objects. It is remarkable, though, that even in large samples of such bright sources that become available nowadays, incredibly large systems have been observed and their nature, while still controversial, could constitute a serious anomaly for the cosmological paradigm.

Beside the large-scale anisotropies in the space distribution of these galaxies harbouring active nuclei, other intriguing observations are available and some could potentially compete with our current view of the Universe. One of these concerns the polarization of the light emitted from quasars. Indeed, more than seventeen years ago, Hutsemékers reported on large-scale anisotropies of the orientations of the polarization vectors of quasars. These correlations involve sources separated by amazingly huge distances. Until now and despite the variety of models that have been proposed, none have been able to provide a satisfactory scenario to account for these observations, which might consequently challenge the cosmological principle. We can present these unexplained observations as follow.

## The anomaly

When studying the polarization of an electromagnetic wave emitted by a source, a polarization vector is defined in the plane orthogonal to the propagation direction of the wave, the line of sight. When the directions of the oscillating electric fields composing the light

beam are not isotropically distributed in that plane, the radiation is said to be partially or fully polarized and the polarization vector has a non-vanishing norm which reflects the degree of linear polarization of the waves. The direction of the polarization vector with respect to an arbitrary direction defines the polarization position angle. In astronomy, the arbitrary direction is often chosen as being the North-South axis of the equatorial coordinate system and the position angles are counted positively in the East-of-North convention. The study of the polarization of the light from astronomical source allows us to infer the geometrical arrangement of their components and, in general, to probe their orientation even when these objects are too far to be resolved by telescopes. The analysis of the polarization is thus a powerful tool in astronomy.

Regarding polarization studies of extragalactic sources, there have been puzzling observations that could potentially have cosmological importance. In 1998, Hutsemékers reported on the striking observation that the polarization vectors of the visible light from luminous active galactic nuclei<sup>1</sup> separated by cosmological distances are coherently oriented in certain regions of space. This analysis, originally presented in (Hutsemékers 1998), was based on a sample of 170 quasars compiled from the literature and carefully selected in order to eliminate at best the contamination by our hosting Milky Way. Since the discovery of the regions of polarization alignments, dedicated observational campaigns have been conducted and the present sample is composed of 355 quasars with high-quality polarization measurements at optical wavelengths (Lamy & Hutsemékers 2000; Hutsemékers & Lamy 2001; Sluse et al. 2005 and Hutsemékers et al. 2005). With the latest sample, statistical tests that study the coherence of the polarization position angles in groups of neighbouring sources show that the observed correlations have probabilities between  $3 \times 10^{-5}$  and  $2 \times 10^{-3}$  to be due to chance (Hutsemékers et al. 2005). The probabilities depend on the chosen test as they are not equally sensitive to the same alignment patterns. We shall summarize below the main characteristics of the anisotropies in the orientations of the optical polarization vectors from quasars.

### Alignment regions

The anisotropies of the orientations of the polarization vectors involve quasars that are grouped in three distinct regions of the three-dimensional comoving space. These comoving regions, two located in the North Galactic Cap and one in the South Galactic Cap, are found towards two regions of the sky that are roughly antipodal. While the borders of these regions are loosely determined due to the (observational) inhomogeneous character of the data set, they are defined in redshift and equatorial coordinates as

- $168^\circ \leq \alpha \leq 218^\circ$ ;  $\delta \leq 50^\circ$  and  $0.0 \leq z \leq 1.0$
- $168^\circ \leq \alpha \leq 218^\circ$ ;  $\delta \leq 50^\circ$  and  $1.0 \leq z \leq 2.3$  (A1)

---

<sup>1</sup>Throughout this work and unless specified, we will referred to active galactic nuclei as quasars, regardless of the observational specificities that make the latter class more restrictive.

- $320^\circ \leq \alpha \leq 360^\circ$ ;  $\delta \leq 50^\circ$  and  $0.7 \leq z \leq 1.5$  (A3)

where  $\alpha$ ,  $\delta$  and  $z$  are the right ascension, the declination and the cosmological redshift, respectively.

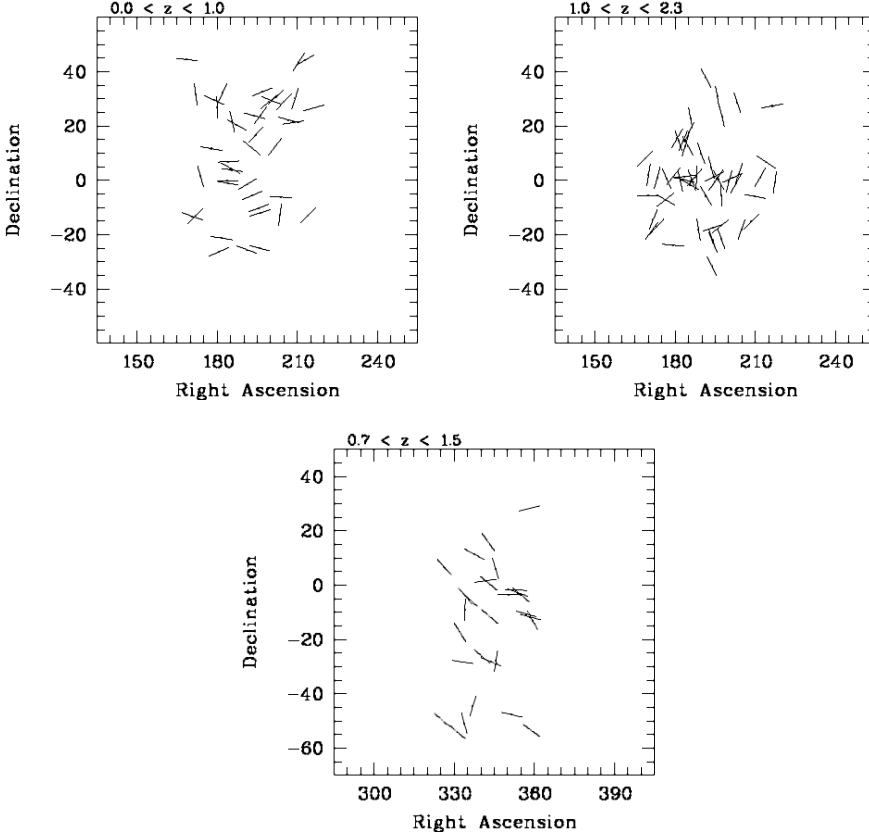


Figure 1: Maps of quasar polarization vectors in the North Galactic Cap (*top*) and in the South Galactic Cap (*bottom*). The dots represent the quasars and the segments the normalized polarization vectors. Coherent orientations are visually detectable in each of these regions of the comoving space. The regions illustrated are the A1 region (*top right*), its low-redshift counterpart (*top left*) and the A3 region (*bottom*). Figures taken from Hutsemékers et al. (2005).

These regions are illustrated in Fig. 1 where the dots represent the quasars and the segments the normalized polarization vectors. For historical reasons, the region of the South Galactic Cap is referred to as the A3 region while the region called A1 is the high-redshift region of the North Galactic Cap, the “A” standing for alignment. Note that in the original paper of 1998, there was an A2 region defined as  $150^\circ \leq \alpha \leq 250^\circ$ ;  $\delta \leq 50^\circ$  and  $0.0 \leq z \leq 0.5$  which is somehow included in the low-redshift part of the data set towards the same region of the sky as A1. The A2 region has been dropped because of the adopted



observational strategies to increase the sample size from 1998 to 2005. As we will see in Section 2.2.1, though, the alignment in this region is still there.

Based on the very fact that the A1 and A3 regions are roughly opposite on the sky, Hutsemékers et al. (2005) defined the A1–A3 axis as the combination of the two sky windows pointing towards these regions. Statistical tests have shown that most of the alignment

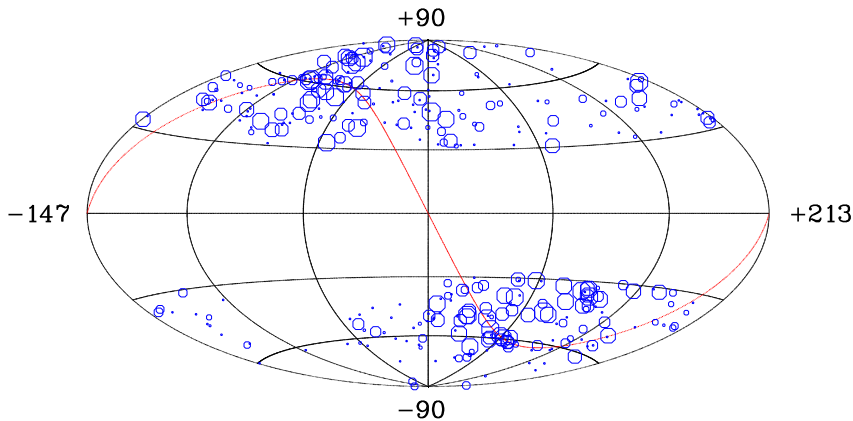


Figure 2: Hammer-Aitoff projection of the quasar positions on the sky, in Galactic coordinates. The 355 objects are plotted. The radius of the circles is given by  $\rho_i \propto \exp s_i - 0.9$ , where  $s_i$  refers to the statistics defined in Section 3.3 from Eq. 1.10 for the Z test with parallel transport correction and  $n_v = 40$  (see Section 1.1). The larger the circle, the more significant the alignment at that point. The superimposed red line gives the location of the celestial equator. Figure taken from Hutsemékers et al. (2005).

It is worth noting that the direction defined by the A1–A3 axis points roughly towards the Virgo cluster. Other large-scale anisotropies have been reported towards the same direction. They include the alignment of the directions towards which the amplitudes of the low-multipoles of the cosmic microwave background are significantly suppressed (e.g., Tegmark et al. 2003; Planck Collaboration XXIII 2014), the direction of the strongest anisotropy in the offset angles of radio galaxy symmetry axes relative to their average polarization angles (Jain & Ralston 1999) and the directions of maximum accelerating expansion rate of the Universe inferred from the Union2 Supernova type Ia data set (Antoniou & Perivolaropoulos 2010). The coincidental alignment of these axes of anisotropies drawn from different probes, including the quasar-optical-polarization alignments, has been questioned by several authors (e.g., Ralston & Jain 2004; Land & Magueijo 2007 and Antoniou & Perivolaropoulos 2010).

## Redshift dependence

The preferred orientations with respect to which the polarization vectors concentrate differ for the three regions of alignments. The mean polarization position angles are  $79^\circ$  for the low- $z$  counterpart of the A1 region,  $8^\circ$  for the A1 region and  $128^\circ$  for the A3 region. The redshift dependence of the anisotropies, which can be observed by comparing the low- and high-redshift parts of the window towards the A1 region in Fig. 1, was further tested by Hutsemékers et al. (2005). Concentrating on the 183 quasars that belong to the A1–A3 axis, the authors potentially unveiled an overall rotation of the mean polarization PA with respect to the redshift of the sources. This significant trend, which is illustrated in Fig. 3, might suggest that the mechanism responsible for the anisotropic patterns is of cosmological nature.

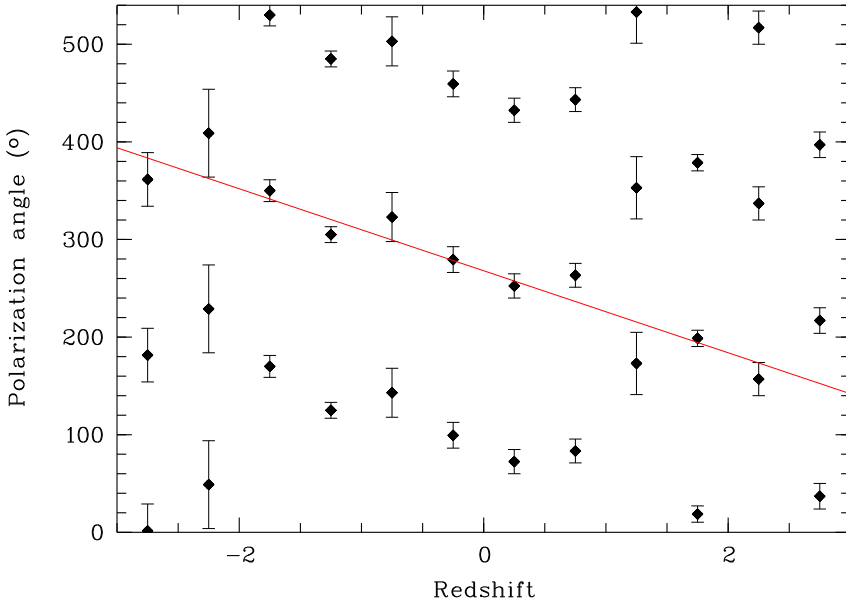


Figure 3: The quasars polarization angles, averaged over redshift bins  $\Delta z = 0.5$ , as a function of the redshift. Redshifts are counted positively for object located in the North Galactic Cap and negatively for those on in the South Galactic Cap. Only the 183 quasars belonging to the A1–A3 axis are considered. Error bars represent 68 % angular confidence intervals for the circular mean (Fisher 1993); they must be seen with caution when the number of quasars per redshift bin is small, i.e. at large  $z$ . Data points are replicated at  $(z, \bar{\psi})$ , at  $(z, \bar{\psi} + 180^\circ)$  and at  $(z, \bar{\psi} + 360^\circ)$ . The fitted red line is given by  $\bar{\psi} = 268^\circ - 42^\circ z$  (see Hutsemékers et al. 2005 for details). Figure taken from Hutsemékers et al. (2005).

## Surviving possible biases

The redshift dependence of the importance of the anisotropies and of the preferential directions constitutes the most stringent argument against potential biases of the polarization data. Indeed, as was extensively discussed in (Hutsemékers 1998; Hutsemékers & Lamy 2001; Sluse et al. 2005; Hutsemékers et al. 2005), Galactic dust contamination through dichroism is unable to account for all the anisotropies. Specifically, if one tries to cancel the alignment in one of the regions by correcting the polarization measurements from quasars to account for an hypothetical (strong) Galactic dust (de)polarization, then, inevitably, one would produce new (or stronger) alignments in the same field but at other redshift(s). Furthermore, it is worth mentioning that the cut in the degree of linear polarization ( $p_{\text{lin}} \geq 0.6\%$ ) has been introduced while defining the sample especially to ensure limited contamination from the Galactic interstellar medium. The cut in Galactic latitude ( $|b_{\text{gal}}| \geq 30^\circ$ ), which can be readily observed in Fig. 2, was introduced for the same reason. Beside, an instrumental bias is also unlikely as approximately half of the sample comes from different surveys and instruments compiled in Hutsemékers (1998). Nevertheless, even if that would be the case, instrumental bias would produce preferred polarization position angles at the particular values of  $0^\circ$  and  $90^\circ$ , inconsistent with the reported ones. The reason is that, at optical wavelengths, the detectors and the optics are usually oriented following the North-South axis, whatever the pointing direction.

## Search for the underlying mechanism

Several scenarios were proposed to explain the large-scale anisotropies of the optical-polarization-vector orientations from quasars. One can consider two main classes of models. Either the quasar polarization orientation is modified along the line of sight, or the structural axes of the sources involved in the observed anisotropies are coherently oriented among themselves over cosmological scales, as the position angles of the optical polarization vectors and the morphological axes of quasars are known to be correlated.

**Photon path effects** There are two different types of physical phenomena that may describe the propagation effects that could produce the observed polarization vector alignments.

**Polarization state modulation** The observations might be explained through models that affect the polarization state of the light during its travel towards Earth. The effects that belong to this category are those that lead to an effective degree of linear polarization towards a specific direction through, e.g., anisotropic absorption or emission of the electromagnetic waves. A mechanism that leads to an anisotropic redistribution of the directions of the incoming electric vector fields would also be part of this category.

**Polarization vector rotation** One might think that the intrinsic polarization state of the sources are not altered along the path from the source to the observer but, instead, that the polarization vectors are rotated by an underlying mechanism that produces the correlations. In order to produce an alignment, though, it is required that the rotation happens asymptotically towards a preferential direction. As already mentioned in (Hutsemékers et al. 2005), a Universe in anisotropic expansion could induce polarization vectors to be coherently oriented through the Brans mechanism (Brans 1975).

**Quasar structural axes alignments** There is observational evidence for correlations between the orientations of the optical polarization vectors and the morphological axes of quasars (e.g., Rusk 1990; Impey et al. 1991; Smith et al. 2004). An immediate alternative to mechanisms acting along the line of sight is therefore the assumption that the polarization alignments actually reflect alignments of the structural axes of quasars over cosmological scales ( $\sim 1$  Gpc).

## Status in 2012

It is clear that the possible scenarios discussed above lead to different characteristics of the anisotropic polarization patterns. For instance, the detection of a wavelength dependence of the alignment features would clearly help to differentiate models. It is in this regard that searches for the same kind of anisotropies in the distribution of the orientations of the polarizations from extragalactic sources have been made at radio wavelengths by Joshi et al. (2007). Based on a large sample of flat-spectrum radio sources, these authors did not find any evidence for coherently oriented polarization vectors, even towards the regions of alignments at optical wavelengths.

Some models can be discarded if the alignment mechanism is wavelength dependent. The assumption that a cosmic anisotropic expansion underlies the observed polarization anisotropies is unlikely. This is true for every other scenarios involving wavelength-independent rotation of the polarization vectors. The scenario in which the quasar morphological axes are aligned is also disfavoured because of the non-detection of polarization alignments at radio wavelengths. Indeed, given that there are (observational) relations between the orientations of the quasar morphological axes and the polarization vectors, not only at optical wavelengths but also at radio wavelengths (e.g., Rusk & Seaquist 1985), one would expect to observe alignments of the polarization vectors in both data sets. This is true even if the correlations are expected to be present at slightly different levels due to the specificity of the relation between morphological axes and polarization vectors for each spectral band (Rusk & Seaquist 1985).

As a consequence, the models implying a wavelength-dependent modulation of the polarization states of the light during its travel to Earth gained some credits. Among such models is the hypothetical and elusive axion-like particles that have been considered as the most

serious candidate for a time (e.g., Das et al. 2005; Agarwal et al. 2011; Payez et al. 2008). However, this scenario has been discarded from the possible explanations for the large-scale polarization alignments at optical wavelengths (Payez, Cudell & Hutsemékers 2011). The principal reason is that this model predicts non-negligible circular polarization which is not observed (Hutsemékers et al. 2010).

Convinced that the study of this anomaly could help at a better understanding of the cosmology, I dedicated my doctoral thesis to a detailed analysis of the large-scale polarization alignments from quasar light that did not find a satisfactory explanation. Rather than proposing various scenarios and testing them against the observations, this work is driven by the data. We adopted a phenomenological approach in the sense that we attempted to extract from the observations as much information as possible in order to draw the most general picture of these anisotropies. However, as we shall see throughout this thesis, our investigations are often limited by the size of the available data sets.

This thesis is structured as follow. The first chapter of this work gives a review of the statistical tests that have been extensively used throughout the years to study the polarization correlations. We also present there a new independent tool that we have developed ourselves. In the second chapter we will use our new method to confirm the presence of correlations between the orientations of the polarizations of quasars when observed at optical wavelengths. The third chapter consists in the search for such alignments of polarization vectors in a large sample of radio-wavelength observations and the presentation of our positive results. We also show that a combination of the polarization alignments from both spectral bands is not feasible due to the poor overlap of the data sets. In chapter four and five, we will then report on a new type of correlations between the polarization orientations of light from quasars and the spatial distribution of the sources, at optical wavelengths and at radio wavelengths. Our conclusion summarize what we have learned from the polarization alignments of quasars during this four years of research and contains an outlook for further investigations.



# Chapter 1

## Dedicated statistical methods

Comparison of polarization orientations from sources that are scarce and non-uniformly distributed on the sky requires dedicated statistical methods. We find important to dedicate a full chapter to introduce the main tools that we will use throughout this work. Hence, we review two statistical tests that have been widely used in the literature to characterize the polarization orientations and further introduce a new method that we have developed. At the end of this chapter, we also discuss an additional method that is widely used in the framework of the studies of the alignments of the morphological axes of galaxies embedded in clusters.

### 1.1 The S and Z tests

In his original paper, Hutsemékers (1998) developed his own test and further used a more sophisticated one originally developed by Andrews and Wasserman and reviewed by Bietenholz (1986). They are referred to as the S and Z tests, respectively. In brief, they are elaborate integrated 2-point correlation functions adapted to axial data. We introduce these two methods in the next sub-sections and provide technical details.

#### 1.1.1 The S test

The S test was originally developed by Hutsemékers (1998) in order to detect and statistically characterize the alignment features of polarization-vector orientations which were first visually detected. Later, Jain, Narain & Sarala (2004) built a variant of this test which actually, and as we shall see, is entirely equivalent of the original one but is much faster on computers. This is convenient when a detailed study is to be considered.

### Hutsemékers version

The S test is based on dispersion measures of the polarization position angles (PA) for groups of  $n_v$  neighbouring sources among the sample. For each object  $i$ , the quantity

$$d_i(\psi) = 90 - \frac{1}{n_v} \sum_{k=1}^{n_v} |90 - |\psi_k - \psi||, \quad (1.1)$$

is computed, where the  $\psi_k$ 's are the polarization PAs of the objects of the group of  $n_v$  neighbours, including the central one, in degree and defined in the range  $0^\circ - 180^\circ$ . This positively defined function accounts for the axial nature of the polarization vectors through the use of the absolute values (Fisher 1993). For the object  $i$ , the mean dispersion of the PAs of the  $n_v$  objects is computed to be the minimum value of  $d_i(\psi)$  and is denoted  $S_i$ . This value will be small for coherently oriented polarization vectors. If  $N$  is the size of the whole sample under consideration, the degree of alignment inside groups among the whole sample is given by a statistics with the free parameter  $n_v$ , defined as

$$S_D = \frac{1}{N} \sum_{i=1}^N S_i. \quad (1.2)$$

$S_D$  measures the concentration of angles for groups of  $n_v$  objects close to each other in space (in 2 or 3 dimensions, as we shall see later). If the polarization vectors are on average locally aligned, the value of  $S_D$  will be smaller than in the case where the PAs are distributed following a uniform distribution on the objects. The significance level (SL) with which one may assign the observed alignment patterns to chance has to be evaluated through simulated data sets because of the mutual dependence between groups. The percentage of simulations with a value of  $S_D$  lower than that of the data gives the SL, i.e. the probability that the dispersion of position angles is due to chance. The generation of simulated data sets is explained in Section 1.1.6.

### Jain et al. version

The variant of the S test introduced by Jain et al. (2004) is very similar to the original one except that, instead of using the dispersion measure in Eq. 1.1, they use

$$d_i^J(\psi) = \frac{1}{n_v} \sum_{k=1}^{n_v} \cos(2(\psi - \psi_k)) \quad (1.3)$$

where the sum is, here also, over the  $n_v$  neighbouring sources of the object  $i$ , including the latter, and where the factor two takes into account the axial nature of the polarization PAs. The position angle  $\bar{\psi}_i$  with respect to which the dispersion of the  $n_v$  PAs of the group around object  $i$  is the least maximizes the function  $d_i^J(\psi)$ . The measure of the dispersion of the PAs is given by this maximal value, as it was given by the minimal value of Eq. 1.1. The larger



the value of  $d_i^J(\bar{\psi}_i)$ , the more concentrated are the PAs. The statistics of a given sample of  $N$  PAs is then introduced as

$$S_D^J = \frac{1}{N} \sum_{i=1}^N d_i^J(\bar{\psi}_i) \quad (1.4)$$

where the sum is over the entire data sample. A large value of  $S_D^J$  implies a strong alignment between the polarization vectors.  $S_D^J = 1$  is the largest value that is possible and would imply that all the polarization vectors of the sample are aligned with each other in groups of  $n_v$  neighbours. It is worth to note that the value  $\bar{\psi}$  that maximizes Eq. 1.3 minimizes in the same time Eq. 1.1, for the same group of sources. This shows that the statistics  $S_D$  and  $S_D^J$  are fully equivalent.

However, the interesting property in the version of Jain et al. (2004) is that the maximization of the  $d_i^J(\psi)$ , as well as the determination of the  $\bar{\psi}_i$ 's can be performed analytically instead of having to minimize Eq. 1.1 via time-consuming trials.

Indeed, searching for the value  $\bar{\psi}_i$  that maximized Eq. 1.3 by the usual procedure, one gets

$$\tan 2\bar{\psi}_i = \frac{\sum_k \sin 2\psi_k}{\sum_k \cos 2\psi_k}. \quad (1.5)$$

Injecting this value in Eq. 1.3 squared, one finally found after trivial calculations that

$$d_i^J(\bar{\psi}_i) = \frac{1}{n_v} \left\{ \left( \sum_{k=1}^{n_v} \cos 2\psi_k \right)^2 + \left( \sum_{k=1}^{n_v} \sin 2\psi_k \right)^2 \right\}^{1/2} \quad (1.6)$$

which is convenient to implement in a computer.

The significance level to which one assigns the observed PA correlations is also obtained through the generation of Monte Carlo simulations.

### 1.1.2 The Z test

The Z test is a non-parametric test originally introduced by Andrews & Wasserman (Bietenholz 1986) to quantify the correlation in groups of objects between the PAs and the position of sources on the sky. The results returned by this test are henceforth not expected to be in full agreement with those from the S test since they are not probing exactly the same kind of correlations.

The basic idea of the Z test is to compute for each object  $j$  the mean direction  $\bar{\psi}_j$  of its  $n_v$  neighbours, excluding this time the central object  $j$ , and to compare this local average to the actual polarization PA of the object  $j$ , namely,  $\psi_j$ . Specifically, the PAs of the  $n_v$  nearest neighbours around each object  $j$  but excluding the latter, are used to compute the mean resultant vector

$$\mathbf{Y}_j = \frac{1}{n_v} \left( \sum_{k=1}^{n_v} \cos 2\psi_k, \sum_{k=1}^{n_v} \sin 2\psi_k \right), \quad (1.7)$$

where the factor two, again, accounts for the axial nature of the polarization. The mean direction  $\bar{\psi}_j$  is given by the normalized mean vector  $\bar{\mathbf{Y}}_j$  through

$$\bar{\mathbf{Y}}_j = (\cos 2\bar{\psi}_j, \sin 2\bar{\psi}_j) . \quad (1.8)$$

The inner product  $D_{i,j} = \mathbf{y}_i \cdot \bar{\mathbf{Y}}_j$ , where  $\mathbf{y}_i = (\cos 2\psi_i, \sin 2\psi_i)$ , gives a measure of the closeness of  $\psi_i$  to  $\bar{\psi}_j$ . If the PAs are correlated to the source positions, then, on average,  $\psi_i$  will be closer to  $\bar{\psi}_{j=i}$  than to  $\bar{\psi}_{j \neq i}$  which, in turn, implies  $D_{i,j}$  to be larger for  $i = j$  than for  $i \neq j$ .

The statistics  $Z_c$  is then introduced as follow (cf. Bietenholz 1986)

$$Z_c = \frac{1}{N} \sum_{i=1}^N Z_i \quad (1.9)$$

where

$$Z_i = \frac{r_i - (N + 1)/2}{\sqrt{N/12}} \quad (1.10)$$

and where  $r_i$  is the rank of  $D_{i,j=i}$ , when the  $D_{i,j=1,n}$ 's are sorted in increasing order (i.e. the position of  $D_{i,j=i}$  in the ordered list of the  $D_{i,j=1,N}$ 's) and  $N$  is the size of the studied sample. If the position angles are independent of the sky positions of the objects, then  $r_i$  is expected to follow a discrete uniform distribution in the interval  $[1, N]$ . The expected value of  $r_i$  is thus  $(N + 1)/2$  with a standard deviation of  $\sqrt{(N^2 - 1)/12}$ . Bietenholz (1986) states that, for  $N > 8$ , the value  $N/\sqrt{12}$  is within 1% of the true standard deviation and used it to build the statistics  $Z_c$ . Given the central limit theorem, the statistics as defined in Eq. 1.9 should be normally distributed. However, for  $i \in [1, N]$ , the  $Z_i$  (from Eq. 1.10) are not independent because of the overlaps between the groups of nearest neighbours.

The statistics  $Z_c$ , which would give the average number of sigma with which the observations differ from pure chance if the  $r_i$  were independent, is therefore approximately normally distributed. This implies that the use of random samples is required in order to evaluate thoroughly the significance level of the dependence of the PAs on the source locations. The SL will therefore be defined as the percentage of simulations that show higher value of  $Z_c$  than that of the observed data.

A modification of the Andrews & Wasserman test was proposed by Hutsemékers (1998). Instead of considering the inner product with  $\bar{\mathbf{Y}}_j$ , he proposed to compute  $D_{i,j} = \mathbf{y}_i \cdot \mathbf{Y}_j$ . This definition is expected to give more weight to the groups of sources having similar PA values. Indeed, aligned polarization vectors imply a large norm of  $\mathbf{Y}_i$  which provides a natural measure of the dispersion of the position angles and leads to a large  $D_{i,j=i}$  in the case of coherent orientations between  $\mathbf{y}_i$  and the  $\mathbf{Y}_i$  of its neighbourhood.

Apart from this variation, the modified statistics is computed in the same way as the original test of Andrews & Wasserman discussed above. In this work, we use this modified version when we refer to the  $Z$  test as it should be more sensitive to local alignments and

thus, more adapted to the search for such features. In Fig. 1.1, we compare for the first time the distribution of the statistics  $Z_c$  of the original test with the one of the modified version. We see that both statistics are approximately normally distributed and that they are actually only slightly different. The individual values of  $Z_c$  from the two versions, though, are found to be different. A deeper understanding of the difference between the two version of the Z test would require the simulation of data set with the introduction of predefined alignment patterns in it. This is beyond the scope of this section and should be further studied elsewhere.

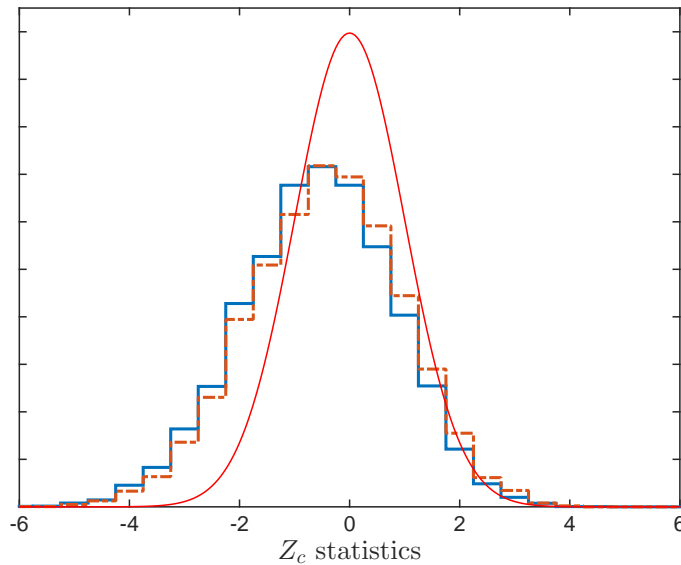


Figure 1.1: The distribution of the  $Z_c$  statistics for the two versions of the Z test. The distribution corresponding to the original test of Andrews & Wasserman (Bietenholz 1986) is plotted in dot-dashed orange and the modified version of Hutsemékers (1998) in blue. The distributions are computed for a sample of 1450 quasars introduced in Chapter 3, the groups of nearest objects are built in 2D (see Section 1.1.5) with  $n_v = 80$  and a number  $N_{\text{sim}}$  of 10 000 Monte Carlo simulations where the PAs are randomly generated according to a uniform distribution. The red over-plotted curve corresponds to a normal distribution that one would obtain if the  $r_i$  were independent such that the central limit theorem would apply.

### 1.1.3 One-free-parameter statistics and its physical interpretation

The S and Z test presented above evaluate the mean level at which the polarization vectors of groups of sources are coherently oriented among a sample and test its significance against randomness. The size of these groups is defined through the only free parameter of the

statistics which is the number of nearest neighbours,  $n_v$ .

To build the groups of nearest-neighbour objects, the relative distances between sources is required. The appropriate distance measure in cosmography is the line-of-sight comoving distance. It is the distance that we would measure locally between two nearby objects (i.e. close in redshift or distance) today if they were locked into the Hubble flow, i.e. if their peculiar velocities were negligible<sup>1</sup>. The comoving distance between two objects remains the same with the epoch. To compute this distance, we follow Peebles (1993). We introduce the function

$$E(z) \equiv \sqrt{\Omega_M (1+z)^3 + \Omega_k (1+z)^2 + \Omega_\Lambda} \quad (1.11)$$

where  $\Omega_M$ ,  $\Omega_k$  and  $\Omega_\Lambda$  are the three dimensionless density parameters of the Universe that reflect its matter density, the curvature of space and the value of the cosmological constant, respectively. These three parameters completely determine the geometry of the Universe and the critical density  $\Omega$ , which is the sum of the three, is normalized to unity (see Hogg 1999 for a brief summary). Assuming a flat and isotropic Universe ( $\Omega_k = 0$ ),  $E(z)$  takes the form

$$E(z) = \sqrt{1 + \Omega_M ((1+z)^3 - 1)}. \quad (1.12)$$

The total line-of-sight comoving distance  $r(z)$  between a source of redshift  $z$  and an observer at  $z = 0$  is given by the integration of  $dz/dE(z)$  along the photon path (see Hogg 1999 and Peebles 1993 for details) as

$$r(z) = \frac{c}{H_0} \int_0^z \frac{dz'}{E(z')} \quad (1.13)$$

where  $c$  and  $H_0$  are respectively the speed of light and the Hubble parameter as measured today.

From Eq. 1.13, the rectangular coordinates of each source are evaluated in a flat Universe through

$$\begin{aligned} x &= r \cos \delta \cos \alpha \\ y &= r \cos \delta \sin \alpha \\ z &= r \sin \delta \end{aligned} \quad (1.14)$$

where  $\delta$  and  $\alpha$  denote the declination and the right ascension of the object in the equatorial coordinate system. The relative distances between sources are then simply computed through the use of their rectangular coordinates.

Note that the Hubble parameter in Eq. 1.13 only acts as a global scaling factor. Therefore, the built neighbouring groups do not depend on its exact value. This is not true, however, for the value of  $\Omega_M$  as it enters in the argument of the integral. The resulting groups of neighbours depend of the adopted cosmological parameters.

Regarding the use of the S and Z tests, it is clear that a three-dimensional analysis of the data set is only feasible for samples for which redshift measurements are available.

---

<sup>1</sup>This will be assumed throughout this work.

Nevertheless, it is worth mentioning that a two dimensional analysis, where we consider the nearest neighbours on the celestial sphere rather than in the 3D space, is not devoid of interest. It is applicable for all samples if we impose  $r = 1$  while we build the groups of nearest neighbours.

In both S and Z tests, the number of nearest neighbours  $n_v$  is a free parameter which has to be explored. Indeed, this parameter is not devoid of physical meaning as it is related to a characteristic scale of the nearest-neighbour groups, in two or three dimensions. This would be strictly true for a sample of sources homogeneously distributed on the whole sky. However, as in general observed samples show deviations from homogeneity and, more importantly, as only part of the entire celestial sphere is commonly covered, the parameter  $n_v$  does not show a straight correspondence with a typical physical size of the groups. A dispersion is naturally expected. Nevertheless, if correlations between polarization orientations occur for a typical scale or if some sub-samples, well delimited in space, present such alignments, it is clear that the SL will be smaller for the corresponding value of  $n_v$  than for others. Therefore, to test the uniformity of the polarization orientations and explore their characteristics, it is necessary to estimate the SL across a wide range of values of  $n_v$ . Note, however, that the lowest value of SL does not provide an accurate estimate of the overall significance of the correlations that might be detected but rather reveals the value of  $n_v$  at which the departure from uniformity is the most significant.

Jain et al. (2004) and Tiwari & Jain (2015) used the S test where they define the groups not with the parameter  $n_v$  but rather with a cut in the comoving distance between sources<sup>2</sup>. Given this modification, they showed that the S test can be used in the same way as before. They also explored the dependence of the values of the significance level on the value of the introduced cut.

This shows explicitly that the number of nearest neighbours has to be explored and that it contains physical information on the alignment patterns.

### 1.1.4 Coordinate dependence of the S and Z test results

The PAs of quantities which are perpendicular to the line of sight to their corresponding sources, i.e. projected in the planes orthogonal to these directions, are dependent on the coordinate system in which the source positions are reported. Let consider a source having  $\alpha$  and  $\delta$  as equatorial coordinates to which corresponds a PA expressed in that coordinate system,  $\psi$ . Then, if we consider an arbitrary system of coordinates for which the equatorial coordinates of its northern pole are  $\alpha_p$  and  $\delta_p$ , the PA  $\psi_N$  corresponding to the source in this new system of coordinates is given by

$$\psi_N = \psi - \arctan \left( \frac{\cos \delta_p \sin(\alpha_p - \alpha)}{\sin \delta_p \cos \delta - \sin \delta \cos \delta_p \cos(\alpha_p - \alpha)} \right). \quad (1.15)$$

---

<sup>2</sup>Note, however, that they fixed the redshift of all the sources of their sample to be  $z = 1$ . Hence, their comoving distance cut must be seen roughly as a cut in angular separation.

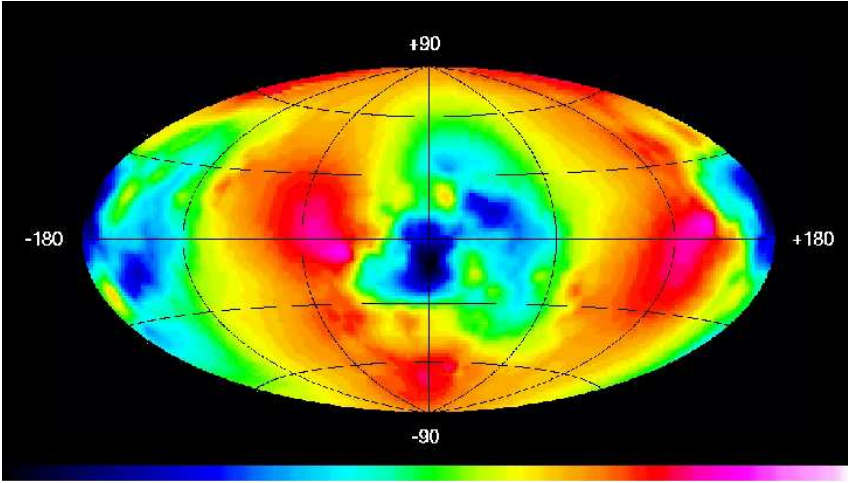


Figure 1.2: Hammer-Aitoff projection of the  $S_D$  statistics averaged over  $n_v = 37$  to 43, as a function of the equatorial coordinates  $\alpha_p$  and  $\delta_p$  of the northern pole of the coordinate system in which the S test is performed. The less significant the statistics for a given pole, the darker the corresponding  $(\alpha_p, \delta_p)$  point on the map. Figure taken from Hutsemékers et al. (2005).

As the changes of PA values depend on the source positions, the distribution of various PAs from angularly separated sources depends on the coordinate system. Accordingly, the significance level of statistical tests is expected to vary. Fig. 1.2 illustrates this dependence for the application of the S test to the sample of 355 quasars compiled in Hutsemékers et al. (2005). The color coded SL was computed for a large set of spherical coordinate systems, spanning the entire sphere, and reported at the northern pole of these. Such coordinate-system dependence of statistical results is obviously unwanted. However, as pointed out by Hutsemékers et al. (2005), this dependence can be used to identify the location on the sky where the alignment are the most significant. Indeed, consider quasars close the equatorial equator with their polarization vectors perfectly aligned. Then, if one chooses a coordinate system with a pole located just in the middle of aligned objects, the polarization angles will range from  $0^\circ$  to  $180^\circ$  and no coherent orientation will be detected by the tests in this new coordinate-system. The regions of minima in Fig. 1.2 indeed point towards the A1 and A3 regions<sup>3</sup>.

### 1.1.5 Parallel transport for coordinate invariance

Jain et al. (2004) developed a workaround to overcome the coordinate dependence of the results returned by the S and Z tests. Instead of computing statistics directly from the PAs that are evaluated with respect to its own meridian, they introduced corrections to the PAs that involve the relative sky positions of the sources. For two sources,  $a$  and  $b$ , separated

<sup>3</sup>Note that this figure is symmetric by construction.  $(\alpha_p, \delta_p)$  is equivalent to  $(\alpha_p + 180^\circ, -\delta_p)$

on the celestial sphere, they proposed to parallel transport the polarization vector of one source onto the other before comparing them<sup>4</sup>. The parallel transport is performed along the sphere geodesic passing through the positions of the two sources. The angle between the polarization vector and the vector tangent to the geodesic is preserved during the parallel transport. The correction to apply to the PAs is simply given by the difference between the angles that the geodesic makes with one of the basis vectors at the locations of the two sources. At location  $P_a$ , the plane tangent to the sphere is defined by the vectors of the local basis  $(\hat{\mathbf{e}}_{\theta_a}, \hat{\mathbf{e}}_{\phi_a})$  in spherical coordinates, where  $\hat{\mathbf{e}}_{\theta_a}$  is pointing toward the southern pole and  $\hat{\mathbf{e}}_{\phi_a}$  towards the East. The angle  $\xi_a$  between the tangent vector of the geodesic  $\hat{\mathbf{t}}_a$  and the basis vector  $\hat{\mathbf{e}}_{\phi_a}$  is given by the two-parameter arctangent function  $\arctan(-\hat{\mathbf{t}}_a \cdot \hat{\mathbf{e}}_{\theta_a}, \hat{\mathbf{t}}_a \cdot \hat{\mathbf{e}}_{\phi_a})$ . This function takes care of the overall addition of  $180^\circ$  if the angle lies in the third or fourth trigonometric quadrants, i.e. if  $(-\hat{\mathbf{t}}_a \cdot \hat{\mathbf{e}}_{\theta_a})$  is negative or  $(-\hat{\mathbf{t}}_a \cdot \hat{\mathbf{e}}_{\theta_a})$  and  $(\hat{\mathbf{t}}_a \cdot \hat{\mathbf{e}}_{\phi_a})$  are both negative. The angle  $\xi_b$  is obtained in the same manner at the location  $P_b$  of the source  $b$ .

Assume that the polarization vector of the source  $a$  forms an angle  $\kappa_a$  with the basis vector  $\hat{\mathbf{e}}_{\phi_a}$  at location  $P_a$ . At location  $P_b$ , the transported vector – from  $P_a$  to  $P_b$  – then forms the angle  $\kappa_a^{(b)} = \kappa_a - \xi_a + \xi_b$  with the basis vector  $\hat{\mathbf{e}}_{\phi_b}$ .

Now, adopting the IAU convention<sup>5</sup>, the corrections to apply to the PAs  $\psi_k$ 's of a sample of sources in order to compare them in a coordinate-invariant fashion at the location of the source  $i$  are given by

$$\begin{aligned}\psi_k^{(i)} &= \psi_k + \Delta_{k \rightarrow i} \\ &= \psi_k + \xi_k - \xi_i\end{aligned}\tag{1.16}$$

The introduction of these simple corrections to the PAs while evaluating Eq. 1.1 (or Eq. 1.3) and Eq. 1.7 leads to coordinate-invariant statistics as was shown by Jain et al. (2004) and Hutsemékers et al. (2005).

In astronomy, when one has to build statistics on the position angles and to circumvent the dependence of the statistics on the coordinate system, one rotates locally the PAs to a coordinate system where the sources are located at the equator (e.g., Planck Collaboration Int. XIX 2015). In principle, it could be demonstrated that the parallel transport corrections mathematically mimic this rotation at least in some cases. The advantage of the parallel transport, thought, is that it can be used for widely dispersed sources on the celestial sphere where it would be impossible to find a coordinate system for which a large patch of the sky could be at the equator.

---

<sup>4</sup>Note that the parallel transport was already introduced in the context of the studies of the alignments of the spins of galaxies (Pen, Lee & Seljak 2000) and is also used to study of the cosmic microwave background polarization (e.g., Keegstra et al. 1997 and Planck Collaboration Int. XIX 2015).

<sup>5</sup>In the International Astronomical Union convention, the position angles are positively measured East-to-North.  $0^\circ$  corresponds to a vector pointing towards the North pole of the coordinate system and  $90^\circ$  to the East.

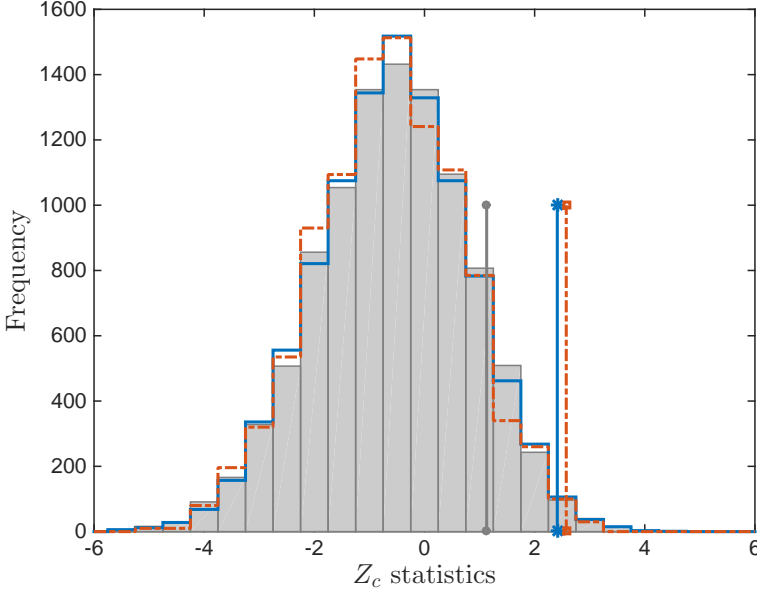


Figure 1.3: The distributions of the  $Z_c$  statistics for the two discussed possibilities for parallel transporting the polarization vectors along with the distribution obtained without correction. The Z test which we equipped with the parallel transport is the modified version of Hutsemékers (1998). The result of the first algorithm (following Eq. 1.17) is shown by the blue line and the second (following Eq. 1.18) with the dot-dashed orange line. The gray histogram is without parallel transport. The vertical lines with corresponding color show the statistics obtained for the real data sets. The same sample as in Fig. 1.1 is used with  $n_v = 80$  and  $N_{\text{sim}} = 10\,000$ .

While there is no ambiguity to equip the S test with the parallel transport correction, the situation is not so clear for the Z test, as it was already pointed out by Jain et al. (2004). Indeed, for the S test, one should just parallel transport the polarization vectors of the  $n_v$  neighbours of source  $i$  at the location of the latter when evaluating Eq. 1.1 (or Eq. 1.3). For the Z test, though, there are at least two different manners to introduce the parallel transport corrections:

- One can first evaluate all the mean resultant vectors  $\mathbf{Y}_j$  by transporting the polarization vectors of the neighbours to the location  $j$  and, afterwards, parallel transport these  $\mathbf{Y}_j$  to the location of the source  $i$  to evaluate the coordinate-invariant  $\tilde{D}_{i,j}$  which is



thus expressed as

$$\begin{aligned}\tilde{D}_{i,j} &= \frac{1}{n_v} \sum_{k=1}^{n_v} \cos \left[ 2 \left( \psi_i - (\psi_k^{(j)} + \Delta_{j \rightarrow i}) \right) \right] \\ &= \frac{1}{n_v} \sum_{k=1}^{n_v} \cos [2 (\psi_i - (\psi_k + \Delta_{k \rightarrow j} + \Delta_{j \rightarrow i}))] \quad (1.17)\end{aligned}$$

- Another algorithm is to parallel transport all the polarization vectors to all the locations of the sources. Then, for each source  $i$ , compute the  $\mathbf{Y}_j$  of all  $j$  and finally compute the coordinate-invariant  $\tilde{D}_{i,j}$  as

$$\begin{aligned}\tilde{D}_{i,j} &= \frac{1}{n_v} \sum_{k=1}^{n_v} \cos \left[ 2 \left( \psi_i - \psi_k^{(i)} \right) \right] \\ &= \frac{1}{n_v} \sum_{k=1}^{n_v} \cos [2 (\psi_i - (\psi_k + \Delta_{k \rightarrow i}))] \quad (1.18)\end{aligned}$$

Despite the fact that the two  $\tilde{D}_{i,j}$  are both coordinate-invariant, they are in general different. This comes from the property of the parallel transport which states that the result depends on the chosen path. Therefore,  $\Delta_{k \rightarrow j} + \Delta_{j \rightarrow i}$  and  $\Delta_{k \rightarrow i}$  are generally different. The only configuration for which they are equal are those where the three locations  $i$ ,  $j$ , and  $k$  belong to the same geodesic of the sphere.

Whereas the parallel transport is a suitable mathematical trick that enables one to build statistics that are coordinate-invariant for circular data tangent to a sphere, there is no real reason to consider the first or the second way presented above, or even imagine more complicated ones. However, the first algorithm (Eq. 1.17) is perhaps more consistent with the fundamental concepts of the Z test (see Bietenholz 1986) and thus, that it seems more appropriate. Nevertheless, this algorithm has not been used in the literature. It is the second algorithm (Eq. 1.18) that has been used in (Jain et al. 2004; Hutsemékers et al. 2005 and Pelgrims & Hutsemékers 2015 (reworked in Chapter 3)). One reason, perhaps, could be the fact that it takes a simpler form (Eq. 1.18) than that of the first. Beside the credit we just gave to the first algorithm, it is worth noticing that for computational purpose the second algorithm should also be disfavoured as it requires  $N$  times more computational steps than the first one<sup>6</sup>.

The only disadvantage that we found to the parallel transport trick is that there is no objective criterion following which one has to choose the way the parallel transport is performed. As a consequence, different statistical results could emerge for the same data set, as shown in Figs. 1.3 and 1.4. However, despite the fact that the distributions obtained through simulations and that the values of the statistics obtained for the observed data set differ from

---

<sup>6</sup>The reason why we will not use the first algorithm (Eq. 1.17) in Chapter 3 is that we realized the above only afterwards.

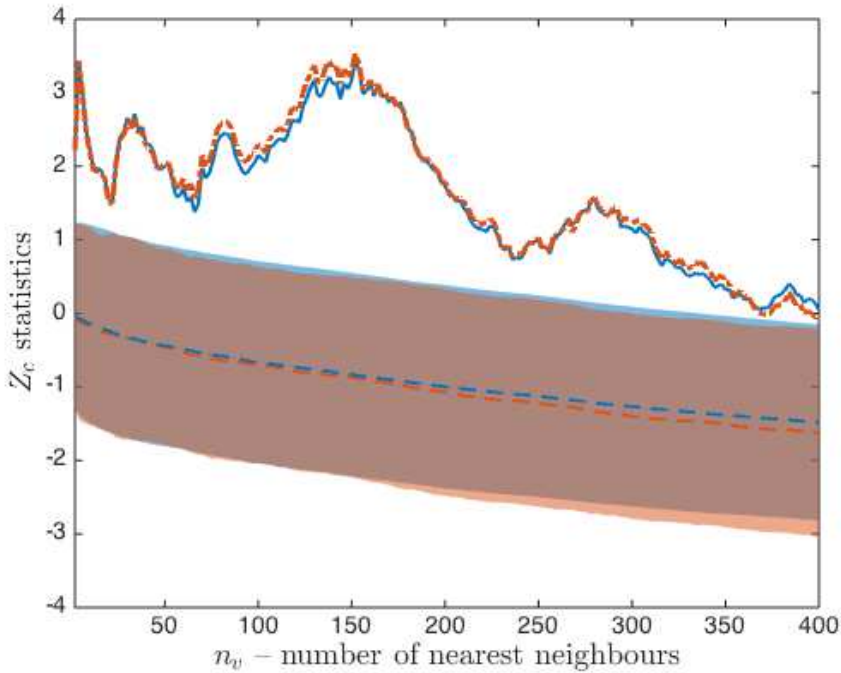


Figure 1.4: The distributions of the  $Z_c$  statistics for the two discussed possibilities for parallel transporting the polarization vectors along with the statistics obtained for the observed data set. The Z test which we equipped with the parallel transport is the modified version of Hutsemékers (1998). The statistics obtained with the first algorithm (following Eq. 1.17) is shown by the blue line and the second (following Eq. 1.18) with the dot-dashed orange line. The  $1\sigma$  confidence intervals (assuming normal distributions) of the prior distributions from the two algorithms are displayed with corresponding color-shaded regions around the means. The same sample as in Fig. 1.1 is used with  $N_{\text{sim}} = 10\,000$  and  $n_v \in [2, 400]$ .

the two method, the returned significance levels agree with each other. Indeed, we found that the values of the significance levels from the two implementations of the parallel transport on the Z test differ by less than a factor of two for the sample that we considered and for the wide range of  $n_v$ -values that we considered. This agreement is enough for our purpose.

### 1.1.6 Generation of simulated data sets

As we stated before, once we use the S or the Z test, simulated data sets are necessary to assess the significance level with which the observations differ from randomness. The need of simulations is due to the mutual dependence of the groups of nearest neighbours which is impossible to estimate analytically. For both tests, and whatever the version of the test, the SL of alignment in a sample is defined as the percentage of generated data sets that give

a statistics as extreme as the one corresponding to the observations. In order to generate a random catalogue, there are two different methods that were already proposed and used in the original paper of Hutsemékers (1998).

For both methods, the sky positions of the sources are kept fixed. Then, the polarization position angles have to be generated. The first method relies on the assumption that at each source location the PAs have to be uniformly distributed. Hence, for this method of data set generation, we generate the  $N$  polarization PAs according to a uniform distribution in the interval  $0^\circ - 180^\circ$  and reproduce this step  $N_{\text{sim}}$  times. The second method uses a re-sampling approach in the sense that the PAs from the observed sample are randomly shuffled among the positions of the sources in order to produce the generated data sets. Namely, the shuffling procedure consists of a bijective mapping of the polarization PAs onto the source positions. Given a coordinate system, let the position vectors of the sources be denoted by  $\hat{e}_r^{(i)}$ , for  $i = 1, \dots, N$ . To each source corresponds a position angle  $\psi$ . The observation data set is thus made of couples  $(\hat{e}_r^{(i)}, \psi_i)$ . The shuffling procedure randomly permutes the PAs in such a way that, for a given randomized sample, the PA at location  $\hat{e}_r^{(i)}$  is given by

$$\psi_i^R = \psi_j \quad (1.19)$$

for a given  $j$  determined by the random permutation of the list  $[1, \dots, N]$ .

Hutsemékers argued that this procedure is more appropriated to the detection of correlated PAs with their corresponding sky locations. He further explained that a possible systematic bias introduced in the data set would be taken into account (Hutsemékers 1998). The final significance level computed via reshuffling method is thus thought to be free of systematic bias. Notice that this is also true if a global physical alignment is contained in the data set. As Jain et al. (2004) showed, a comparison between the SLs obtained with the two methods of data set generations (through shuffling or uniform randomization) can thus help to unveil a global coherence in the polarization PAs.

In the previous section, we discussed the problem of the production of statistical results that are independent of the coordinate system. We have seen that the introduction of the parallel transport helps to solve this issue. One may wonder if the procedures of data set generation that we introduced above lead to distributions that are independent of the system of coordinates.

The distributions obtained with the data sets that are produced through the generation of uniformly distributed polarization PAs in their range of definition are definitely coordinate independent, as long as the number of simulated data sets is large.

The situation is not so clear when the random data sets are generated via the shuffling of the polarization position angles. What is clear, though, is that the distribution of the statistics (Eq. 1.2 and Eq. 1.9) will depend on the system of coordinates if no particular care is taken. To overcome this problem, one has to shuffle the polarization vectors in a coordinate-independent fashion. Again, the introduction of parallel transport helps but a similar ambiguity to the one we discussed in the previous section arises. There is no unique

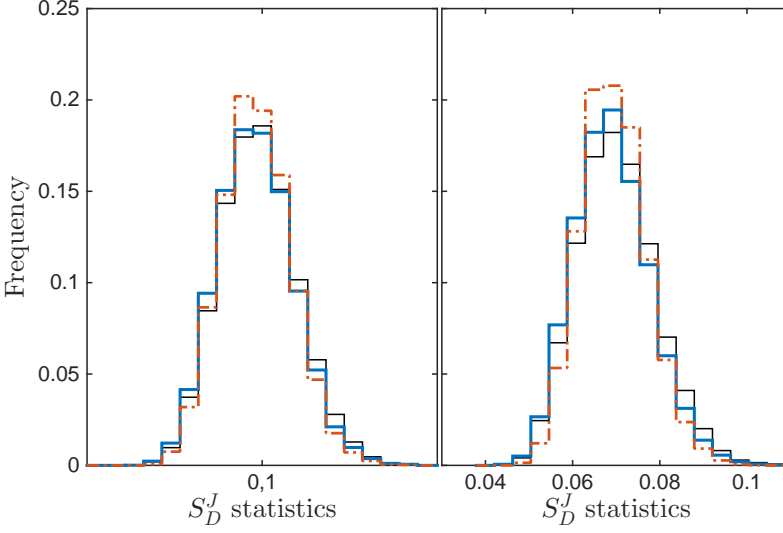


Figure 1.5: The distributions of the  $S_D$  statistics for the two discussed possibilities for generating the randomized data sample while the shuffling procedure is adopted with parallel transport corrections, for two values of  $n_v$ . The distribution from the simplest mapping (Eq. 1.20) is plotted in blue and the more sophisticated one (Eq. 1.21) in dot-dashed orange. The thin-black line corresponds to the distribution generated with PAs drawn from a uniform distribution. The same sample as for Fig. 1.3 is used,  $N_{\text{sim}} = 10\,000$  and  $n_v = 80$  on the left and  $n_v = 160$  on the right.

prescription to equip the shuffling with the parallel transport. We give two such possibilities in the following and compare the significance levels that they lead to.

- The simplest coordinate-independent mapping that one can imagine is that the random position angle at location  $j$  from a generated catalogue  $\psi_j^R$  is given by

$$\begin{aligned}\psi_j^R &= \psi_k^{(j)} \\ &= \psi_k + \Delta_{k \rightarrow j},\end{aligned}\tag{1.20}$$

for a given  $k$  obtained by the random permutation. Readily, compared to the real data sample, the position angle of the source  $k$  has migrated to the source location  $j$  through parallel transport on the sphere. This is done for all the PAs of the sample without repetition, either on the PAs or on the source positions. Starting with the generated sample, the usual procedure to evaluate the statistics has to be applied (with the correction for the parallel transport).

- Another possible algorithm can be imagined as follows. All the polarization vectors of the sample are parallel transported at each source location  $i$ . Then, at each location,

the shuffling of the corrected position angles is done via random permutations. If necessary, then, the shuffled-polarization vectors have to be parallel transported back to their “initial position”.

$$\begin{aligned}\psi_j^{R(i)} &= \psi_k^{(i)} + \Delta_{i \rightarrow j} \\ &= \psi_k + \Delta_{k \rightarrow i} + \Delta_{i \rightarrow j} .\end{aligned}\tag{1.21}$$

In this case, it is important to realize that for the same generated sample, the value of the PA attached to a given source varies according to the source location at which it will be used for the evaluation of the statistics. This justifies the super-script index in the left hand-side of Eq. 1.21. Note that the back parallel transport of the polarization vectors is only necessary for the computation of the Z test if the first algorithm (Eq. 1.17) is chosen.

As we show in Fig. 1.5 the two possible ways of generating randomized data sets via parallel-transport-corrected reshuffling lead to different distributions of the statistics. Indeed, comparison of the histograms reveals that the second algorithm leads to narrower distributions than the first one which, in turn, is narrower than the distribution given by uniform PA generations. The resultant significance level of the observations are thus expected to be different given the adopted method and these differences may become significant as the number of neighbours increases. Indeed, the difference between the values of the standard deviations of the distributions obtained with the different possibilities increases with the number of neighbours  $n_v$ . This is nicely illustrated in Fig. 1.6. The three methods to generate the prior distributions are shown for a very large range of  $n_v$  values. As an illustration, we also plot (in red) the statistics obtained for the real data. A comparison of the red curve with the different distribution shows that one would obtain SL that varies, for the same sample and for the same value of the parameter of the statistics. This would be uncomfortable when thorough analyses are required and, again, there is no physical criterion suggesting one procedure to be preferred. However, we have compared the values of the significance levels returned by the two parallel-transport-corrected shuffling procedures and it turned out that they agree by a factor of two, upto  $n_v = 400$ . The differences between the two methods are thus irrelevant for our purpose.

## 1.2 The polarization cap test

Noting that the large-scale polarization alignments of Hutsemékers et al. (1998; 2001; 2005) had always been characterized by means of the two same statistical methods, we found important to independently confirm them. In this respect, we have developed a new and independent statistical test. It was originally presented in Pelgrims & Cudell (2014) and additional details were given in Pelgrims (2014). The basics of the new method rely on the introduction of a new polarization space, a 2-sphere, and on the treatment of the polarization

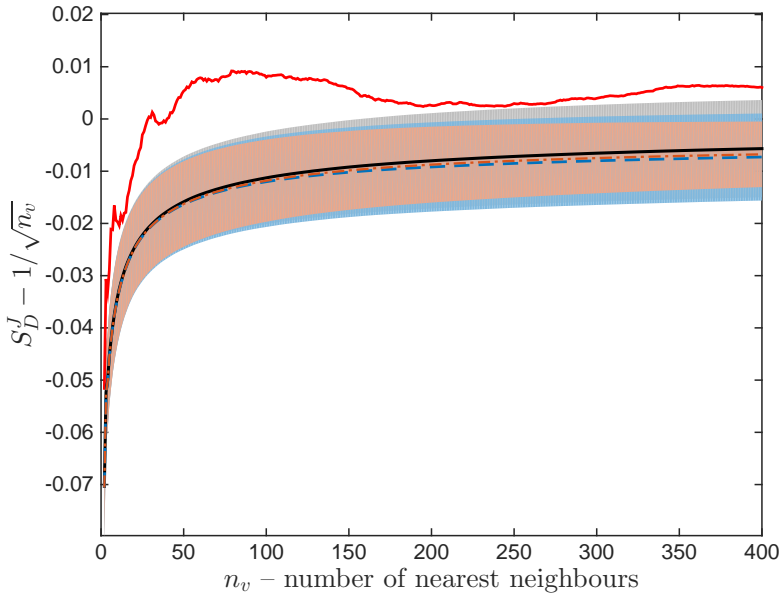


Figure 1.6: The distributions of the  $S_D$  statistics for the two discussed possibilities for generating the randomized data sample while the shuffling procedure is adopted along with uniform randomization, against a large range of value of  $n_v$ . The means of the distributions from the simplest mapping is plotted in dashed blue and the more sophisticated one in dot-dashed orange, the black-thick line is for uniform randomization. The color-shaded regions with corresponding colors mark the  $1\sigma$  confidence intervals of the distributions. We assume normal distributions to compute these intervals. The thick-red line shows the statistics for the real data sample. We use the same sample as for Figs. 1.3 and 1.5 and the distribution are computed for  $N_{\text{sim}} = 10\,000$  and  $n_v$  ranging from 2 to 400 by step of 2.

vectors as points on it. A dedicated study of the density of these polarization points within the cap of the polarization sphere allows for the comparison of the observed distribution of the polarization vector orientations with the distribution that one would expect to observe by chance. The main features of this test are that it is intrinsically coordinate invariant, that the likelihood of the observations against randomness can be analytically derived, that it directly returns the preferred orientation of the polarization vectors and, hence, that it should ease the interpretation of the alignment patterns. We shall refer to this new test as the polarization cap (PC) test. All details of its construction and its working are explained below.

As we will show, the new method allows us to compare the polarization vectors of sources located at different angular coordinates and leads to the characterization of the effect through an unbiased analysis of the data. The basic idea is to consider the physical polarization vectors as 3-dimensional objects rather than 2-dimensional ones embedded in

their polarization plane. These 3-dimensional objects are the directions of the electric field oscillations and they are the physical objects which are measured. As we are dealing with a number of vectors, the definition of a preferred (3-dimensional) direction naturally follows. As we shall see in Chapter 2, the method can be used to study the dependence of the alignment characteristics with redshift, position in the sky or degree of linear polarization by imposing cuts on these variables and repeating the study for the corresponding sub-sample. Naturally, it can also be used to study the distribution of the polarization angles inside groups of sources, similar to the S and Z tests. We use it on this way in Chapter 3.

### 1.2.1 A new coordinate-invariant statistical test for polarization data

When an electromagnetic wave is partially or fully linearly polarized, a polarization vector is introduced. Its norm reflects the degree of linear polarization of the radiation while its direction is that of the oscillating electric field. This vector is embedded into the plane orthogonal to the radiation direction of propagation, the polarization plane. Since the electric field is oscillating, the polarization vector is an axial quantity, rather than a true vector, so that the polarization angle is determined up to  $180^\circ$ .

We consider sources as being points on the unit celestial sphere and we choose a spherical polar coordinate system defined by the orthonormal 3-vectors  $(\hat{e}_r, \hat{e}_\theta, \hat{e}_\phi)$ , with  $\hat{e}_\theta$  pointing to the South pole. Polarization vectors are tangent to this unit sphere. For a given source in the direction  $\hat{e}_r$ , a polarization vector must lie in the plane defined by the two unit vectors  $\hat{e}_\phi$  and  $\hat{e}_\theta$ . We choose the angle  $\kappa$  between the polarization vector  $\mathbf{p}$  and the basis vector  $\hat{e}_\phi$ , defined in the range  $[-90^\circ, 90^\circ[$ , to be the polarization angle. The normalized polarization vector can then be written

$$\hat{\mathbf{p}} = \cos \kappa \hat{e}_\phi - \sin \kappa \hat{e}_\theta . \quad (1.22)$$

Each measurement  $i$  of the data set (Hutsemékers et al. 2005) is equivalent to a position 3-vector  $\hat{\mathbf{e}}_r^{(i)}$  associated with a normalised polarization direction  $\hat{\mathbf{p}}^{(i)}$  and polarization magnitude  $|\mathbf{p}^{(i)}|$ . Contrarily to the various angles,  $\hat{\mathbf{e}}_r^{(i)}$  and  $\hat{\mathbf{p}}^{(i)}$  are physical, i.e. they do not depend on the choice of the coordinate system. As we are interested in polarization alignments, we shall consider mostly the  $\hat{\mathbf{p}}^{(i)}$  in the following.

The problem is then as follows: we have a number of normalised vectors, and we want to decide if they are abnormally aligned. We can draw them from the same origin, and their ends, which we shall call the polarization points, have to lie on a unit 2-sphere, which we shall refer to as the polarization sphere. The problem is that, even when the polarization angles  $\psi$  (or  $\kappa$ )<sup>7</sup> are uniformly distributed, the polarization sphere is not uniformly covered by the points: they have to lie on great circles on the 2-sphere. Indeed, for each source, the polarization vectors are constrained to be in the plane defined by the basis vectors  $(\hat{e}_\phi^{(i)}, \hat{e}_\theta^{(i)})$ .

---

<sup>7</sup>If  $\psi$  are the polarization position angles given in the IAU convention, then we have  $\kappa = 90^\circ - \psi$ . We developed our formalism in terms of  $\kappa$  for simplicity.

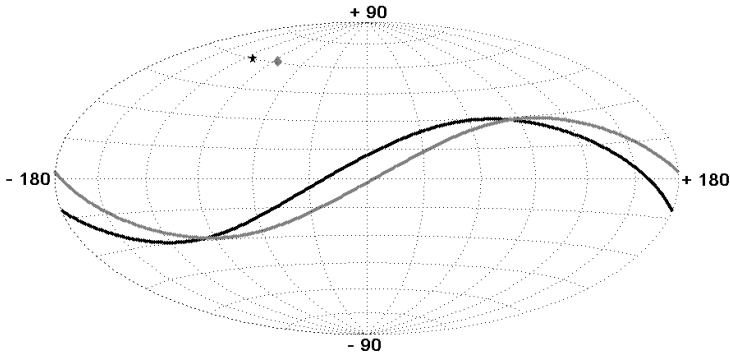


Figure 1.7: Superposition of the Hammer-Aitoff projections of the celestial sphere and the polarization sphere (in Galactic coordinates). Two quasars (B1115+080 (in black) and B1157+014 (in grey)) are displayed on the celestial sphere with the corresponding geometric loci of their polarization point on the polarization sphere. The source position and the corresponding geometric locus of the polarization point are printed in same brightness.

The intersection of the plane with the polarization sphere is a great circle, which is the geometric locus where the polarization vector attached to the source  $i$  may intersect the sphere, as shown in Fig. 1.7. See Fig. 1.8 for an illustration of the notations and of the concept of the above. Note that the Fig. 1.7 is symmetric as polarization vectors are defined up to a sign. In the following, we choose to show the full sphere, although a half-sphere could be used to represent the polarization space.

As a result, simple spherical data analysis such as those presented in Fisher et al. (1993) are not applicable in the case of transverse quantities because of the constrained geometrical locus of the points. One can nevertheless evaluate the density of points at each location on the unit 2-sphere by adopting Kamb-like methods (e.g., Vollmer 1995). Namely, to compare the observations with what one would expect if the polarization points were drawn from a random distribution of polarization angles, we need to select a region on the polarization sphere, count the number of polarization points within this region, and compare this number with the prediction. One could do this by Monte-Carlo techniques but the probabilities turn out to be rather low so that a detailed study would prove difficult.

However, we found that a particular choice of shape for the region on the sphere considerably simplifies the evaluation of the probabilities. We consider cones in which the polarization vectors fall, or equivalently spherical caps of fixed aperture angle. The probability distribution of a given number of points in a given spherical cap can be computed analytically when densities are evaluated through a standard step function, as explained be-



low. A scan of the whole polarization half-sphere with such cones leads to a map of expected densities which constitutes the statistical background. At any location on the half-sphere, the hypothesis of uniformity can then be tested by calculating the probability of the observed number of polarization points. An alignment of polarization vectors from different sources will be detected when an over-density between data points and the background is significant.

### 1.2.2 Construction of the probability distribution

As mentioned above, the locus of a polarization point is a half-circle in the plane normal to the source position vector. The probability that a polarization point lies inside a spherical cap is then given by the length of the arc of circle intercepted by the cap, divided by the whole length of the half-circle ( $\pi$ ). Let  $\eta$  being the half-aperture angle of the spherical cap, and  $\hat{s}$  the unit vector pointing to its centre. If  $\hat{p}^{(i)}$  is a normalised polarization vector attached to the source  $i$ , with position vector  $\hat{e}_r^{(i)}$ , the corresponding polarization point lies inside the spherical cap centred at  $\hat{s}$  if and only if

$$|\hat{p}^{(i)} \cdot \hat{s}| \geq \cos \eta \quad (1.23)$$

is verified. Adopting the decomposition of  $\hat{p}^{(i)}$  along two vectors in the polarization plane

$$\hat{p}^{(i)} = A \left( \hat{s} - \left( \hat{s} \cdot \hat{e}_r^{(i)} \right) \hat{e}_r^{(i)} \right) + B \hat{t}^{(i)} \quad (1.24)$$

where  $\hat{t}^{(i)} = \left( \hat{e}_r^{(i)} \times \hat{s} \right) / |\hat{e}_r^{(i)} \times \hat{s}|$ , a straightforward calculation involving the normalisation of  $\hat{p}^{(i)}$  and the condition for being inside the spherical cap leads to the arc length  $L^{(i)}$  of the geometric locus lying inside the considered area. The result takes a simple form in terms of  $\tau^{(i)} \in [0^\circ, 90^\circ]$ , the acute angle between  $\hat{e}_r^{(i)}$  and  $\hat{s}$ : the condition in Eq. 1.23 becomes  $\sin \tau^{(i)} \geq \cos \eta$  and, by integration of the line element, the arc length within the cap is found to be

$$L^{(i)} = \begin{cases} 2 \arccos \left( \frac{\cos \eta}{\sin \tau^{(i)}} \right) & \text{if } \sin \tau^{(i)} \geq \cos \eta \\ 0 & \text{otherwise .} \end{cases} \quad (1.25)$$

Therefore, the probability  $\ell^{(i)}$  that the  $i$ -th source of the sample leads to a polarization point inside a given spherical cap is

$$\ell^{(i)} = \frac{L^{(i)}}{\pi}. \quad (1.26)$$

Hence, this probability only depends on the chosen aperture angle of the spherical cap and on the angle between the source position and the cap centre. This probability is thus completely independent of the system of coordinates.

For each cap, the set of probabilities  $\ell^{(i)}$ , corresponding to a set of polarized sources, leads to the construction of the probability distribution  $P_n$  of observing exactly  $n$  points of

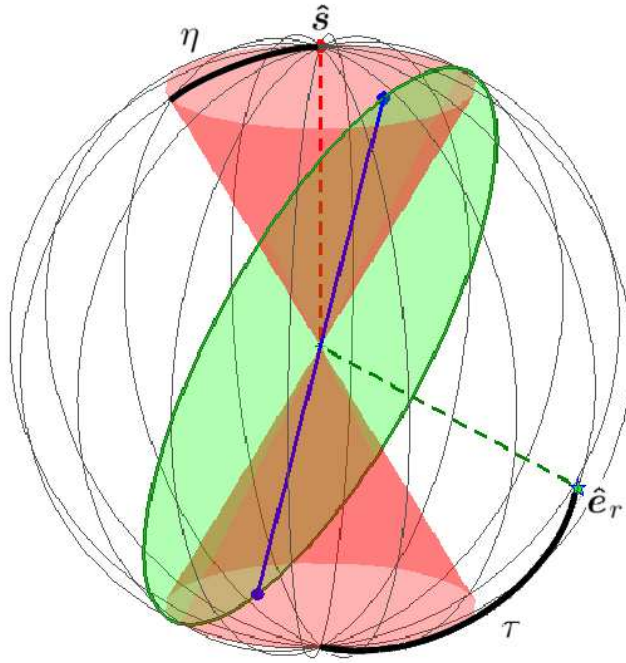


Figure 1.8: Illustration of the building of the PC test. The considered source is represented by the star with the pointing vector in dashed green. The green disk is the polarization plane drawn at the origin of the coordinate system, the dark green circle is the geometrical locus of all possible polarization points which correspond to the source. The blue axis corresponds to the axial-polarization vector attached to the source. The blue points at its ends, at the intersection with the unit sphere, are the observed polarization points. The red point (here at the pole of the sphere) is the centre of a spherical cap of half-aperture angle  $\eta$  defined by the intersection of the cone (in red) and the unit sphere. Under the hypothesis that the polarization position angle are drawn from a uniform distribution, the probability that the polarization points fall inside the spherical cap depends only on the acute angle  $\tau$  (Eq. 1.25) between the vectors pointing towards the source ( $\hat{e}_r$ ) and towards the centre of the cap ( $\hat{s}$ ).

polarization inside the spherical cap. If  $N$  is the sample size, we have:

$$P_0 = \prod_{i=1}^N (1 - \ell^{(i)}) \quad (1.27)$$

$$P_1 = \sum_{j=1}^N \ell^{(j)} \prod_{i \neq j} (1 - \ell^{(i)}) \quad (1.28)$$

$$P_2 = \frac{1}{2} \sum_{k=1}^N \ell^{(k)} \sum_{j \neq k} \ell^{(j)} \prod_{i \neq j \neq k} (1 - \ell^{(i)}) \quad (1.29)$$

$\vdots$

$$\begin{aligned} P_N &= \frac{1}{N!} \sum_{l=1}^N \ell^{(l)} \dots \sum_{j \neq \text{prev. indices}} \ell^{(j)} \prod_{i \in \{\emptyset\}} (1 - \ell^{(i)}) \\ &= \prod_{l=1}^N \ell^{(l)} \quad . \end{aligned} \quad (1.30)$$

Note that following the previous definitions, it is possible to write, for each  $n \geq 1$ ,

$$P_n = \frac{1}{n} \sum_{j=1}^N \ell^{(j)} P_{n-1 \setminus j} \quad (1.31)$$

where  $P_{n-1 \setminus j}$  is the probability to observe  $n-1$  points of polarization (and only  $n-1$ ) after the  $j$ -th element is removed from the original sample, making the new sample size  $N-1$ .

### 1.2.3 A fast algorithm for generating the $P_n$

Starting with the entire sample of size  $N$ , let us consider the probability  $P_0$  to observe no polarization point within the cap. We remove the  $k$ -th element from this sample. Then, from Eq. 1.27, the probability to observe no polarization point within this reduced sample, denoted by  $P_{0 \setminus k}$ , is related to  $P_0$  through  $P_0 = \ell^{(k)} P_{0 \setminus k}$ , where we introduced the following notation for the probability that the source  $k$  does not lead to a polarization point in the concerned area :  $\ell^{(k)} \equiv (1 - \ell^{(k)})$ .

First consider the probability  $P_1$  to observe one and only one polarization point:

$$\begin{aligned}
 P_1 &= \sum_{j=1}^N \ell^{(j)} \prod_{i \neq j} \ell^{(i)} \\
 &= \sum_{j=1}^N \ell^{(j)} P_{0 \setminus j} \\
 &= \sum_{j \neq k} \frac{\ell^{(j)}}{\ell^{(j)}} P_0 + \ell^{(k)} P_{0 \setminus k} \\
 &= \ell^{(k)} \left( \sum_{j \neq k} \frac{\ell^{(j)}}{\ell^{(j)}} P_{0 \setminus k} \right) + \ell^{(k)} P_{0 \setminus k} \\
 &= \ell^{(k)} P_{1 \setminus k} + \ell^{(k)} P_{0 \setminus k} \quad .
 \end{aligned} \tag{1.32}$$

A similar calculation leads to  $P_2 = \ell^{(k)} P_{2 \setminus k} + \ell^{(k)} P_{1 \setminus k}$ . One can prove by induction that the following relation holds for every  $m \in \mathbb{N}$ :

$$P_m = \ell^{(k)} P_{m \setminus k} + \ell^{(k)} P_{m-1 \setminus k} \tag{1.33}$$

Indeed, assuming the relation is true for  $m \leq n-1$ , it is easy to show that it is then true for  $m = n$ :

$$\begin{aligned}
 P_n &= \frac{1}{n} \sum_{l=1}^N \ell^{(l)} P_{n-1 \setminus l} \\
 &= \frac{1}{n} \sum_{l \neq k} \ell^{(l)} P_{n-1 \setminus l} + \frac{1}{n} \ell^{(k)} P_{n-1 \setminus k} \\
 &= \ell^{(k)} \left( \frac{1}{n} \sum_{l \neq k} \ell^{(l)} P_{n-1 \setminus l \setminus k} \right) + \ell^{(k)} \left( \frac{1}{n} \sum_{l \neq k} \ell^{(l)} P_{n-2 \setminus l \setminus k} \right) + \frac{1}{n} \ell^{(k)} P_{n-1 \setminus k} \\
 &= \ell^{(k)} P_{n \setminus k} + \ell^{(k)} \left( \frac{n-1}{n} \left[ \frac{1}{n-1} \sum_{l \neq k} \ell^{(l)} P_{n-2 \setminus l \setminus k} \right] \right) + \ell^{(k)} \frac{1}{n} P_{n-1 \setminus k} \\
 &= \ell^{(k)} P_{n \setminus k} + \ell^{(k)} P_{n-1 \setminus k} \quad .
 \end{aligned} \tag{1.34}$$

Therefore, Eq. 1.33 holds<sup>8</sup> for every  $m \in \mathbb{N}$ . Assuming that, for a sample of size  $N$  and for a given spherical cap, we have all elementary probabilities  $\ell^{(i)}$ , we use the following algorithm for numerically computing the probability distribution:

- i. We introduce a column vector  $V$  of size  $N+1$ , initialized to zero, except for  $V_0$  which is set to 1. The  $V_n$  are the  $P_n$  for an empty data set (with  $n = 1, \dots, N$ ).

---

<sup>8</sup>Afterwards, we realized that Eq. 1.33 was first introduced by Howard (1972) and its numerical behaviour was extensively discussed by Chen & Liu (1997) about computational techniques for the Poisson-binomial probabilities. The algorithm presented here is equivalent to that given in Chen & Liu (1997).

- ii. We add one data point at a time, and update  $V$  according to Eq. 1.33.
- iii. After  $N$  iterations, the  $V_n$  give the  $P_n$  distribution for the studied sample.

We test our implementation of the algorithm by comparing its results to those obtained via a Monte-Carlo treatment, for the A1 region of Hutsemékers et al. (2005). For the generation of the Monte-Carlo samples, we proceed as follow. We keep the quasar positions fixed and we generate random polarization PAs according to a uniform distribution. For various spherical caps, we count the number of polarization points falling effectively in these caps and build the expected distributions through the simulated data sets. We then compare these distributions to the  $P_n$  distributions from our algorithm and Eqs. 1.25 and 1.26. As illustrated in Fig. 1.9 for an arbitrary spherical cap, we obtain very good agreement between theory and simulation. We checked that the same conclusions are obtained for arbitrary sub-samples of quasar polarization measurements presented in Hutsemékers et al. (2005) and for arbitrary spherical cap.

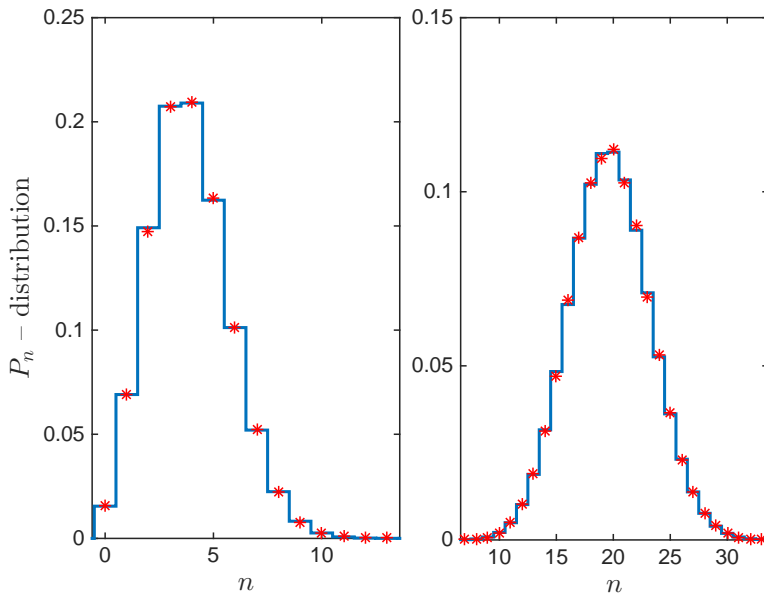


Figure 1.9: Comparison of the  $P_n$  distribution built from our algorithm presented in Section 1.2.3 (in blue) and the normalized histogram (red asterisk) obtained by running 100 000 random simulations where the positions of the sources are kept fixed and the PAs uniformly distributed. For this simulation, we take the A1 region (see Table 1.1), choose arbitrarily a spherical cap and set  $\eta = 12^\circ$  for the left panel and  $\eta = 35^\circ$  for the right.

### 1.2.4 A first example

To illustrate the use of the above, we show in Fig. 1.10 a map of the expected background for region A1 of Hutsemékers et al. (2005), as defined in Table 1.1. At each point  $a$  of the

region	declination	right ascension	redshift	number of quasars
A1	$\delta \leq 50^\circ$	$168^\circ \leq \alpha \leq 217^\circ$	$1.0 \leq z \leq 2.3$	56
A2	$\delta \leq 50^\circ$	$150^\circ \leq \alpha \leq 250^\circ$	$0.0 \leq z < 0.5$	53
A3		$320^\circ \leq \alpha \leq 360^\circ$	$0.7 \leq z \leq 1.5$	29

Table 1.1: The three regions of alignment of Hutsemékers et al. (2005) in equatorial coordinates B1950.

polarization sphere we associate a probability distribution  $P_n^a$  through the use of spherical caps. The mean values  $\bar{N}^a = \sum_n n P_n^a$  determine the expected number of polarization points. From those numbers, we build iso-density regions on the polarization sphere in order to visualize the structure that the statistical background takes. We arbitrarily choose here caps of half aperture  $\eta = 17^\circ$ . The dependence of the results on  $\eta$  will be discussed in Section 1.2.5.

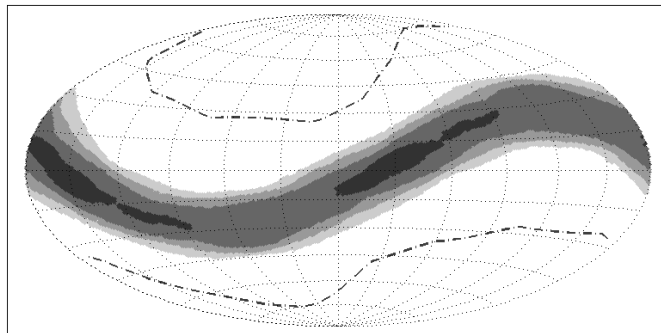


Figure 1.10: Hammer-Aitoff projection (Galactic coordinates) of the polarization sphere associated to the A1 region. Expected density regions are displayed following the legend: white:  $\bar{N}^a < 4$ ; light grey:  $4 \leq \bar{N}^a < 5$ ; grey:  $5 \leq \bar{N}^a < 6$ ; dark grey:  $6 \leq \bar{N}^a < 7$ ; black:  $\bar{N}^a \geq 7$ . White regions towards poles which are delimited by dashed curves are regions where polarization points cannot fall at all. For this map, we arbitrarily fix  $\eta = 17^\circ$ .

Due to the non uniformity of the source locations, there are regions of maxima (and

minima) in the expected densities of polarization points as well as regions where polarization points are forbidden. For this sample, a close look at Fig. 1.10 shows that a quadrupole is naturally expected in the density structure on the polarization sphere. This shows that the use of the  $P_n$  distributions is mandatory, as the expected density is not flat.

### 1.2.5 Further refinements of the method

#### Optimal set of centres for the spherical caps

The method presented so far has two problems:

- Several spherical caps can contain the same polarization points, so that several probabilities are assigned to the same set of data points.
- Among the caps containing the same data points, the most significant ones will be those for which several of the  $\ell^{(i)}$  will be small, i.e. for which the loci of several polarization points are almost tangent to the caps. This enhanced significance is an artefact of our method which is due border effects.

In order to minimize these problems, we do not allow all caps to be considered, but rather focus on those that correspond to cones with an axis along the vectorial sum of the normalised polarization vectors inside them. Hence the effective polarization vector corresponding to the centre of the cap is

$$\begin{aligned} \mathbf{s}_{centre} &= \sum_{i \in \text{cap}} \hat{\mathbf{p}}^{(i)} , \\ \hat{\mathbf{s}}_{centre} &= \frac{\mathbf{s}_{centre}}{|\mathbf{s}_{centre}|} . \end{aligned} \quad (1.35)$$

These centres are first determined by iteration before applying the algorithm explained above.

#### Local p-value of the data

The study of alignments is performed separately for each cap  $a$  on the polarization sphere, for which we derive probability distributions  $P_n^a$ . In each cap, we count the number  $o_a$  of observed polarization points, and  $P_{o_a}^a$  gives us the probability that the presence of  $o_a$  polarization points in cap  $a$  is due to a background fluctuation. The probability that a generation from a uniform background has a density greater than the observed one is given by the p-value  $p^a = \sum_{n \geq o_a} P_n^a$ . The latter quantity gives us the significance level of a specific polarization point concentration in one given direction. As already mentioned, Eq. 1.26 shows that the probabilities are coordinate invariant. It in fact provides a generalisation of the binomial test used in Hutseméekers et al. (1998; 2001; 2005). In other words, the  $p^a$ 's give the cumulative Poisson-Binomial probabilities that, given the set of polarized sources

and under the assumption that the polarization angles are uniformly distributed, there are  $o_a$  or more polarization points in the cap of half-aperture  $\eta$  and centred on  $a$ .

For each sample, we can consider the cap  $a_{\min}$  that gives the most significant p-value  $p_{\min} = \min_a(p^a)$  which we call the significance level. This defines a direction in polarization space, and a plane in position space.

### Dependence on the spherical cap aperture

The only free quantity in this method is the aperture half-angle of the spherical caps. More

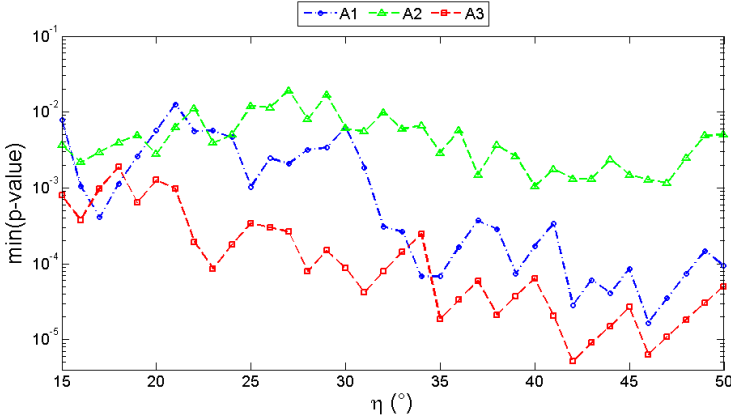


Figure 1.11: Dependence of the significance level with  $\eta$ , the half-aperture angle of spherical caps (in degree). The regions are defined as in Table 1.1.

than a simple bin width as in histogram-based statistics, the value of  $\eta$  is also somewhat similar to that of the number of nearest neighbours used in (Hutsemékers 1998; Jain et al. 2004 and Hutsemékers et al. 2005), and it has a physical meaning.

First of all, each polarization cap corresponds to a band in the sky, which has an angular width of  $2\eta$ . Hence,  $\eta$  selects part of the celestial sphere. Secondly, as the sources are angularly separated and as quasar polarization vectors are always perpendicular to the line of sight, their projections to the centre of the polarization sphere will always be spread.  $\eta$  takes this spread into account. Finally,  $\eta$  is linked to the strength of the effect (more on this in Section 2.2.3). A very strong alignment will gather the polarization points in a small cap, due only to the spread of the sources. A weaker one will necessitate larger caps, as the effect will be added to a random one that produces a large spread on the polarization sphere. We thus see that  $\eta$  is determined by physical parameters: the spread of the sources and the strength of the effect. It thus seems reasonable to determine its optimal value, which we shall do in the next subsections.

For a given sample of sources we perform the study for a wide range of half-aperture angle. For each of them we determine the optimum cap centres, and calculate  $p_{\min}$  as a



function of  $\eta$ . Fig. 1.11 shows  $p_{\min}$  as a function of  $\eta$  for the sub-samples A1, A2 and A3 defined in Table 1.1 and for  $\eta$  taking all integer values between  $15^\circ$  and  $50^\circ$ . Fig. 1.11 shows that the different samples present significant over-densities of polarization points. We see that  $p_{\min}$  is smaller for  $\eta$  between  $30^\circ$  and  $50^\circ$ , depending on the sample.

### Global significance level of the effect

So far, we have considered the probability that an over-density in a given cap be due to a background fluctuation. A more relevant probability maybe that of the occurrence of such an over-density anywhere on the polarization sphere. To calculate this, we have resorted to a Monte-Carlo treatment, generating for each data sample  $N_{\text{sim}}$  simulated data sets, in which we consider only the quasars of that data set, keep their positions fixed on the sky, and randomly vary their polarization angles according to a flat distribution. For a given data sample, we introduce a global significance level  $p^\sigma$  defined as the percentage of random sets which produce p-values smaller or equal to  $p_{\min}$  somewhere on the polarization sphere.

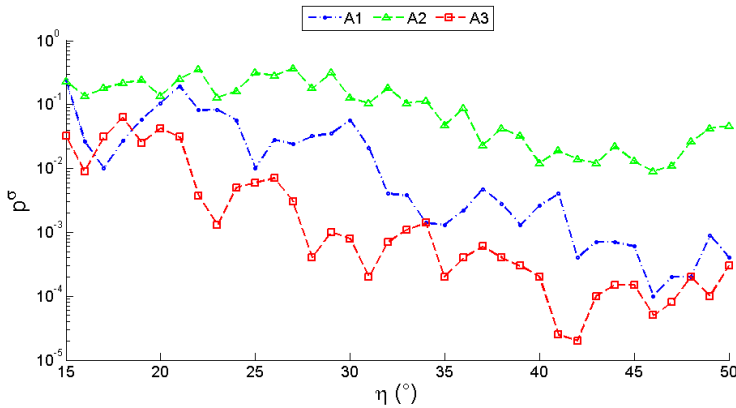


Figure 1.12: Behaviour of the global significance level with the half-aperture angle for the A1, A2 and A3 regions of Table 1.1.

### Optimal angle for the spherical caps

Fig. 1.12 shows the behaviour of the global significance level  $p^\sigma$  with the aperture angle of the spherical caps for the sub-samples A1, A2 and A3. Comparing Figs. 1.11 and 1.12, we note that  $p^\sigma$  and  $p_{\min}$  follow the same trend. Clearly, the relation between them must involve the number of possible caps  $N_c$  and  $p^\sigma$  would be equal to  $N_c p_{\min}$  if the caps did not overlap and if all simulated data sets had the same number of caps. Hence we expect  $N_c$  to be of the order of the area of the half-sphere divided by the area of a cap,  $p^\sigma \approx p_{\min} / (1 - \cos \eta)$ . We found empirically that this relation underestimates  $p^\sigma$  by a factor smaller than 4, for all the (sub-)samples we analysed.

Table 1.2 shows the significance levels  $p_{\min}$  of over-densities obtained for the different samples of quasars, compared with the binomial probability  $P_{\text{bin}}$  reported by Hutsemékers et al. (2005). Note that a spherical cap is in general sensitive only to sources along a band of the celestial sphere so that only part of the entire data sample can contribute to it. We thus compare the number of polarization points in the cap  $o_a$  to the maximum number of points possible in that cap,  $o_a^{\max}$ .

We see from Table 1.2 that the best half-aperture angle depends on the region, and that it is large: 42 or 46 degrees. We also see that the regions A1 and A3 defined by Hutsemékers et al. (2005) are the most significant with our algorithm. However, we need to know whether the difference between  $P_{\text{bin}}$  and  $p_{\min}$  is important. We shall then study the errors on the significance level and on  $\eta$  and see that the discrepancies are reasonable. To do so, we perform a jackknife analysis, removing in turn each quasar from a given sample, and performing the analysis again. The results are show in Fig. 1.13. We see that the errors on  $\eta$  are large, and that  $p_{\min}$  can go up or down by a factor of the order of 3. Hence it seems that our method really agrees with the estimates of (Hutsemékers et al. 2005). One also clearly sees that region A2 is less significant than A1 and A3.

Region	$P_{\text{bin}}$	$p_{\min}$	$\eta$ ( $^\circ$ )	$o_a/o_a^{\max}$	$p^\sigma$
A1	$3.3 \cdot 10^{-6}$	$1.7 \cdot 10^{-5}$	46	43/56	$1.0 \cdot 10^{-4}$
A2	—	$1.7 \cdot 10^{-3}$	46	32/47	$0.9 \cdot 10^{-2}$
A3	$2.6 \cdot 10^{-5}$	$5.1 \cdot 10^{-6}$	42	25/29	$2.7 \cdot 10^{-5}$

Table 1.2: Significance levels for various data samples.  $o_a$  is the number of polarization points inside the spherical cap where the minimum significance level (minimum p-value)  $p_{\min}$  is observed,  $o_a^{\max}$  is the maximum number of polarization points that might fall inside this cap,  $\eta$  is the half-aperture angle of the cap,  $P_{\text{bin}}$  is the binomial probability obtained by Hutsemékers et al. (2005) (Table 1) and  $p^\sigma$  is the global significance level of the region obtained through the method explained above.

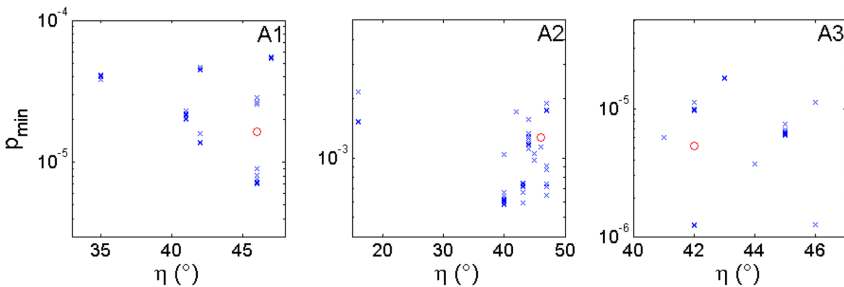


Figure 1.13: Result of the jackknife methods for regions A1, A2 and A3. The red circles correspond to the results of Table 1.2.

### Mean position angle for local groups

During our analysis in Section 3.2.1, we consider groups of neighbouring sources and report the mean position angle  $\bar{\psi}_{\text{PC}}$  of their corresponding polarization PA distributions. The latter is computed with respect to the spherical basis vectors  $(\mathbf{e}_\phi, -\mathbf{e}_\theta)_{\text{CM}}$  at the location given by the normalized vectorial sum of the 2-dimensional positions of the sources. The mean position angle corresponds to the projection of the normalized sum of the polarization vectors of the sources onto the plane tangent to the sphere at this mean position. This quantity has a meaning only when the maximum angular separation between studied sources is not large and when the position angle distribution is not uniform.

### 1.2.6 The PC test: conclusion

We have presented a new one-parameter coordinate-invariant method designed to detect and characterize polarization alignments from sparse data. The basics of this method are independent from the previous tests. The new method can thus be used to independently study the orientation distribution in polarization data catalogues.

This method has the considerable advantage to return significance levels that are semi-analytically computed. Indeed, our algorithm leads to rapid evaluation of the probabilities that, by chance, the polarization vectors point towards given directions, without the need of random catalogue generations. Hence, the use of this method allows us to determine unambiguously the direction of polarization alignments in space and to test for their significance against randomness. The remaining drawbacks, however, are that the determination of the global significance levels relies on very time-consuming Monte Carlo simulations and that the only parameter of the method might induce edge effects in the same way as the bin width value does in histogram-based studies. The edge effects are minimized but not removed by the arbitrary (and time consuming) selection of spherical caps for which the density studies are performed (see Section 1.2.5). These unwanted effects might eventually be dimmed by adopting another function than the step function for the evaluation of the densities. However, we did not yet find any function that still leads to an analytical determination of elementary probabilities (Eq. 1.26), which is one of the pillar of the method.

All in all, we provide a new statistical test that allows for the study of the distribution of the polarization PAs from astronomical sources. Compared to the S and Z tests, our method is intrinsically coordinate-invariant via physically motivated arguments. However, and given its current version, this new test still contains the weak points discussed above. It is worth mentioning that our method can be used to compare directly the polarization vectors from sources that are oppositely located on the celestial sphere. In the framework of cosmological scenarios this constitutes a considerable advantage compared to the S and Z tests. Finally, this new statistical test cannot replace the other methods presented earlier in this chapter. It is complementary to them. This is especially true for the Z test which, in addition to testing for local alignments of the polarization vectors, also studies the correlation of the alignment

patterns with their specific locations on the sky.

The working of the method is summarized in Fig. 1.14. For this illustration, we use a sub-region of the sample of the 355 quasars with optical polarization measurement compiled in Hutsemékers et al. (2005). This sub-sample, named the S2+ region, is identified in Section 2.2.1 where we performed an unbiased analysis in order to extract the most aligned regions from the optical sample. For this region of 18 quasars, the local and global probabilities are found to be  $p_{\min} = 1.9 \times 10^{-6}$  and  $p^{\sigma} = 1.0 \times 10^{-5}$  when the half-aperture angle of the spherical cap being used is arbitrarily set to  $\eta = 45^{\circ}$ .

### 1.3 The Hawley–Peebles Fourier method

In Chapter 3, we will make use of an additional statistical test commonly used to study the alignments of galaxy morphologies. This test, called the Hawley–Peebles test after Hawley & Peebles (1975), is based on fitting the observed distribution of PAs by a model of the form

$$n(\psi_i) = \bar{n} (1 + \Delta_1 \cos 2\psi_i + \Delta_2 \sin 2\psi_i) \quad (1.36)$$

where  $\bar{n}$  is the mean of the number of objects per bin and  $n(\psi_i)$  is the observed number of objects in the bin centred in  $\psi_i$ . The number of bins, and thus their width, is a free parameter.  $\Delta_1$  and  $\Delta_2$  are the coefficients of the wave model which describe the degree of deviation of the distribution from being uniform. If the PAs are not uniformly distributed, the mean position angle is given by  $\bar{\psi} = (1/2) \arctan (\Delta_2/\Delta_1)$ . A good measure of departure from uniformity is the total amplitude  $\Delta^2 = \Delta_1^2 + \Delta_2^2$ . As easily understood, the larger the value of  $\Delta$ , the less uniform the distribution. The probability that the total amplitude exceeds by chance a given value of  $\Delta$  is computed to be approximately

$$P_{\text{HP}} = \exp (-n\Delta^2/4) \quad (1.37)$$

where  $N$  is the number of objects in the sample. However, as far as small samples are considered, random simulations are required as the distribution of  $\Delta$  differs from a normal Gaussian and as this approximate relation fails far out in the tails (see Godłowski 2012 for a detailed discussion). For the simulated samples, polarization PAs are uniformly generated and distributed among the sources. The probability  $P_{\text{HP}}$  is then simply given by the percentage of random realizations having a  $\Delta$  value larger than that of the data.

In our Chapter 3, we tested all reported probabilities using random simulations and we only found marginal differences compared to those given by the approximate relation (Eq. 1.37). These are actually smaller than the variations caused by the choice of the number of bin. We decided to report only the probabilities computed through the Gaussian approximation. It is worth mentioning that this statistical test also depends on the coordinate system in which PAs are defined. However, as we will use this test to study the uniformity

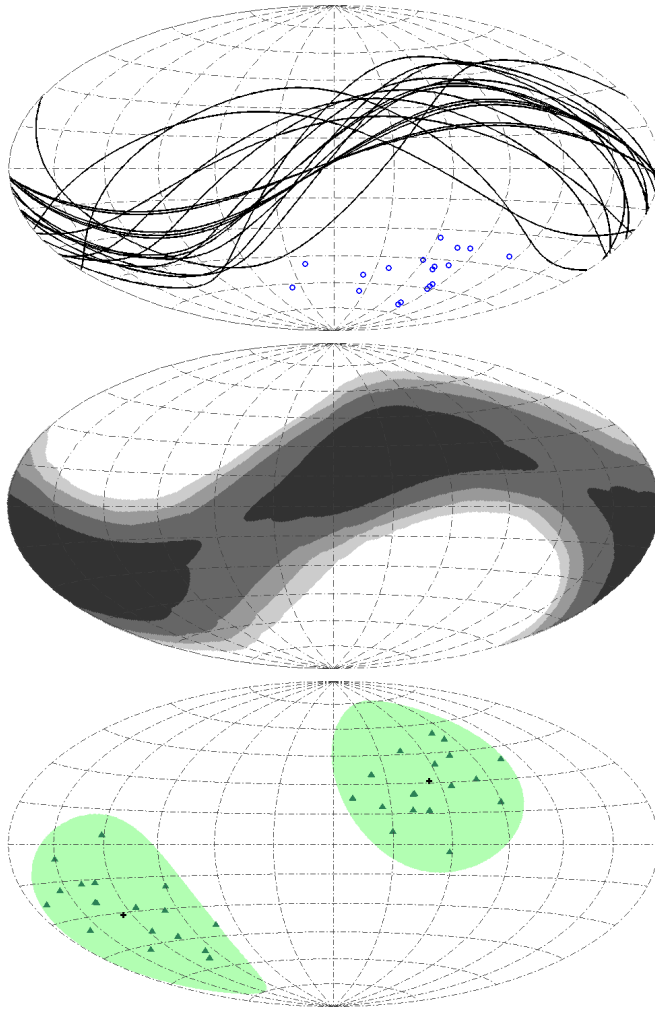


Figure 1.14: The new method at work. Top: Small blue circles are source positions. Continuous lines are geometrical loci of the corresponding polarization points. The probability distributions are computed at each location from the arclength of geometrical loci embedded in the cap. Middle: Density contours of the mean densities of the distributions evaluated at each location of the sphere. The darker the shades, the higher the expected densities. Bottom: Observed densities  $o_a$  are evaluated by counting the number of polarization points (triangles) falling in each cap. We evaluate the cumulative probabilities from the  $o_a$  and the  $P_n^a$  distributions. The alignment direction (black crosses) is defined as the centre of the cap (green patches) showing the most unexpected over-density. Hammer-Aitoff projected maps are centred on the Galactic centre with positive Galactic latitude at the top and longitude increasing to the right.

of the polarization PA distributions inside relatively small regions of the sky and because the declinations of these regions are not too high, we expect the changes to be small.

## Chapter 2

# A new analysis of quasar optical polarization alignments

This chapter is devoted to the application of our new statistical method to the catalogue of optical polarization measurements for the 355 quasars compiled by Hutsemékers et al. (2005). This analysis was originally presented in (Pelgrims & Cudell 2014).

Since the PC test is entirely independent of the S and Z tests that have been applied by Hutsemékers et al. (1998; 2001; 2005) and by Jain et al. (2004), this new analysis is an independent search for the characterization of the polarization vector orientations of this sample.

The results returned by the PC test depend only on the value  $\eta$  of the aperture half-angle of the spherical caps which is used. From the jackknife treatment in Section 1.2.5, we have seen that, for a same parent sub-sample, the value of  $\eta$  that maximizes the detection of the alignments strongly fluctuates and that the local probability  $p_{\min}$  can go up or down by a factor of the order of 3. This behaviour comes from the fact that  $\eta$  takes into account the spread of the sources on the sky and that the PC test is subject to edge effects. To circumvent this problem in this analysis, we choose to fix the angle  $\eta$  at  $45^\circ$ . Therefore, the local and global significance levels that we give in the remainder could be slightly improved by choosing a different value of  $\eta$  for each sample. With this fixed value of  $\eta$ , we can scan the polarization sphere with caps, and assign a value of  $p_{\min}$  to each. The most significant deviations can be kept and we can numerically evaluate the global significance  $p^\sigma$  for the same sample. This can be done not only on the full data sample, but also on sub-samples corresponding to regions of redshift, declination or right ascension, or to cuts on the degree of linear polarization.

In the following sections, we thus apply the PC test to the sample first globally and then to slices in redshift. There, we also consider the dependence of the alignments on the various parameters, extract the most significant regions exhibiting an anomalous alignment of polarization vectors and finally highlight the possibility of a cosmological alignment that

Sample	$p_{\min}$	$(\delta, \alpha)_{a_{\min}} (^{\circ})$	$o_a/o_a^{\max}$	$(\delta, \alpha)_{\langle e_r \rangle} (^{\circ})$	$p^{\sigma}$
Whole	$1.5 \cdot 10^{-2}$	(48.6, 283.7)	163/318	(5.5, 185.0)	0.14
Northern sky	$9.3 \cdot 10^{-2}$	(23.1, 294.0)	82/173	(12.2, 197.2)	0.58
Southern sky	$5.1 \cdot 10^{-5}$	(39.7, 270.6)	89/142	(−0.7, 358.5)	$6.0 \cdot 10^{-4}$

Table 2.1: Parameters of the most significant caps obtained with  $\eta = 45^{\circ}$ .

involves sources from both hemispheres.

## 2.1 Full sample

The full sample of quasars is naturally split into Galactic North and Galactic South because the observations are away from the Galactic plane, so that besides the whole sample, we shall also consider all the northern quasars or all the southern ones. Each sample has respectively 355, 195 and 160 sources. We consider all the possible spherical caps, and show the most significant ones in Table 2.1. The first column gives the most significant p-value, the equatorial coordinates in the polarization space  $(\delta, \alpha)_{a_{\min}}$  of the centre of the most significant cap, and the ratio of the number of quasars within the cap to the maximum number,  $o_a/o_a^{\max}$ . We also give the angular coordinates of the vector  $\langle e_r \rangle$  resulting from the normalized sum of the position vectors of the  $o_a$  sources and the global significance level  $p^{\sigma}$  of the alignment.

From this table, one sees that nothing is detected in the whole sample or in the northern one. On the other hand, an alignment is detected towards the Galactic South. One may wonder then how it was possible to find the significant alignments A1 and A2 towards the Galactic North, as in Tables 1.1 and 1.2. The reason for this is that so far we have considered all data points, i.e. all redshifts, all declinations, and all right ascensions. The fact that there is an alignment to the South and not to the North tells us that the effect depends on the physical position of the sources. Hence when we consider all sources, we average the effect, and can simply destroy it.

To illustrate this, we can consider the redshift distribution of the quasars contributing to the alignment seen towards the Galactic South. Simply counting the aligned quasars in regions of redshift is not enough, though, as the statistics of the sample varies, and as only some quasars have trajectories in polarization space that can intercept the considered cap. However, we have already the required tool: for a fixed cap, we can consider slices of redshift and their p-value. Fig. 2.1 shows the p-values of slices in which there is an excess of density. We can clearly see in it that the alignment is concentrated in a reduced region of redshift starting at  $z = 0.8$ .

It is indeed known that the directions of large-scale alignments of optical polarization orientations of quasars show a dependence on the redshift of the sources (see Hutsemékers et al. 1998; 2001; 2005; 2010 and Jain et al. 2004). Hence studying the effect globally may



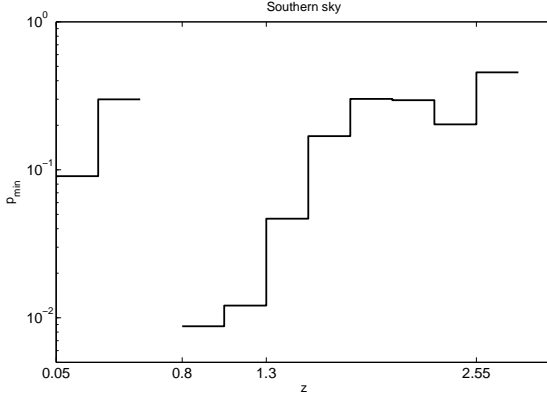


Figure 2.1: The p-value distribution of the slices of redshift that show an excess of aligned polarizations towards the direction of the most significant cap identified in Table 2.1, for quasars of the southern sample. Redshift bins have a width of  $\delta z = 0.25$ .

not make sense, and different alignments at different redshifts may cancel each other. Also, if only some regions of redshift have an alignment effect, then it can get washed out globally. Concentrating on the most significant region of Fig. 2.1 is not consistent either, as the cap which it is built from is influenced by the unaligned quasars at high and low redshift. In the next section, we shall develop a method to determine the regions of redshift where the quasars are strongly aligned.

## 2.2 Redshift dependence

The problem is thus to make a blind analysis of the redshift dependence of the alignment. To do so, we consider a slice of redshift  $[z_{\min}, z_{\max}]$  and calculate the p-value of the quasars falling in it. We then vary  $z_{\min}$  and  $z_{\max}$  on a grid. The size of the steps  $\delta z$  in  $z_{\min}$  and  $z_{\max}$  will of course depend on the statistics of the data.

We show the redshift distribution of the data in Fig. 2.2. We see that the high-redshift data points ( $z > 2.5$ ) are few, and that there is another deficit in the southern sample in the region  $[1.5, 1.7]$ . Also, we see that bins of width  $\delta z = 0.1$  allow reasonable statistics for most redshifts.

We can now consider all the values of  $z_{\min}$  and  $z_{\max}$  on a grid of spacing 0.1 (we also exclude the one quasar with  $z > 3$ ). As our test does not use the quasar position (although it depends on it), we do not need to introduce further cuts by hand as in (Hutsemékers et al. 1998 and 2005). We nevertheless consider the whole sample, and the northern and southern regions separately. We show in Fig. 2.3 the result of this study. For a given region  $[z_{\min}, z_{\max}]$  we show the value of  $p_{\min}$  as different shades of grey, the darkest regions being the most significant. Clearly, the dependence on redshift does not seem to be continuous: the alignment is present for some redshift and not for others. In particular, all regions present alignments at small  $z_{\min}$ , the northern hemisphere has one further clear alignment starting

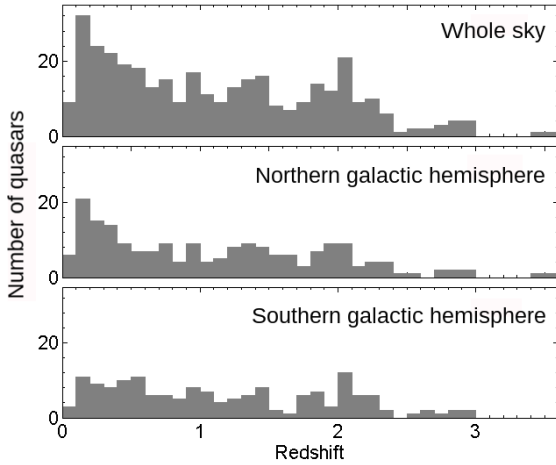


Figure 2.2: The redshift distribution of the sample of 355 quasars with bin width of  $\delta z = 0.1$  are shown for the whole sky, the northern Galactic hemisphere and the southern Galactic hemisphere. The last bin in the histograms of the whole sky and northern part contains the quasar at  $z = 3.94$ .

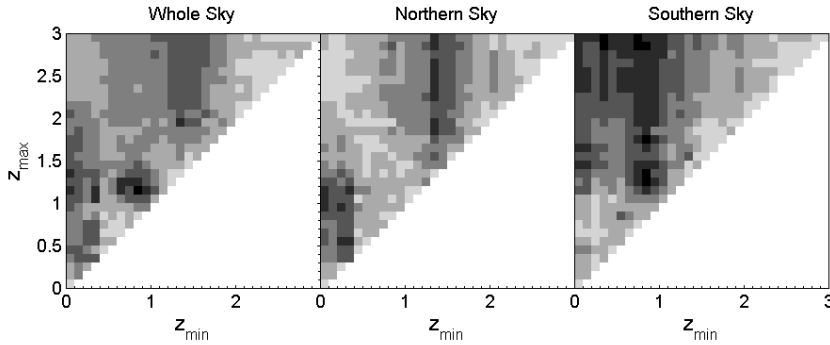


Figure 2.3: Contour plots of  $p_{min}$  as a function of the minimum and maximum values of the redshift, for the whole sample, for the Galactic North and for the Galactic South. Values from  $10^{-6}$  to  $10^{-5}$  are in black, and the different nuances of grey correspond to factors of 10, up to the white regions, which are for  $p_{min}$  between 0.1 and 1.

Sample	$z_{\min}$	$z_{\max}$	$p_{\min}$	$(\delta, \alpha)_{a_{\min}} (^{\circ})$	$o_a/o_a^{\max}$	$(\delta, \alpha)_{\langle e_r \rangle} (^{\circ})$	$p^{\sigma}$
W0	0.3	1.1	$2.9 \cdot 10^{-5}$	(20.7, 304.3)	60/99	(16.9, 203.3)	
W1	0.8	1.2	$7.3 \cdot 10^{-6}$	(25.4, 278.1)	31/40	(12.2, 181.2)	
W2	1.3	2.0	$8.3 \cdot 10^{-5}$	(76.0, 304.7)	53/80	(10.2, 32.4)	
<b>WCo</b>	<b>1.3</b>	<b>2.0</b>	<b><math>4.3 \cdot 10^{-6}</math></b>	<b>(65.9, 293.1)</b>	<b>39/50</b>	<b>(−9.3, 3.5)</b>	<b><math>2.7 \cdot 10^{-5}</math></b>
<b>N0</b>	<b>0.2</b>	<b>0.6</b>	<b><math>1.4 \cdot 10^{-5}</math></b>	<b>(15.0, 308.2)</b>	<b>28/37</b>	<b>(22.3, 208.4)</b>	<b><math>1.8 \cdot 10^{-4}</math></b>
N1	0.3	1.2	$1.5 \cdot 10^{-5}$	(12.7, 305.0)	40/58	(19.3, 206.4)	
<b>N2</b>	<b>1.3</b>	<b>2.0</b>	<b><math>3.5 \cdot 10^{-5}</math></b>	<b>(78.2, 298.1)</b>	<b>35/47</b>	<b>(5.8, 186.6)</b>	<b><math>3.4 \cdot 10^{-4}</math></b>
S0	0.3	2.9	$8.1 \cdot 10^{-6}$	(44.7, 273.8)	79/120	(−5.0, 357.1)	
S1	0.7	3.0	$3.1 \cdot 10^{-6}$	(43.6, 272.3)	62/89	(−7.0, 357.6)	
<b>S2</b>	<b>0.8</b>	<b>1.3</b>	<b><math>3.9 \cdot 10^{-6}</math></b>	<b>(31.8, 263.9)</b>	<b>19/20</b>	<b>(−7.8, 348.3)</b>	<b><math>3.0 \cdot 10^{-5}</math></b>

Table 2.2: Significant sub-samples from the scan on redshift performed on the whole sample of 354 quasars and the northern and southern samples of 194 and 160 sources, respectively. Best cap parameters are shown as in Table 2.1 as well as the lower and upper limits in redshift of sub-samples. Note that region WCo is detected for  $p_{\min} \leq 1.5\%$ . Bold characters stress the most significant independent regions (see the text for a discussion).

at  $z = 1.3$ , whereas the southern hemisphere has a significant alignment starting at  $z = 0.8$ . We see that for each sample, the redshift slices that show significant alignment are grouped in several islands in the  $(z_{\min}, z_{\max})$  plane. For each island we retain the most significant sub-sample. The parameters of these nine sub-samples and of the corresponding most significant caps are given in Table 2.2. In this table, sub-samples are quoted by letter which indicates their original samples; namely, W, N and S indicate if they are extracted from the whole sky, from the northern sky or from the southern sky (in Galactic coordinates). Note that the sub-sample named WCo will be introduced and discussed in Section 2.2.2.

It may be worth insisting on the fact that cuts in redshift, (or in declination and right ascension, see further subsections) amount to the consideration of data sub-samples with lower statistics. In that case, our method leads to higher values of  $p_{\min}$  if an alignment effect is present, or to a similar value of  $p_{\min}$  if there is no effect. The fact that one can markedly increase the significance of the effect by using such cuts indicates that the effect of alignment is stronger for some regions of redshift (or for some regions on the celestial sphere).

The first thing to notice is that we indeed find possible regions of alignment towards the Galactic South. However, we must decide whether they are all significant and independent, as a very significant region can always be somewhat extended by adding to it some noise. To decide, we can proceed as in the case of Fig. 2.1, and cut this time each sample in slices of redshift, declination and right ascension. The results of such a study are shown in Fig. 2.4 for all the regions of Table 2.2. If for now we concentrate on the last three columns of the southern regions (last three lines) in Fig. 2.4, we see the structure of S0, S1 and S2. The distributions in right ascension and declination tell us that the quasars that contribute most are in the same region of the celestial sphere, which is confirmed by the

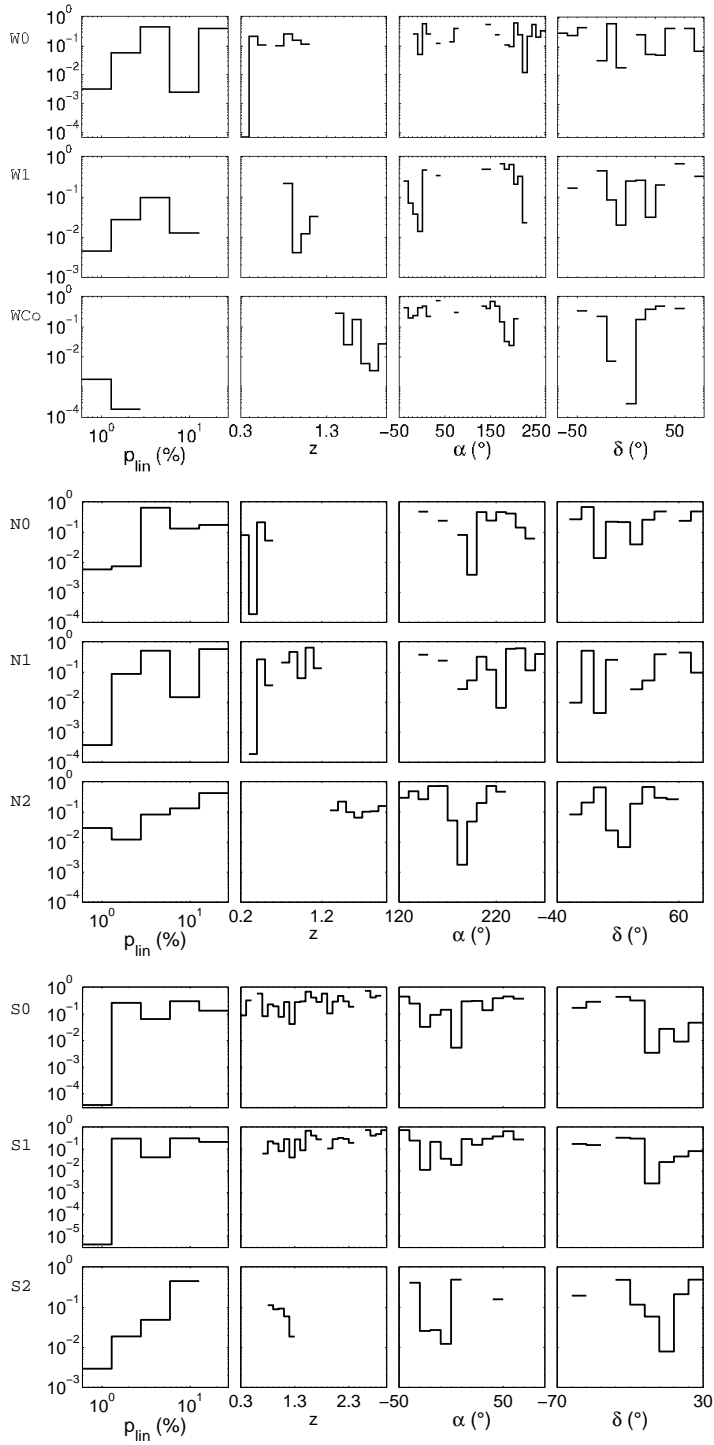


Figure 2.4: Fine structure of the regions of Table 2.2. The ordinates gives the p-values for excess in the sub-regions defined by the bins in the abscissae. Deficits are not shown.

7th column of Table 2.2 that gives the average position on the sky. Also, the 5th column of Table 2.2 shows that the alignment is in the same direction for S0 and S1, and almost in the same direction for S2 (remember that the caps have an aperture of  $45^\circ$ ). Hence it seems that there is a very strong alignment (to which 19 quasars out of 20 contribute) for the limited redshift region  $0.8 < z < 1.3$ , and that alignment can be extended to higher or lower redshift, without changing its significance much. As increasing the number of sources should markedly decrease the p-value if they also have aligned polarization vectors, we believe that only S2 is significant.

We can perform the same analysis for the northern quasars. Considering again the last three columns, and this time the fourth, fifth and sixth lines of Fig. 2.4, we see that N0 and N1 are populated by quasars in the same region of the celestial sphere, and that N1 is the same as N0, but extended in redshift. Table 2.2 confirms that the average position on the sky is very close, and that the preferred directions of polarization are almost identical. It thus seems that N0 is the significant region, as N1 has more statistics, but less significance. On the other hand, Table 2.2 clearly shows that N2 is disjoint from N0 and N1 in redshift and that the preferred directions of alignments are significantly different. Indeed, the angular change is of the order of  $70^\circ$  which is reminiscent of result already obtained by Hutsemékers et al. (2005) which is somehow illustrated in Fig.1.

Finally, we can consider the first two lines of Fig. 2.4. We see, looking at the plot in right ascension, that the most significant part of W0 is towards the Galactic North, whereas W1 is more significant towards the Galactic South. Table 2.2 shows that the direction of alignment of W0 (resp. W1) is compatible with that of N0 (resp. S2). Furthermore, we see that the most significant quasars of W0 fall in the same redshift bin as those of N0. Hence it seems that W0 is really a reflection of N0. Similarly, the p-values are smallest in W1 for the same redshift as for S2, and it seems that W1 is really generated by S2.

We have checked these conclusions by separating W0 and W1 into their northern and southern parts and by performing the study independently for these two parts. If p-values of both parts are all higher than the value of  $p_{\min}$  of the whole, and point towards the same preferred direction, then it is clear that the observed alignment is produced by sources from both hemispheres. In the case of W0 (resp. W1) we find that the northern (resp. southern) alignment is much more significant.

### 2.2.1 Fine structure and best regions

We can study the structure of each region, and check whether it can be better defined by using further cuts. Consider the first column of Fig. 2.4, i.e. cuts on linear polarization. We do not find, for N0, N2 and S2, that cuts in linear polarization increase the effect significantly (i.e. that  $p_{\min}$  gets reduced by more than a factor of two). The reduced significance of the bins with large polarization is due to their lower statistics.

On the other hand, the dependence on right ascension and declination suggests that some

Sample	$z_{\min}$	$z_{\max}$	$p_{\min}$	$(\delta, \alpha)_{a_{\min}} (^{\circ})$	$o_a/o_a^{\max}$	$\delta$ interval ( $^{\circ}$ )	$\alpha$ interval ( $^{\circ}$ )	$p^{\sigma}$
N0	0.2	0.6	$1.4 \cdot 10^{-5}$	(15.0, 308.2)	28/37	$[-25, 80]^*$	$[135, 265]^*$	$1.8 \cdot 10^{-4}$
N2+	1.3	2.0	$4.5 \cdot 10^{-6}$	(79.8, 289.3)	30/35	$[-30, 35]$	$[165, 230]$	$5.0 \cdot 10^{-5}$
S2+	0.8	1.3	$1.9 \cdot 10^{-6}$	(31.8, 261.2)	18/18	$[-55, 25]^*$	$[-40, 20]$	$1.0 \cdot 10^{-5}$

Table 2.3: Best independent regions of alignment. The regions in  $\delta, \alpha$  marked by an asterisk describe the data sample, the others are cuts imposed on the data. N0 is the same as in Table 2.2. S2+ and N2+ are restrictions of S2 and N2 to a smaller region of the celestial sphere.

regions of the sky are more significantly aligned. From this observation, we can define even more significant regions, by placing cuts on right ascension and declination. This does not lead to a significant difference, except for regions N2 and S2. Following the above argument, it seems that we have detected three independent regions of alignment, which are significant. We summarise their parameters in Table 2.3. Note that N0, N2+ and S2+ are improved versions of A2, A1+ and A3 defined by Hutsemékers et al. (2005).

### 2.2.2 A possible cosmological alignment

Although cutting on polarization does not improve significantly the previous probabilities, we detected a rather surprising alignment, as it is very significant only when the North sample is considered together with the southern one. Indeed, if we consider only small linear polarizations, with  $p_{\text{lin}} \leq 1.5$  per cent, then there is a North-South alignment with  $p_{\min} < 5 \cdot 10^{-6}$ , as shown in the sample WCo of Table 2.2. This alignment is much less significant in the North ( $p_{\min} \approx 2 \cdot 10^{-4}$ ) or in the South ( $p_{\min} \approx 10^{-3}$ ), but it becomes significant once both hemispheres are considered together. It must also be noted that it is significant only after the cut on linear polarization.

### 2.2.3 A naive interpretation

One can imagine that a systematic oscillating electric field  $\mathbf{E}$  is at work in each of the regions we defined. We can try to determine its norm and take it parallel to the centre of the polarization cap  $\hat{s}_{\text{centre}}$ , in such a way that the alignments we found disappear if we subtract that systematic effect from the samples we defined (in practice we impose that  $p_{\min} \geq 0.1$ ). Of course, we have first to project  $\mathbf{E}$  onto the plane normal to the direction of propagation, then remove it from the polarization. If we perform this exercise, the resulting values of  $|\mathbf{E}|$  are given in Table 2.4 for the most significant regions of Table 2.2. It is remarkable that the vectors we have to remove from the data have roughly the same norm. Due to the projection of the vector  $\mathbf{E}$ , this naive model could explain why polarization vectors are not all seen to be aligned.

Sample	$ E $ (%)
N0	0.65 – 0.70
N2	0.6 – 0.7
S2	0.8 – 1.2
WCo	0.5 – 0.9

Table 2.4: Norm of a systematic 3-vector accounting for the effect.

## 2.3 Concluding remarks

In this chapter, we performed a new analysis of the catalogue of the 355 quasar polarization measurements at optical wavelengths compiled by Hutsemékers et al. (2005). Based on this data set, and from earlier versions, previous analyses have reported evidence for coherent orientations of quasar polarization vectors at very large scales. The quasars involved in these correlations are indeed separated by gigaparsec-scale comoving distances (see Jain et al. 2004 and Hutsemékers et al. 2005). These analyses, however, rely on the use of the same two statistical methods, the S and Z tests that we discussed in Sections 1.1.1 and 1.1.2. Our analysis, though, is performed with the statistical test that we introduced in Section 1.2 which is independent from the two others. Hence, our analysis is complementary, although the same data set is under study. Furthermore, the new method allowed us to extract in an unbiased way the sub-samples that show significant correlated polarization orientations.

The application of the PC test to the optical sample of quasar polarizations confirms the large-scale polarization alignments. We showed that we automatically recover regions previously found, and we refined their limits based on unbiased criteria (see Table 2.3). We believe that this new analysis puts the alignment effect on stronger grounds as the global significance level is as low as  $3.0 \times 10^{-5}$  for some regions of space.

However, one has to note that the significance levels obtained in this chapter and those reported by Hutsemékers et al. (2005) are not in full agreement. The main reason that accounts for these differences is that these authors generated random catalogues through the reshuffling in order to assess the significance levels of the correlations with the S and Z tests. The advantage is that any systematic effect vanishes automatically through this method. The disadvantage is that it washes out global effects, or alignments present for a large number of quasars. Random generation of polarization angles, as used here or also by Jain et al. (2004), has the opposite features: we can detect global alignments, but we are sensitive to systematic effects. Hence the two methods do not need to be in full agreement. One should note, however, that the sample of optical polarization measurements of quasars considered here comes from many independent observational campaigns, so that a common bias is unlikely (see Hutsemékers et al. [1998; 2005] for discussion). Furthermore, Jain et al. (2004) have

addressed this question of global systematic effect with the sample of 213 quasar polarization measurements available at the time by comparing analyses with the S and Z tests using uniform polarization angle distributions and distributions made by reshuffling. For some sub-samples, they found that the significance levels increase by factors of the order three when the generation of random data set is made through reshuffling. We expect to obtain the same difference for the global significance level obtained with our test ( $p^\sigma$ ) if we generate random catalogue with reshuffling instead of generating the position angles according to a uniform distribution. Note that this difference is also of the same order as that we estimated using the jackknife method. To conclude, our analysis is found to be in good agreement with the previous ones.

Through the PC test, we identified the following main features of the alignments. The directions of alignments show a dependence on the redshift of the sources. Although this dependence seems discontinuous, one should note that we detected significant alignments for redshift intervals where the distribution of data peaks. Thus, more data in regions of redshift with poor statistics are required in order to study this dependence in more details. Further, as seen in Fig. 2.4 for a given redshift interval, alignments seem to be mainly due to quasars well localized towards specific directions of the sky, again in agreement with previous studies. However, no strong evidence has been found for a dependence on the degree of linear polarization. This result is slightly at odds with previous claims even though Hutsemékers et al. (2005) specifically cautioned that their findings can be due to selection biases in their data set.

As a result of the application of our new method to the present sample of optical polarization measurements of quasars, and in agreement with Hutsemékers et al. (2005), we found several distinct sub-samples of sources well localized in space that show unexpected alignments of their polarization vectors. We established two regions towards the North Galactic pole, one at low and the other at high redshift, and only one towards the South Galactic pole at intermediate redshift, which possibly dominates the whole southern sky. Besides the regions previously detected, or their improved version, we also showed that there exists the possibility of a cosmological alignment.



## Chapter 3

# A search for quasar radio polarization alignments

Jackson et al. (2007) compiled the JVAS/CLASS 8.4-GHz sample of flat-spectrum radio sources (FSRS), paying particular attention to instrumental biases. This sample contains polarization position angle (PA) measurements. As they have shown, rotation measures of the polarization vectors induced by Faraday rotation at 8.4 GHz are too small to destroy information about the intrinsic PAs. Therefore, any observed correlation of PAs among sources can be thought to be intrinsic to the sources themselves. Joshi et al. (2007) extracted from this sample 4290 FSRSs with polarized flux higher than 1 mJy, and searched for systematic alignments of radio polarization vectors of the type reported at optical wavelengths by Hutsemékers and collaborators, i.e. at cosmological scales. Their analysis did not reveal such large-scale alignments at radio wavelengths. From this claim, the recognized wavelength dependence of the polarization vector alignments has brought the model of axion-like particle (e.g., Das et al. 2005; Payez, Cudell & Hutsemékers 2008; Agarwal, Kamal & Jain 2011) as the favourite candidate to explain alignments at optical wavelengths. This model has however been observationally ruled out since it predicts non-negligible circular polarization which is not detected (Hutsemékers et al. 2010; Payez, Cudell & Hutsemékers 2011).

Beside this analysis, Tiwari & Jain (2013) tested the uniformity of the polarization PAs considering roughly the same sample. They found significant evidence for alignments at distance scales of the order of 150 Mpc<sup>1</sup>. As the correlations are found at different distance scales, their study does not contradict the analysis of Joshi et al. (2007). More recently, Shurtleff (2014) studied the correlation of the PAs for sources grouped in circular regions of 24° radius. He reported PA alignments in two regions of the sky, although not at a very significant level.

---

<sup>1</sup>Attention has to be paid regarding this scale as these authors defined the comoving distances assuming a redshift of one for all objects. Their analysis is thus a 2-dimensional one rather than a 3-dimensional one, contrary to what the reported scale might suggest.

Despite these analyses which involve different statistical tests and different samples which correspond to different cuts of the original data set, the status of polarization PA correlation at radio wavelengths was not clear. Moreover, an analysis taking properly the redshift of the sources into account was still missing. The redshift dependence is an important characteristic of the alignments of quasar polarization vectors at optical wavelengths and it seemed important to take it into account in the analysis of the radio sample, especially if one seeks the same signature at radio wavelengths as at optical wavelengths. Therefore, we performed a careful analysis of the uniformity of the polarization PAs of FSRs belonging to the JVAS/CLASS 8.4-GHz surveys. This analysis (published in Pelgrims & Hutsemékers 2015) is presented in this chapter which is structured as follows.

The data samples which are studied throughout this analysis are introduced in Section 3.1. The sample with robust polarization measurements is made of 4155 objects and spectroscopic redshift information is collected for 1531 of them. In Section 3.2.1, taking the redshift of the sources into account, we shall investigate the polarization PA distributions of the FSRs located in regions of the sky where the optical polarization alignments are the most significant. Stimulated by the detection of alignment in one of these regions, we perform a complete analysis of the entire data set in Section 3.2.2, with and without accounting for the redshift. Having highlighted significant alignment signatures in the sample of quasars, we search for their characterization in Section 3.3. We finally summarize our results in Section 3.4, present arguments against and for the hypothesis of biases in the data set and discuss a possible interpretation of the data. We conclude in Section 3.5 either that the data set of the polarization angle measurements of the JVAS/CLASS 8.4-GHz surveys are not exploitable due to biases or that they suggest large-scale alignments at radio wavelengths. Indeed, as we shall see, two statistical analyses (one in two dimensions and the other in three dimensions when distance is available), detect significant large-scale alignments of polarization vectors for samples containing only quasars among the varieties of FSRs. While these correlations prove difficult to explain either by a physical effect or by biases in the data set, the fact that the quasars which have significantly aligned polarization vectors are found in regions of the sky where optical polarization alignments were previously found is striking.

### 3.1 Data sample

The JVAS/CLASS 8.4-GHz catalogue is made of the JVAS (Jodrell-VLA Astrometric Survey) and the CLASS (Cosmic Lens All-Sky Survey) surveys that were gathered by Jackson et al. (2007) to build the largest catalogue of polarization measurements of compact radio sources at that time, paying attention to avoid biases on polarization measurements. We refer to Jackson et al. (2007) and references therein for a complete description of the catalogue and the surveys. In this catalogue, the total number of object having polarization measurements

is 12743 (see the on-line catalogue<sup>2</sup>). Adopting the prescription given by Jackson et al. (2007) and Joshi et al. (2007), we keep the sources for which the polarized flux is higher or equal to 1 mJy in order to select significant polarization detections only and to obtain an unbiased sample. Jackson et al. (2007) claim that this cut in polarized flux corresponds to a significant polarization detections at the level of approximately  $4\sigma$ . When there is more than one object in a radius of 1 arcsec on the sky, we select the object with the highest polarized flux. This selection, which also eliminates multiple measurements, leaves us with a sample size of 4265 objects. If we only remove multiple measurements, we recover the source number of 4290 studied by Joshi et al. (2007). We nevertheless choose to add the above constraint for an efficient source separation.

The data table of Jackson et al. (2007) contains the following information for the sources: right ascension, declination, Stokes parameters ( $I$ ,  $Q$  and  $U$ ), the corresponding errors ( $\sigma_I$ ,  $\sigma_Q$  and  $\sigma_U$ ) and the derived polarization position angle ( $\psi = (1/2) \arctan(U/Q)$ ) in the East-of-North convention. From these data and according to the usual definition for the degree of linear polarization, we define  $p_{\text{lin}} = (u^2 + q^2)^{1/2}$ , where we make use of the normalized Stokes parameters  $u = U/I$  and  $q = Q/I$ . We then compute the standard error  $\sigma_p$  and  $\sigma_\psi$  for  $p_{\text{lin}}$  and  $\psi$  which are given by the Serkowski's formulae (Serkowski 1958; Naghizadeh-Khouei & Clarke 1993)

$$\sigma_p = \frac{(q^2 \sigma_q^2 + u^2 \sigma_u^2)^{1/2}}{p_{\text{lin}}} \quad (3.1)$$

and

$$\sigma_\psi = \frac{(u^2 \sigma_q^2 + q^2 \sigma_u^2)^{1/2}}{2p_{\text{lin}}^2}. \quad (3.2)$$

Given that  $\sigma_p \simeq \sigma_q \simeq \sigma_u$  is verified in general (e.g., Lamy & Hutsemékers 2000), the usual equation for the uncertainty on the polarization position angle reads

$$\sigma_\psi = \frac{\sigma_p}{2p_{\text{lin}}} \text{ rad} = 28.^\circ 65 \frac{\sigma_p}{p_{\text{lin}}}. \quad (3.3)$$

Led by a selection criterion used at optical wavelengths to ensure a significant polarization detection (e.g., Hutsemékers 1998; Sluse et al. 2005), we further constrain the sample asking that the uncertainty of the position angle, computed as in Eq. 3.3, verify  $\sigma_\psi \leq 14^\circ$ . While the cut at 1 mJy ensures significant polarization detection, our additional cut has to be seen as an additional quality criterion. Out of the 4265 sources, 4155 satisfied the criterion. This sample, which we call *All* in the reminder, constitutes the largest one for which we have robust polarization PA measurements from the JVAS/CLASS 8.4-GHz surveys. The sky projection of the sample *All* is shown in Fig. 3.1.

Using the NASA Extragalactic Database<sup>3</sup> (NED), we identified a total of 3858 sources. We first used the automated mode "Near-Object/Position List" with a search radius of 0.1

<sup>2</sup><http://vizier.u-strasbg.fr/viz-bin/VizieR-3?-source=J/MNRAS/376/371>

<sup>3</sup><http://ned.ipac.caltech.edu/>

arcsec. After manual selection among multiple identifications, 3446 objects were kept. For the 709 objects left, we used a search radius of 0.5 arcsec and found 412 additional sources, after having again manually took care of the multiple identifications. We stopped the procedure at this value of the search radius in order to ensure proper identifications. Out of the 3858 retrieved objects, 1531 have spectroscopic, and thus reliable, measurements of redshift,  $z$ . The use of NED also leads to the classification of the sources. Table 3.1 reports the number of sources identified for each class of FSRs as well as the number of these sources for which we have redshift information.

$z$	Object Type	$N$	Acronym
no	All	3858	—
	QSOs	1450	<i>QSO</i>
	Radio Sources	1379	<i>RS</i>
	Galaxies	381	<i>G</i>
	Other Objects	648	<i>VO</i>
yes	All	1531	<i>All(<math>z</math>)</i>
	QSOs	1325	<i>QSO(<math>z</math>)</i>
	Radio Sources	11	—
	Galaxies	184	—
	Other Objects	11	—

Table 3.1: Number ( $N$ ) of the object from different source species as retrieved from the NED database among the sample of 4155 sources with reliable polarization PA measurements, with and without redshift information,  $z$ . The last column contains the acronyms used for the samples that we analyse in this work. The category named “Other Objects” contains various species with small number of members.

As it can be clearly seen, the QSOs represent 86% of the sample with redshift measurements. Hence, analyses and results involving samples with redshift information will mainly concern those objects. Following Jackson et al. (2007), the core-dominated FSRs are predominantly quasars or BL Lac objects in which the jet is oriented close to the line of sight. We nevertheless choose to adopt the notation of the NED database. Throughout this chapter, we will thus refer to the sub-samples of QSOs and Radio Sources via the acronyms *QSO* and *RS*.

## 3.2 Uniformity of radio-polarization PAs

### 3.2.1 Regions of optical polarization alignments

As we already discussed in the previous chapters, specific regions of the sky for which polarization PAs of quasars are found to be aligned at optical wavelengths have been identified. In the original analysis (Hutsemékers 1998), the two most significant regions were identified by eye and were called A1 and A3. Hutsemékers et al. (2005) showed that it is actually from these regions that comes from most of the alignment signal (see for example Fig. 2). In the latter and independent identification (presented in Chapter 2), we used an unbiased method and highlighted the regions N2 and S2 containing significant alignments of the quasar po-

larization vectors. While less extended, the latter two regions were consistently found at similar locations in the 3-dimensional space. Here, as the sky coverage of the radio surveys and the optical catalogue are different (see below), we choose to consider the most extended regions (A1 and A3) to ensure an overlap as big as possible. Furthermore, those regions have been the subject of various studies in the past. We recall their boundaries here:

- A1:  $168^\circ \leq \alpha \leq 218^\circ$  ;  $\delta \leq 50^\circ$  and  $1.0 \leq z \leq 2.3$
- A3:  $320^\circ \leq \alpha \leq 360^\circ$  ;  $\delta \leq 50^\circ$  and  $0.7 \leq z \leq 1.5$

where  $\alpha$  and  $\delta$  refer to the right ascension and the declination of the sources, respectively.

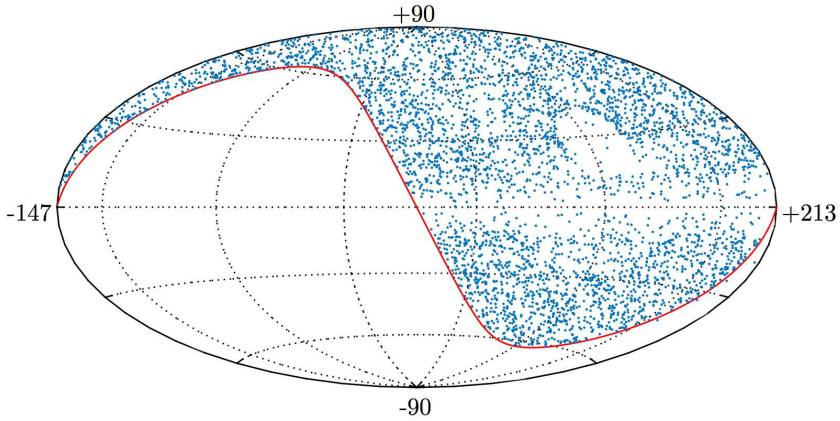


Figure 3.1: Hammer-Aitoff projection of the positions of the 4155 FSRs in the sample *All* (blue dots) in Galactic coordinates. The red line corresponds to the equator of the equatorial coordinates. The map is centred at Galactic longitude  $l_{\text{gal}} = 33^\circ$  for comparison of the sky distribution of the optical sample in Fig. 2.

Joshi et al. (2007) addressed the question of uniformity of the polarization PAs of FSRs from the JVAS/CLASS 8.4-GHz surveys in these regions and reported no obvious alignment. However, they did not introduce the cuts in redshift and thus, only considered the windows towards the A1 and A3 regions, defined by cuts in right ascension and declination only. As the redshift of the sources is an important characteristic of the alignments of optical polarization PAs, we perform a new analysis of these regions. It is nevertheless important to realize that the sky coverages of the JVAS/CLASS FSRs and the studied quasars at optical wavelengths are different. In particular, the surveys at radio wavelengths do not contain data at  $\delta < 0^\circ$  and the optical data set is limited in Galactic latitude as  $|b_{\text{gal}}| \geq 30^\circ$ . The differences of the sky coverages of the two sample can be noted by comparison of Figs. 2 and 3.1.

To study the polarization PA distributions of the A1 and A3 regions, we use the Hawley–Peebles test (Hawley & Peebles 1975 and Godłowski 2012) and the PC test introduced in

	A1 region		A3 region	
	$All(z)$	$QSO(z)$	$All(z)$	$QSO(z)$
$N$	141	139	50	45
$P_{\text{HP}} (\%)$	95.43	93.15	4.19	0.96
$\bar{\psi} (^\circ)$	—	—	64	62
$p_{\text{min}} (\%)$	$\geq 4$	$\geq 5$	0.01	$7.2 \cdot 10^{-4}$
$\eta (^\circ)$	20 – 90	20 – 90	58	56
$p^\sigma (\%) [N_{\text{sim}}]$	$\geq 13 [10^2]$	$\geq 10 [10^2]$	0.07 [ $5 \cdot 10^4$ ]	$4.0 \cdot 10^{-3} [5 \cdot 10^4]$
$\bar{\psi}_{\text{PC}} (^\circ)$	—	—	68	67

Table 3.2: Results of the Hawley–Peebles and the PC tests performed on the sub-samples corresponding to the A1 and A3 regions of optical polarization alignments. Sub-samples are obtained from both the  $All(z)$  and the  $QSO(z)$  samples.  $N$  is the size of the sub-samples,  $P_{\text{HP}}$  is the probability given by the Hawley–Peebles test that the PAs are drawn from a uniform parent distribution and  $\bar{\theta}$  is the mean polarization PA returned by this method.  $p_{\text{min}}$  is the local probability obtained with the PC test for the half-aperture angle  $\eta$  to which corresponds the minimum global probability  $p^\sigma$  computed with  $N_{\text{sim}}$  random simulations. The mean angle  $\bar{\theta}_{\text{PC}}$  is computed as explained in Section 1.2.5. Probabilities are given in percent.

Chapter 1. We refer to Sections 1.2 and 1.3 for a description of these statistical tests. Considering samples of sources that are in a small region of the sky, these tests return the probability that the observed distribution of PAs is random and define the mean PAs ( $\bar{\psi}$  and  $\bar{\psi}_{\text{PC}}$ , resp.) which are relevant only in the case of non-uniformity.

The Hawley–Peebles test analyses PA histograms. The number of bins is a free parameter. We decide to use 18 bins of  $10^\circ$  each, spanning the range  $0^\circ - 180^\circ$ . This choice does not maximize the reported probabilities but is somehow justified by the fact that a bin width of  $10^\circ$  corresponds approximately to twice the mean error of the polarization PAs under study.

The PC test involves spherical caps of equal area. This area is fixed by the angular aperture of the cap ( $2\eta$ ) which is the only free parameter of the test. As discussed in the Section 1.2.5, it is useful to investigate a large range of values for  $\eta$ . Therefore, we explore here the range  $2^\circ - 90^\circ$  for  $\eta$  and we report the probabilities  $p_{\text{min}}$  and  $p^\sigma$  corresponding to the value of  $\eta$  for which  $p^\sigma$  is the smallest.

Results of the tests applied to the sub-samples extracted from the  $All(z)$  and the  $QSO(z)$  samples are shown in Table 3.2. The hypothesis of uniformity of the polarization orientations is rejected at the level of at least 95% in the A3 region but not in the A1 region<sup>4</sup> in both sub-sample  $All(z)$  and  $QSO(z)$ . The detection of an alignment is very intriguing, espe-

<sup>4</sup>At first glance, the fact that we found alignment in the A3 region but not in the A1 region could be caused by a bad spatial overlap between radio and optical data in the A1 region. But the overlapping is not better in the A3 region.

cially given the claim by Joshi et al. (2007). To reconcile the analyses, we extracted the A3 window from the entire sample of 4155 FSRs. Applying our tests to this sub-sample of 385 sources, we did not find any evidence for alignment. This test confirms the negative result of Joshi et al. (2007) stating that there is not alignment of the radio polarization vectors inside the A1 and the A3 windows (see Table 3.3 and Section 3.2.3 for further related discussions).

Our analysis of the A1 and A3 regions, however, contradicts the claim of Joshi et al. (2007) which states that no alignment is present at radio wavelengths (8.4 GHz) inside the regions where the optical polarization vectors are found to be coherently oriented. This contradiction is likely due to the redshift cuts but could also be due to the fact that the radio polarizations of QSOs are aligned whereas the polarization of the other FSRs are not.

It is therefore of interest to find out whether the alignment tendency observed in this region is an isolated structure inside the sample of FSRs or part of a major trend which was not recognized earlier. To this end, we shall address the question of uniformity of the polarization PAs for the complete JVAS/CLASS 8.4-GHz surveys, without restriction on the sky location, taking redshift into account and considering the subdivision of the sample into the different species.

### 3.2.2 Full sky coverage

To study the uniformity of polarization angle distributions for the sample and sub-samples of the FSRs that are sparse and non-uniformly scattered on the celestial sphere, we shall use the S and Z tests that we introduced in Chapter 1. As we have seen, the S and Z tests are appropriate to assess the probability that the distributions of polarization PAs of local groups are due to statistical fluctuations considering the overall sample. We use these tests in this section. The intrinsically coordinate-invariant PC test (Section 1.2) being more useful for the characterization of correlations is used in Section 3.3. We do not use the other statistical tests as they are coordinate-dependent and that this dependence grows with the angular distance between sources. Hence, they are thus not adequate to test the uniformity of the PA distribution over large scales.

In Sections 1.1.1 and 1.1.2, we discussed extensively the coordinate-invariant S and Z tests. These nearest-neighbour tests compute the probability that the polarization PAs are uniformly distributed in spatially defined groups of objects, making use of Monte Carlo simulations. For each realization, the PAs are reshuffled among the sources of the entire sample and a statistics is computed for each group of  $n_v$  nearest neighbours. The percentage of Monte Carlo simulations having an average statistic ( $S_D$  or  $Z_c$ ) as extreme as the one of the data defines the significance level (SL) of the test, i.e., the probability that the observed PA correlations inside groups can be attributed to statistical fluctuations in the entire sample. For the samples of Table 3.1, we explore a wide range of values of the parameter  $n_v$  (see Section 1.1.3 for the motivation of doing this) and use a number of random simulations  $N_{\text{sim}} = 1000$ , except contraindication. We span the range 4 – 400 (with steps of 2 and 20

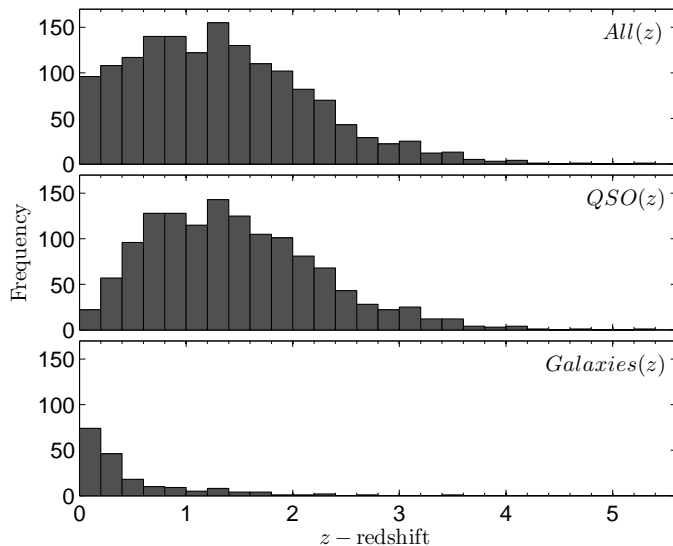


Figure 3.2: Redshift distributions of the sample  $All(z)$  and its sub-samples of QSOs and galaxies.

for ranges  $4 - 18$  and  $20 - 400$ , respectively), except for the sample of galaxies where we stop at  $n_v = 200$  for obvious reasons. Note that the lowest value of the SL does not provide an accurate estimate of the overall significance but gives instead the value of  $n_v$  at which the departure from uniformity is the most significant.

We will first consider samples for which reliable redshift measurements are available. For these samples, both 2- and 3-dimensional analyses are applied, i.e. defining nearest-neighbour groups on the celestial sphere or in the 3-dimensional comoving space respectively. We will then turn to the 2-dimensional analysis of the samples of Table 3.1 which are not constrained by redshift. For convenience, we give in Table 3.4 a summary of the results of these two tests applied to all the considered samples.

### Samples with redshift measurements

As already mentioned, the sample of 1531 sources for which reliable redshift measurement are available is composed at 86% of QSOs. The second important population of this sample is that of galaxies. The redshift distributions of these samples are shown in Fig. 3.2. Of course, the redshift distributions of the sample  $QSO(z)$  and that of galaxies do not follow the same trend.

**3-dimensional analysis.** We discuss our results in terms of a typical comoving distance  $\mathcal{L}$  instead of the free parameter  $n_v$  of the statistical tests. This typical scale is defined



as the median of the comoving distances between each central object and its  $n_v$ 'th nearest neighbour, the median being evaluated over the full sample under consideration. The line-of-sight comoving distances (see Section 1.1.3) are computed assuming a flat Universe with the cosmological parameters:  $\Omega_M = 0.31$  and  $H_0 = 68 \text{ km s}^{-1} \text{ Mpc}^{-1}$ , following Planck Collaboration XVI (2014). We show in Fig. 3.3 (*top*) the relation between the parameter value  $n_v$  and the typical comoving distance for the samples we analyse in 3 dimensions. We applied the statistical tests to the sample of 1531 objects and to the subcategory of QSO, namely  $All(z)$  and  $QSO(z)$ . We also considered the high redshift part of the latter, imposing  $z > 1$ . This restricted sub-sample is populated by 894 sources and is denoted  $QSO(z > 1)$ .

Results of the S and Z tests are shown in Fig. 3.3 (*middle* and *bottom*, respectively). We did not find any significant evidence ( $SL < 5\%$ ) over a wide range of value of  $n_v$  (or  $\mathcal{L}$ ) for alignment of the polarization PAs in the samples  $All(z)$  and  $QSO(z)$ . However a redshift dependence is possibly detected with the Z test as suggested in Fig. 3.3 (*bottom*). Indeed, in the high-redshift QSO sample, correlations of polarization PAs of sources inside groups of typical comoving radius  $\sim 2 \text{ Gpc}$  show a probability smaller than 1% of being due to statistical fluctuations.

**2-dimensional analysis.** The radial coordinates of the sources are fixed to  $r = 1$  (see Eq. 1.15) for the 2-dimensional analysis, even though redshift measurements are available. We discuss our results in terms of the typical angular separation  $\xi$ . The latter is defined as the median of the angular separation between each object of the sample and its  $n_v$ 'th nearest neighbour. Fig. 3.4 (*top*) shows the relation between  $\xi$  and  $n_v$  for the three samples.

We show the dependence of the SL on the typical angular separation  $\xi$  in Fig. 3.4. Significant correlations ( $SL < 5\%$  over a wide range of  $\xi$  value) of the polarization PAs inside groups is observed for the three samples ( $All(z)$ ,  $QSO(z)$  and  $QSO(z > 1)$ ) although the minima occur at different typical angular separations. Indeed, for the S test, the sample  $All(z)$  shows its minimum SL at 0.3 % for  $\xi \approx 23^\circ$  and  $QSO(z)$  shows a small dip for the range of  $\xi \approx 8^\circ - 26^\circ$  with a minimum  $SL = 1.2\%$  for  $\xi = 18^\circ$ . The high-redshift part of the QSO sub-sample ( $QSO(z > 1)$ ) exhibits values of the SL below 1% for smaller angular separation ( $\xi \leq 10^\circ$ ). These features are confirmed by the Z test as seen from Fig. 3.4 (*bottom*). For this test, the minimum SL value of the sample  $QSO(z)$  is found to be as low as 0.3 % for  $\xi \approx 23^\circ$  and the sample  $QSO(z > 1)$  shows SL below 1% for  $\xi \leq 10^\circ$  with an additional dip around  $\xi = 34^\circ$ .

### Full samples with different object types

Analysing samples with redshift measurements in two dimensions, we have found significant correlations ( $SL < 5\%$  with minima  $< 1\%$ ). It is therefore interesting to also perform the 2-dimensional analysis on the other samples of Table 3.1, i.e. on the samples that are not

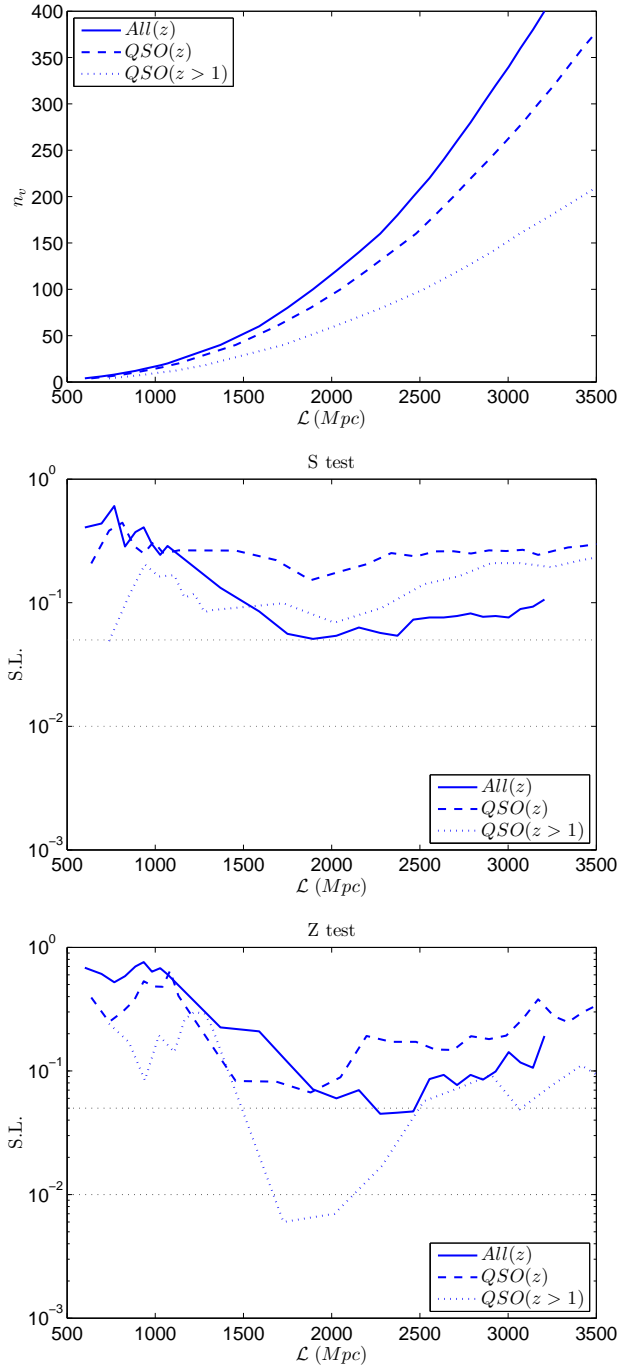


Figure 3.3: 3D analysis of the samples with redshift measurements. (*top*): Relation between the parameter  $n_v$  and the typical comoving separation  $\mathcal{L}$  in Mpc for the samples  $All(z)$ ,  $QSO(z)$  and  $QSO(z > 1)$ . (*middle and bottom*): Significance level obtained with the S and Z tests (resp.) as a function of the typical comoving distance  $\mathcal{L}$  for the three samples. The 5% and 1% SL are indicated with dotted-horizontal lines.

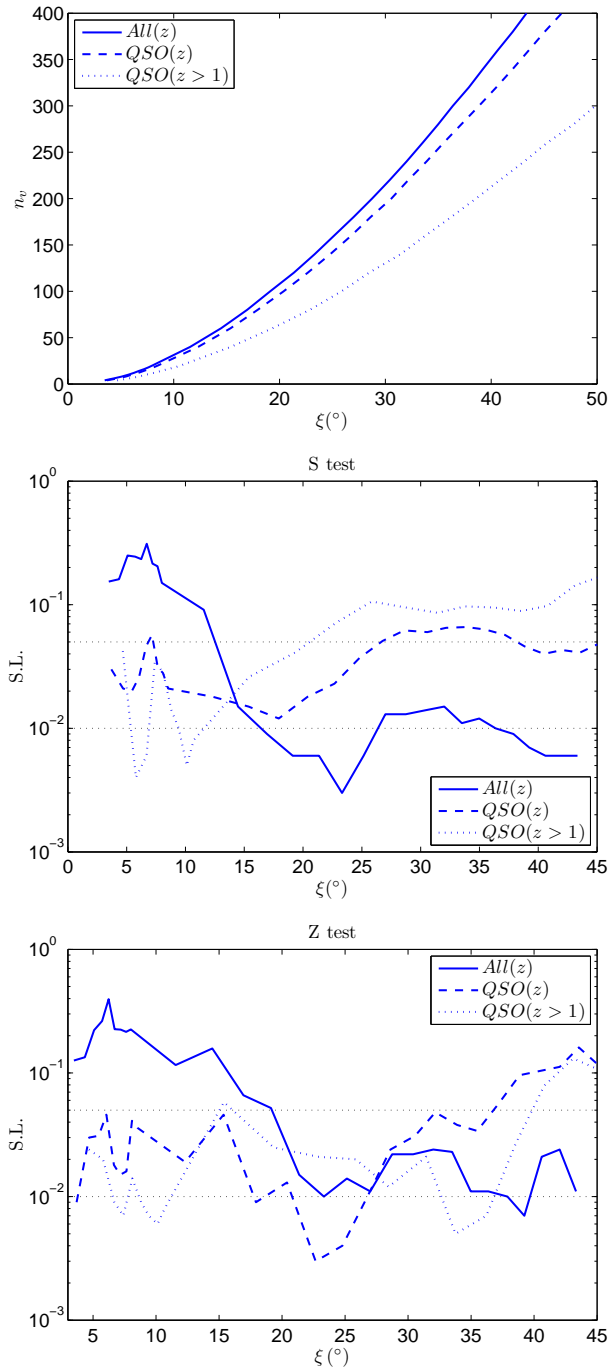


Figure 3.4: 2D analysis of the samples with redshift measurements. (*top*): Relation between the parameter  $n_v$  and the typical angular separation  $\xi$  in degree for the samples  $All(z)$ ,  $QSO(z)$  and  $QSO(z > 1)$ . (*middle and bottom*): Significance level obtained with the S and Z tests (resp.) as a function of the typical angular separation  $\xi$  for the three samples. The 5% and 1% SL are indicated with dotted-horizontal lines.

restricted by the availability of the redshifts of the sources. We thus consider the sample of 4155 sources as well as its four sub-samples with different object types. We show in Fig. 3.5 (*top*) the relations between  $n_v$  and  $\xi$  for these five samples. The results of the S and Z tests are shown in Fig. 3.5 (*middle* and *bottom*, respectively).

For small values of  $n_v$  (from 6 to 10), we found indications of alignments in the three samples *All*, *RS* and *QSO* as the S and Z tests return SL values at the percent level (1.1% and 1.2% for the sample *All*). The indications of alignments in the sample *All* are reminiscent of the correlations highlighted by Tiwari & Jain (2013) at the scale of  $\sim 150 \text{ Mpc}^5$ . The reasons why we found correlations with lower significance are likely that we consider a different sample<sup>6</sup>. We also thought (in Pelgrims & Hutsemékers 2015) that the use of a different definition of the  $S_D$  statistics could cause these differences in SL. However, we have seen in Section 1.1.1 that the two definitions are equivalent.

For large values of  $n_v$ , alignments are detected with SL below 5% over a wide range of  $\xi$  only for the sample *QSO*. The SL of the S test applied to *QSO* exhibits a dip for  $n_v$  between 40 and 140, reaching the value of 0.7% for  $n_v = 60$  and 80. The range of typical angular separations involved in these correlations is  $\xi \approx 12^\circ - 24^\circ$ , with stronger correlations for the range  $14.5^\circ - 17.5^\circ$ . The Z test exhibits a large dip for the range  $n_v = 40 - 200$  with the minimum SL of 0.12% for  $n_v = 140$ , implying correlations at  $\xi \approx 24^\circ$ . Those correlations of polarization PAs involve QSOs separated by large distances on the celestial sphere and confirm the detection made in the sample *QSO(z)* (with redshift measurements) in the previous sub-section.

For such angular scales, the distributions of the polarization PAs of the other samples (*All*, *RS*, *G* and *VO*) are in good agreement with the hypothesis of uniformity. Let us emphasize that these large-scale correlations are not observed for the category of radio sources (*RS*), even though the sample size is comparable to that of *QSO* (see Table 3.1).

### 3.2.3 Intermediate outcomes

So far in the chapter, we have studied the distribution of the polarization PAs of different samples drawn from the JVAS/CLASS 8.4-GHz surveys. We have found significant alignments in some of these samples; first, in one of the regions where the optical polarization vectors were found to be aligned and second, in the QSO all-sky survey.

Regarding the A3 region, a few reasons might lead to the differences between our findings and the conclusions of Joshi et al. (2007). As already mentioned, when these authors analysed the so-called A1 and A3 regions, they did not constrain their sample with regard to the redshift, which is an important characteristic of the optical polarization alignments. They applied their “Nearest Neighbour Test” to the full sample restricted to the sky window of the A3 region, i.e. introducing cuts in right ascension and declination only (see Section 3.3 and 5

<sup>5</sup>See the footnote 1 of this chapter.

<sup>6</sup>When we built the data set from the JVAS/CLASS 8.4-GHz catalogue, we removed duplicate measurements while Tiwari & Jain (2013) did not (Jain 2015 (private communication) and Tiwari & Jain 2015).

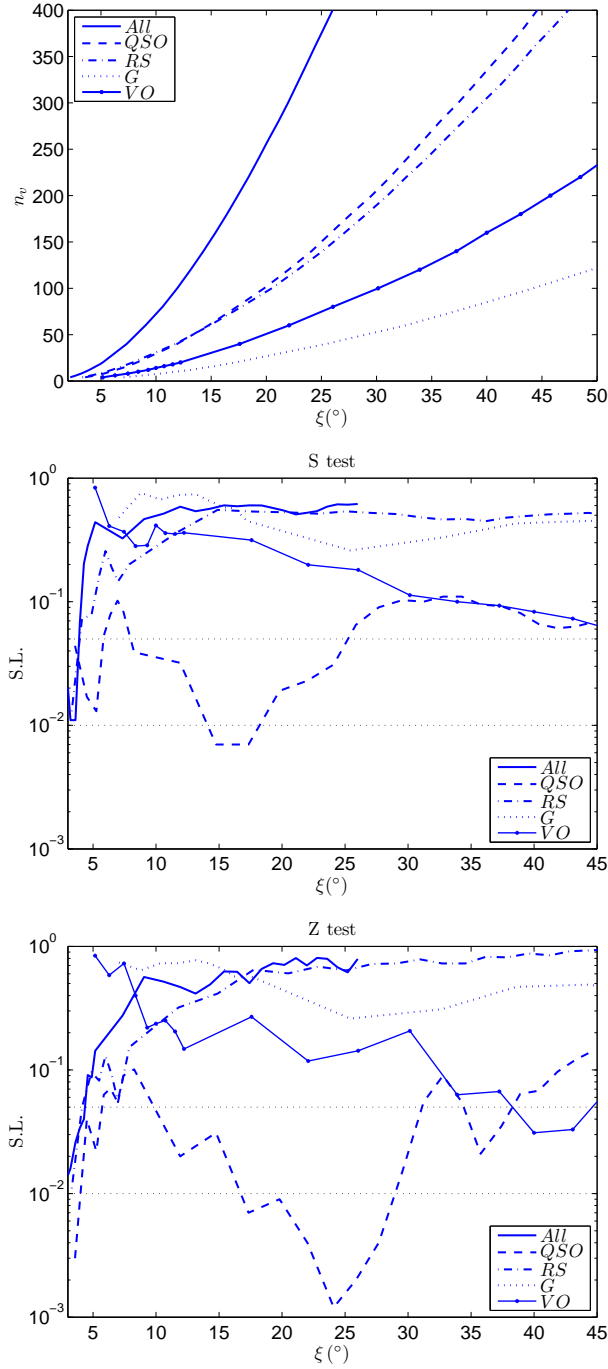


Figure 3.5: 2D analysis of the full samples. (*top*): Relation between the parameter  $n_v$  and the typical angular separation  $\xi$  for the samples *All*, *QSO*, *RS*, *G* and *VO* of Table 3.1. (*middle and bottom*): Significance level obtained with the S and Z tests (resp.) as a function of the typical angular separation  $\xi$  for the five samples. Note that the SL value of the sample *QSO* for  $\xi \approx 24^\circ$  ( $n_v = 140$ ) has been computed with  $10^4$  random simulations.

of Joshi et al. 2007). The first possible cause of divergent results is a redshift dependence of the alignments at radio wavelengths as at optical wavelengths, so that taking all the sources in the window regardless of their redshift blurs the alignment. Alternatively, the comparison of the last two columns of Table 3.2 suggests that alignments are more pronounced for QSOs compared to the other types of objects.

In order to test these two scenarios, we performed an analysis of the samples obtained by imposing the A3 window cut on the different samples of Table 3.1. Results of the Hawley–Peebles test and the PC test of are shown in Table 3.3. Correlations between polarization PAs are observed when we consider the A3 window cut of the samples  $QSO$ ,  $QSO(z)$  and  $All(z)$ , but no deviation from uniformity is detected for the A3 window cut of  $All$ , in agreement with the result of Joshi et al. (2007). Comparison of the last two columns of Table 3.3 teaches us that adding the other species to the  $QSO$  sample completely blurs the alignments. This simple observation argues for the scenario in which the species selection is at the origin of the detection of the correlations. This scenario is reinforced when we consider the A3 window cut of the sample  $RS$ . For this sub-sample of 138 objects, we found that the distribution of the polarization PAs is in agreement with the hypothesis of uniformity. Comparison of Tables 3.2 and 3.3 does not allow us to conclude on a possible redshift dependence of the polarization alignments. This is partially due to the lack of redshift information for non-QSO species.

	A3 window cut on			
	$QSO(z)$	$All(z)$	$QSO$	$All$
$n$	100	115	114	385
$P_{HP}$ (%)	0.36	1.27	1.19	29.6
$\bar{\psi}$ (°)	68	72	68	—
$p_{\min}$ (%)	$7.0 \cdot 10^{-4}$	$1.9 \cdot 10^{-3}$	$5.9 \cdot 10^{-3}$	0.14
$\eta$ (°)	52	52	52	68
$p^\sigma$ (%) [ $n_{sim}$ ]	0.02 [ $5 \cdot 10^4$ ]	0.01 [ $10^4$ ]	$5.4 \cdot 10^{-2}$ [ $5 \cdot 10^4$ ]	1.5 [ $10^3$ ]
$\bar{\psi}_{PC}$ (°)	69	70	68	59

Table 3.3: Same as Table 3.2 but for the sub-samples obtained by application of the A3 window on the samples of 1325 QSOs with redshift ( $QSO(z)$ ), 1531 sources with redshift ( $All(z)$ ), 1450 QSOs regardless of the redshift information ( $QSO$ ), and 4155 flat-spectrum radio sources ( $All$ ).

In the full sample we highlighted alignments involving sources separated by typical angular scales of about  $20^\circ$ . For the samples with redshift measurements, the large-scale correlations are observed to be more significant in the 2-dimensional analysis than in the 3-dimensional one. Considering samples that are not limited by the redshift availability, we also pinpointed that the large-scale correlations mainly concern the category of QSOs as was already suggested during the study of the A3 window in Section 3.2.1.

As a conclusion of the analysis of the all-sky (sub-)samples, we find that the polarization PAs of the JVAS/CLASS 8.4-GHz surveys show correlations in groups of QSOs with an angular radius of about  $20^\circ$ . The significance level at which these correlations can be attributed to statistical fluctuations in the sample of QSO is found to be as low as  $\sim 0.1\%$  for  $\xi \approx 24^\circ$  with the Z test.

3D	S			Z		
	min(SL) (%)	$\mathcal{L}$ (Gpc)	$n_v$	min(SL) (%)	$\mathcal{L}$ (Gpc)	$n_v$
<i>All</i> ( $z$ )	—	—	—	—	—	—
<i>QSO</i> ( $z$ )	—	—	—	—	—	—
<i>QSO</i> ( $z > 1$ )	—	—	—	0.6	$\sim 1.7$	40
2D	min(SL) (%)	$\xi$ ( $^\circ$ )	$n_v$	min(SL) (%)	$\xi$ ( $^\circ$ )	$n_v$
<i>All</i> ( $z$ )	0.3	$\sim 23$	140	1.0	$\sim 23$	140
<i>QSO</i> ( $z$ )	1.2	$\sim 18$	80	0.3	$\sim 23$	120
<i>QSO</i> ( $z > 1$ )	0.5	$\sim 10$	18	0.6 / 0.5	10 / 34	18 / 160
<i>All</i>	1.1	3 – 4	8 – 10	1.2	$\sim 3$	6 – 8
<i>QSO</i>	0.7	14.5 – 17.5	60 – 80	0.12 *	$\sim 24$	140
<i>RS</i>	1.3	$\sim 3$	4	1.1	$\sim 3$	4
<i>G</i>	—	—	—	—	—	—
<i>VO</i>	—	—	—	3.0	$\sim 40$	160

Table 3.4: Summary of the application of the S and Z statistical tests to all samples of Table 3.1. For each test, we report the value of the minimum SL with the corresponding  $n_v$  parameter and its attached typical scale ( $\mathcal{L}$  or  $\xi$  for the 3- or 2-dimensional analysis, resp.). We only show results when the SL of the sample is found to be below the threshold of 5% for a wide range of  $n_v$ . All SL have been evaluated with 1000 Monte Carlo simulations except the smallest one (marked by an asterisk) for which we had to use 10 000 simulations.

### 3.3 Identification of regions of aligned polarizations

For the correlations highlighted in the previous section, it would be of interest to figure out if the alignments detected at typical scales of  $\xi \approx 15^\circ - 25^\circ$  are due to a global trend across the whole sky coverage of the survey or if they are prominent in some regions of the sky, as seems to be the case at optical wavelengths.

To this end, we proceed to the identification of the groups of sources with distributions of polarization PAs that show significant departure from uniformity. The fact that these groups are clustered in space or not tells us whether the correlations of polarization orientations are due to well localized objects or to a general trend. This identification can, inter alia, be achieved with the help of the S and Z tests. For clarity, we give the details for the S test. Also, note that we limit our search to the 2-dimensional analysis of the sample *QSO* since

it revealed the most convincing evidence for departure from uniformity with a confidence level higher than 99% for the range of  $\xi \approx 14.5^\circ - 17.5^\circ$ .

In Section 3.2.2, local statistics  $S_i$  were computed for each nearest-neighbour group and these statistics have been computed for each simulated data set. We attribute to each central source  $i$  the quantity  $s_i$  which tells us how much the corresponding group of nearest neighbours contributes to the global statistics  $S_D$ . This quantity is defined as  $s_i = (\langle S_i \rangle - S_i^*) / 2\sigma_i$ , where  $S_i^*$  is the statistics obtained for the observed data set (see Eqs. 1.1 and 1.2) and where  $\langle S_i \rangle$  and  $\sigma_i$  are the mean and the standard deviation of this statistics evaluated over the whole set of simulations assuming that the local statistics are normally distributed. The larger the value of  $s_i$ , the more the group contributes to  $S_D$ . If the local statistics were normally distributed, then  $s_i$  would be the number of sigma with which the observations differ from randomness, divided by 2. However, the local statistics are not normally distributed and  $s_i$  is just an empiric measure of the significance of the local alignment. A group of nearest-neighbour objects is considered as contributing significantly to  $S_D$  if  $s_i \geq s_c$ , for an arbitrary threshold  $s_c$ .

Of course we shall search for the identification of the most significant groups, i.e. consider the  $s_i$  quantities computed with the parameter  $n_v$  chosen such that  $S_D$  is the smallest (see Table 3.4). To visualize the sky location of the most significant groups we produce maps which highlight their central sources. Note that these maps do not critically depend on the choice of  $n_v$ . These maps are equal-area Schmidt projection (e.g., Fisher et al. 1993) of the northern hemisphere (in equatorial coordinates). This choice is suitable for the considered data set as it covers only positive declinations. We also plot (in grey bold lines) the limits of the A1 and A3 windows defined in Section 3.2.1. Let us insist on the fact that only the northern part of these limits are shown: the A1 and A3 windows defined from the analysis at optical wavelengths extend to the South equatorial hemisphere which is not displayed here.

The identification map corresponding to the S test (in 2D) for the sample *QSO* with the parameters  $n_v = 80$  and  $s_c = 2.5$  is shown in Fig. 3.6. As one can see, the highlighted central sources cluster in three or four groups along with other more sparse and/or isolated locations. When pushing  $s_c$  up to 3 (darker points), only the cluster with right ascension  $\alpha \sim 206^\circ$  and declination  $\delta \sim 38^\circ$  remains. Following this analysis, it is likely that the significant departure from uniformity in this sample is due to polarization alignments in a few groups of QSOs. It is intriguing that two of them are found in the A1 and A3 windows. In order to put the latter identification of aligned regions on stronger grounds, we may use other tests. The Z test also reveals significant non-uniformity. For the *QSO* sample and the parameter value  $n_v = 140$ , it leads to the map shown in Fig. 3.7 which is in relatively good agreement with Fig. 3.6 although it shows more scattered clusters.

Also, we find relevant to proceed to a complementary identification using the PC test. As this test does not depend explicitly on the number of nearest neighbours (while it is encapsulated within the statistics), local groups can be defined by a physical angular scale,



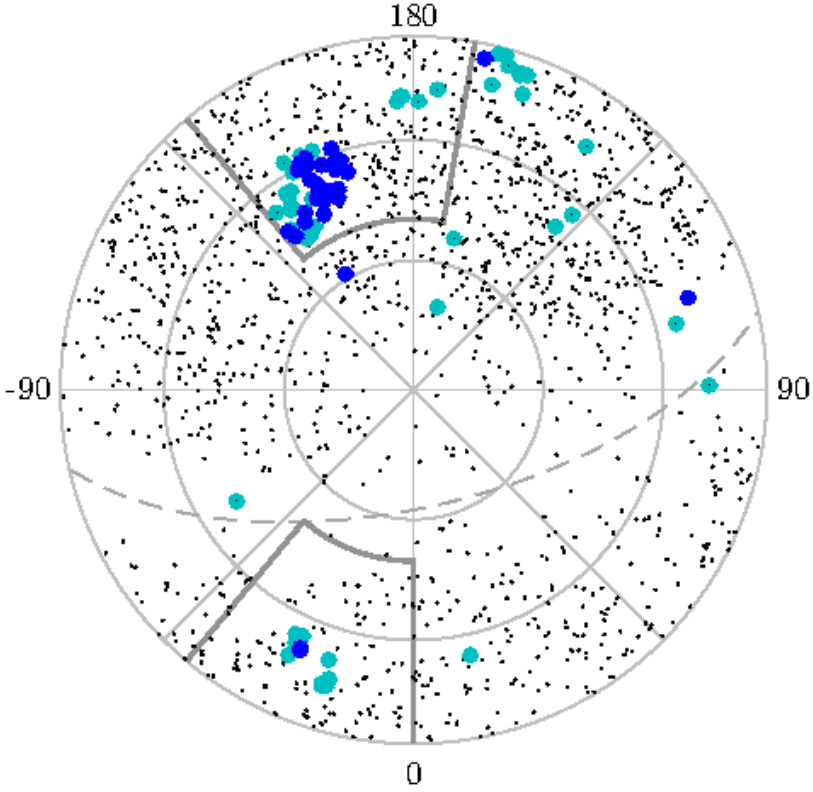


Figure 3.6: Identification map for the sample *QSO* using the S test in 2D. The parameter is fixed to  $n_v = 80$  (see Fig. 3.5 (*middle*)) and we adopt two threshold values:  $s_c = 2.5$  (lighter points) and  $s_c = 3.0$  (darker points), respectively cyan and light blue. Identification maps are equal area Schmidt projection of equatorial coordinates. Only the equatorial north hemisphere is displayed with the north pole at the centre of the map. Grey circles are parallels of declinations  $0^\circ$ ,  $30^\circ$  and  $60^\circ$  and grey diagonals are meridians of right ascensions being multiple of  $45^\circ$ . The curved dashed line is the Galactic equator, the North and the South Galactic caps being respectively above and below the line. Grey bold lines are northern boundaries of the A1 and A3 regions of optical polarization alignments (see text). Small black dots are the locations of the 1450 sources of the sample. Highlighted sources are objects for which corresponding neighbours show a polarization PA distribution that is unlikely due to chance.

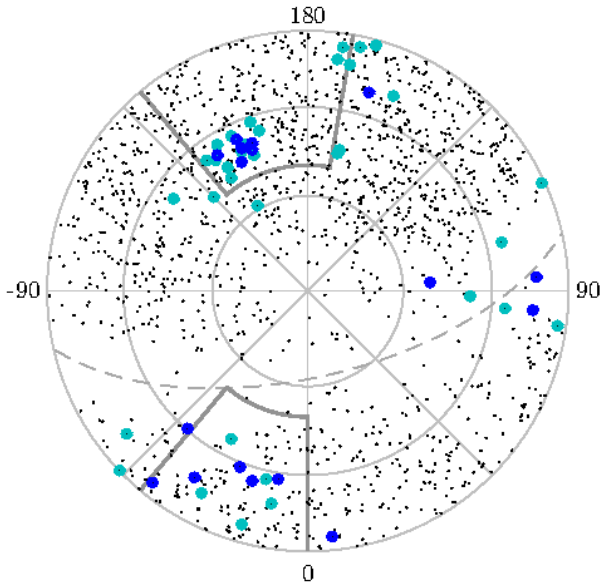


Figure 3.7: Identification map for the sample *QSO* using the Z test in 2D. The parameter is fixed to  $n_v = 140$  (see Fig. 3.5 (bottom)) and we adopt two threshold values:  $s_c = 1.65$  (lighter points) and  $s_c = 1.75$  (darker points), respectively cyan and light blue. Please note that the thresholds  $s_c$  for the S and Z tests do not refer to the same quantities and have thus different values (compare Eqs. 1.6 and 1.10 for instance).

denoted  $\Omega$ . In order to carry out an identification as close as possible to those produced with the S and the Z tests, we found necessary to split each sample in its two Galactic hemispheres to determine the physical scale at which local groups have to be defined. Indeed, the density of the data points in the North Galactic Cap and the South Galactic Cap are different. In the sample *QSO*, the typical angular separation corresponding to  $n_v = 80$  is  $\xi \approx 17^\circ$  and corresponding to  $n_v = 140$  is  $\xi \approx 24^\circ$  (cf. Fig. 3.5 (Top)). However, by splitting the sample in its northern and southern Galactic parts, we obtain  $\xi_N \approx 16^\circ$  and  $\xi_S \approx 23^\circ$  for  $n_v = 80$  and  $\xi_N \approx 21^\circ$  and  $\xi_S \approx 33^\circ$  for  $n_v = 140$ , respectively. Given these values, we decided to define local groups in 2 dimensions with angular scales  $\Omega_N = 20^\circ$  for the North and  $\Omega_S = 30^\circ$  for the South.

As we search for the characterization of the polarization PA distribution of each group taken as a whole, we shall not investigate values of  $\eta$  (the free parameter of the method) below the angular separation of the group, i.e. below the imposed angular scales. We arbitrarily chose  $\eta = 40^\circ$  and  $\eta = 50^\circ$  for the North and the South, respectively. The identification map computed with these parameters is shown in Fig. 3.8. We checked the robustness of the map with other pairs of values such as  $(\Omega_N, \Omega_S) = (15^\circ, 25^\circ)$  and  $(25^\circ, 35^\circ)$ . We also checked the stability of our results using other values of  $\eta$ . Note that we did not search for the optimal value of  $\eta$ , i.e. the one which would give the lowest probabilities, as the method undergoes edge effects. We rather spanned the range of  $20^\circ$  to  $60^\circ$  with step of  $5^\circ$  and found consistent maps.

Although a close examination shows discrepancies in the precise locations of central sources of neighbouring groups, a comparison of the maps presented in Figs. 3.6, 3.7 and 3.8 shows a relatively good agreement, especially for the cluster at  $(\alpha, \delta) \sim (206^\circ, 38^\circ)$ .

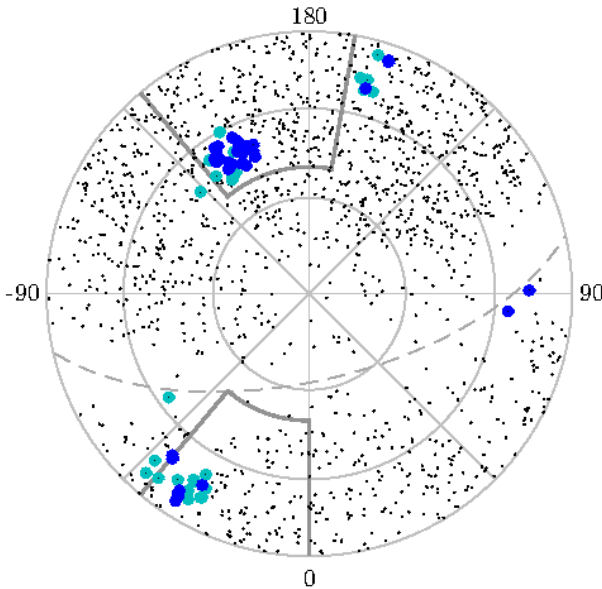


Figure 3.8: Identification map for the sample *QSO* with the PC test. Parameters are fixed as  $\Omega = 20^\circ$  and  $\eta = 40^\circ$  for the North Galactic Cap and  $\Omega = 30^\circ$  and  $\eta = 50^\circ$  for the South Galactic Cap. Highlighted sources correspond to groups showing  $p_{\min} \leq 10^{-3}$  (lighter points) and  $p_{\min} \leq 3 \cdot 10^{-4}$  (darker points), respectively cyan and light blue.

In order to define more precisely the limits of regions of polarization alignment, we proceed as follows. To each central source corresponds a group of nearest objects (defined via the parameter  $n_v$  or  $\Omega$ ). A highlighted central source is said to form a cluster along with (an)other highlighted source(s) if it belongs to the group of nearest objects of the latter. A central source is discarded from a cluster if it is not in the neighbourhood of a sufficient percentage of central sources forming this cluster (e.g.  $\sim 60\%$ ). Reproducing this test for all highlighted objects, we end up with identification of independent clusters. We finally add to the cluster the nearest neighbouring objects of each central sources, paying attention to duplication. Although this procedure is rudimentary, it is sufficient for our goal. We thus end up with three regions for each of the three tests. We decide to define our final regions as the intersection of the regions from the different tests. We report the final regions of alignments in Table 3.5 which also gives some of their characteristics and the result of the application of the Hawley–Peebles test on their polarization PA distributions.

As a result, we identified three well-defined regions of the sky in which QSOs show coherently oriented polarization vectors. Two of these regions are located in the North Galactic hemisphere of the sky and one towards the South. Considering the southern cap, it is worth remarking that more than 85% of the sources of the sub-sample identified here belong to the A3 window defined from the region of optical alignment discovered by Hutsemékers et al. (1998; 2001; 2005). To the North, the identified regions are located at the edges of the A1 window of optical alignment, one outside at low declination and the other inside at high declination. We call them RN1 and RN2, respectively. It is again worth mentioning that more than 70% of the sources of the RN2 sub-sample identified here belong to the A1 window. It is remarkable that our region RN2 coincides with the main aligned cluster resulting from the

independent analysis of Shurtleff (2014). Consistently with our previous results, we report a stronger alignment than he did as we only consider the species of QSO.

In order to visualize the alignment patterns, we show in Fig. 3.9 the equatorial-coordinate maps of the normalized polarization vectors of the identified regions along with their corresponding polarization PA histogram. Some structures can be spotted out by eye. This is better seen in the region RN1 (see Fig. 3.9 (Top)). The statistical tests used throughout this analysis do not allow us to search and characterized better such structures. This task is far beyond the scope of this chapter and would request dedicated algorithms to compute the likelihood of structures of aligned polarization vectors in a random sample.

	$N$	$(\alpha, \delta)_{\text{CM}} (^{\circ})$	$\bar{\xi} (^{\circ})$	$\xi_{\text{max}} (^{\circ})$	$P_{\text{HP}} (\%)$	$\bar{\psi} (^{\circ})$
RN1	108	(163, 12)	12	21	0.45	131
RN2	191	(206, 38)	14	25	1.17	42
RS1	116	(340, 18)	15	25.2	1.45	57

Table 3.5: Identified regions from the 2-dimensional analysis of the sample *QSO* with the S, Z and PC tests. Regions are intersections of those given by each test (see text). The two first lines are for the regions located in the North Galactic cap and the third is for the region of the South part. They are named RN1, RN2 and RS1, respectively.  $N$  is the number of members belonging to the region,  $(\alpha, \delta)_{\text{CM}}$  refers to the position of the normalized vectorial sum of the sky location of the sources of the region,  $\bar{\xi}$  and  $\xi_{\text{max}}$  are the mean and the maximum value of the angular separations of sources to  $(\alpha, \delta)_{\text{CM}}$ .  $P_{\text{HP}}$  and  $\bar{\psi}$  are the results of the Hawley–Peebles test.

## 3.4 Interpreting the results

So far we have found that the polarization vectors of QSOs which are in groups that have angular radii of about  $20^{\circ}$  have correlated orientations. We showed that these groups cluster in three independent regions of the sky and that to each of these corresponds a different preferred polarization PA.

### 3.4.1 Are the data contaminated?

The preferred angles for the two northern regions are found to have values close to  $45^{\circ}$  and  $135^{\circ}$ . These values, are very particular (see Battye, Browne & Jackson 2008) and lead us to consider the possibility that the correlations we found are due to biases in the data set; despite our careful selection of polarized sources in Section 3.1, following the prescriptions of Jackson et al. (2007). This hypothesis is a priori difficult to reconcile with the local character of the alignment features but could potentially explain that they are better detected with

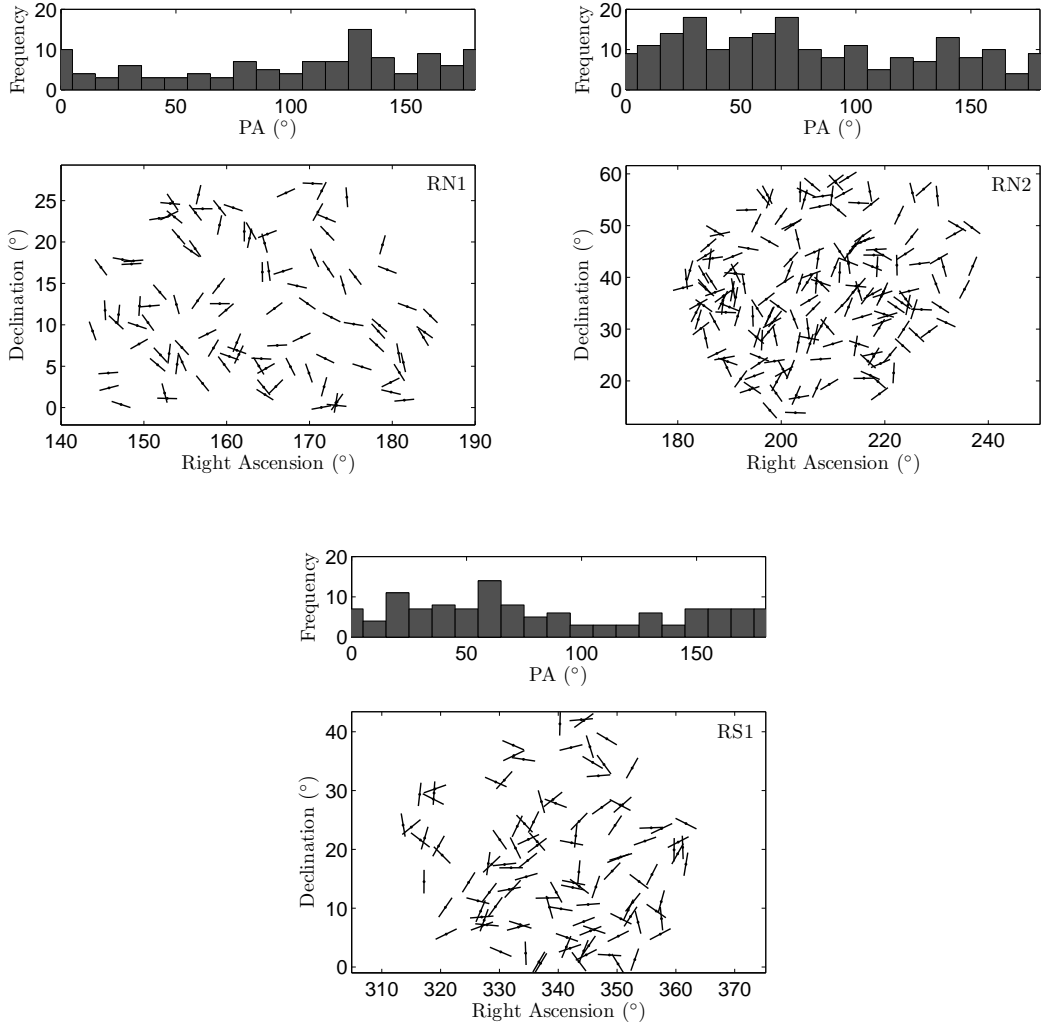


Figure 3.9: Maps of polarization vectors in the identified regions along with their corresponding polarization PA histograms. Polarization vectors are normalized to the same length in each map. (*top-left* and *top-right*): the two regions in the North Galactic hemisphere at low and high (equatorial) declination, respectively. (*bottom*): the region identified in the South Galactic hemisphere. Properties of these regions are given in Table 3.5.

the 2-dimensional analysis than with the 3-dimensional one. In this sense, and contrarily to what Jackson et al. (2007) and Joshi et al. (2007) claimed, we also find evidence for a global non-uniformity inside the polarization data set. Using the Hawley–Peebles test, the probability that the distribution of the 4155 objects is uniform is found to be  $P_{\text{HP}} = 2.7\%$  (with  $\bar{\psi} \sim 51^\circ$ ). This non-uniformity of the overall polarization distribution of the sample *All* argues for the hypothesis of a biased data set. However, consistently with our previous results, this non-uniformity is found to come from the sub-category of QSO as we find  $P_{\text{HP}} = 1.1\%$  (with  $\bar{\psi} \sim 57^\circ$ ) for this sample and that removing the QSOs from the sample *All* leads to  $P_{\text{HP}} = 44.5\%$ <sup>7</sup>. This result together with the previous evidence for alignment of QSOs and not for the other species is awkward to reconcile with an observational bias, as there is no reason for a contamination of the polarization data for the species of QSO and not for the others, as we shall see.

Comparing the properties of the samples *QSO* and *RS* (which have a comparable number of objects), we note some differences. As illustrated by the Fig. 3.10, their polarization characteristics at radio wavelengths do not follow the same parent distribution. However, we do not find obvious reasons why the QSOs would be more affected by observational biases than the sample *RS* as the QSO sample shows higher total and polarized flux.

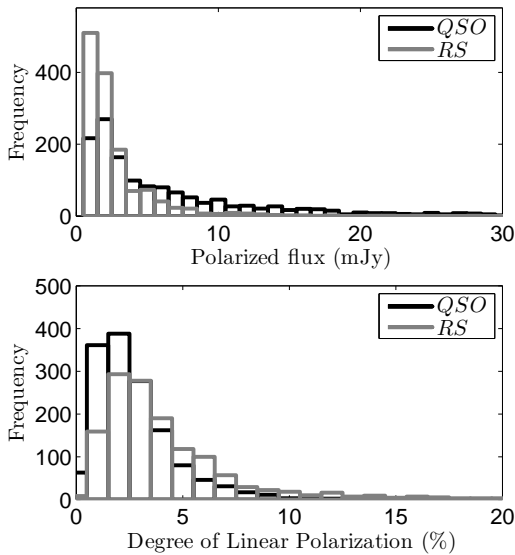


Figure 3.10: Polarized flux (*top*) and degree of linear polarization (*bottom*) of the samples *QSO* and *RS*. A two-sample Kolmogorov–Smirnov test reveals that the polarized flux, as well as the degree of linear polarization, of the two samples have a probability much below 1% to be drawn from the same underlying parent distribution.

The distributions on the sky of the two samples are also different as shown in Fig. 3.11. While the sample *QSO* is almost homogeneously distributed over the sky, the sample *RS* is far from being so.

In order to test the possibility that it is the difference of the distributions on the sky that is responsible for the detection of alignments for *QSO* and not for *RS*, we test the uniformity

<sup>7</sup>The polarization PA distribution of the sample *RS* is also in good agreement with uniformity ( $P_{\text{HP}} = 79.1\%$ ).

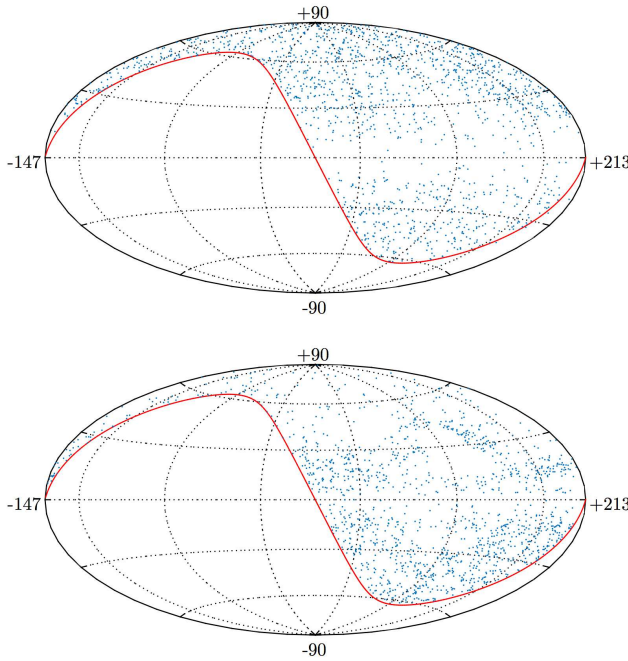


Figure 3.11: Hammer-Aitoff projection of the positions in Galactic coordinates of the sub-samples *QSO* (top) and *RS* (bottom) that contain 1450 and 1379 FSRs respectively. The red line corresponds to the equator of the equatorial coordinates. The map is centred at Galactic longitude  $l_{\text{gal}} = 33^\circ$  for comparison of the sky distribution of the optical sample in Fig. 2 and of the entire sample of the 4155 FSRs in Fig. 3.1. The difference of the sky coverages of the sub-sample *QSO* and *RS* can be spotted by eye.

of the polarization PA of the RS's belonging to the regions of alignments of Table 3.5. The overlap is very poor for the regions in the North Galactic hemisphere: only 32 RS's are found in each of the RN1 and RN2 regions. To the South, however, there are 165 RS's in the RS1 region. The Hawley-Peebles test does not reveal departure from uniformity, neither taking RS's alone or mixing them with the QSOs of this region<sup>8</sup>. Therefore, while the bad overlap between the *QSO* and *RS* samples in the northern regions could explain the difference in the alignment detection, this is not the case to the South. We thus conclude that the difference of the distributions on the sky is unlikely responsible for this difference.

Similarly to an instrumental bias, contamination by foreground polarization would affect more strongly the sample of RS's than that of QSOs as the polarized flux is globally smaller for *RS* (see Fig. 3.10 (top)). This is again in contradiction with what is observed. The contamination by foreground polarization is thus unlikely to be responsible for the observed correlations of the polarization PAs of QSOs.

<sup>8</sup>This was expected from the analysis of the A3 window (see Section 3.2.3).

### 3.4.2 Are the polarization alignments real?

As polarization is usually correlated to the morphological axis of the object (e.g., Saikia & Salter 1988; Lister 2001; Pollack, Taylor & Zavala 2003; Smith et al. 2004; Marin 2014), there might be real differences between the classes of QSO and RS. Indeed, the core dominated FSRs are predominantly quasars or BL Lac objects in which the jet is oriented close to the line of sight (see Jackson et al. 2007). The majority of the sources belonging to the sample *RS* is thus expected to be BL Lac objects which are thought to be viewed at very small angles to the line of sight. Consequently, they are expected to show rapid variations ( $< 2$  years) of their polarization PA and to be more strongly polarized than quasars, which is what we observe in Fig. 3.10 (Bottom). Also, for this class of objects, no net correlation between the jet orientation and the polarization PA has been reported (e.g., Pollack et al. 2003 and references therein). These observational facts could explain the absence of alignment signatures for the sample of RS's within the hypothesis that polarization alignments reflect morphological-axis alignments of the sources, as supported by the recent discovery at optical wavelengths of such correlation for one of the most largest known quasar group at  $z \sim 1.3$  (see Chapter 4). The latter hypothesis is also reinforced by the discovery of large-scale alignments of the jet position angles of active galactic nuclei in the ELAIS N1 field by Jagannathan & Taylor (2014) and Jagannathan (2014). The fact that radio and optical alignments are found in the same parts of the sky also supports a real effect. In this framework, one would have to compare the alignment patterns observed at optical wavelengths with these at radio wavelengths. However, given the bad overlap between the sky coverage of the radio and optical catalogues, a detailed comparison is not straightforward. To illustrate the weak overlaps between the radio and optical samples, we show in Fig. 3.12 equatorial maps of the sources from both samples that are found in the neighbourhood of the regions of alignments. Sources that we defined as being part of the RN1, RN2 and RS1 regions are highlighted in light red and sources belonging to the A1 and A3 regions of Hutsemékers et al. (2005) in light green. Again, the alignment regions in the optical that we defined in Chapter 2 are smaller than A1 and A3, the overlaps being even worth. We also show the polarization vector orientations of sources that belong to regions of alignments.

## 3.5 Concluding remarks

We tested the hypothesis that the polarization position angles are randomly distributed among the FSRs contained in the JVAS/CLASS 8.4-GHz surveys presented in Jackson et al. (2007). We performed the analysis in two and three dimensions, accounting for the distribution of the sources on the sky (2D) and additionally for their line-of-sight comoving distances (3D). The polarization orientations of quasars (the *QSO* sample) show low probabilities to be consistent with the hypothesis of randomness. This departure from uniformity is likely to be due to correlations of polarization vectors of QSOs in groups of angular radius of about  $20^\circ$ .



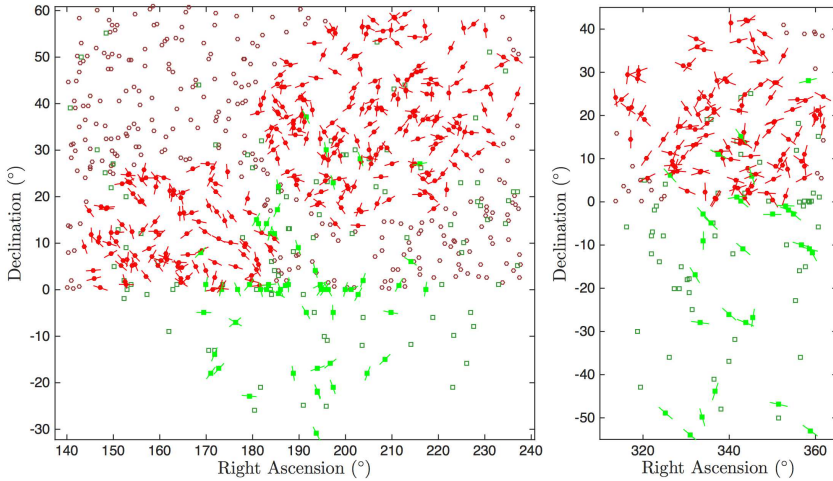


Figure 3.12: Comparison of the optical sample and radio sample in the sky neighbourhood of the align regions. (*left*) towards the North Galactic Cap and (*right*) toward the South Galactic Cap. For each panel we show all the sources from both samples that have (equatorial) right ascension and declination in the range  $\alpha \in [140^\circ, 238^\circ]$  and  $\delta \in [-31^\circ, 61^\circ]$  for the North and  $\alpha \in [313^\circ, 362^\circ]$  and  $\delta \in [-55^\circ, 43^\circ]$  for the South. Sources from the sub-sample *QSO* are displayed by brown circles and those from the optical sample by dark green squares. Sources contained in aligned regions (accounting for redshift limits at optical wavelengths) are highlighted with filled symbols in light colors (red and green, respectively) and their polarization vectors are shown with fixed but arbitrary length.

A basic identification procedure has shown that these groups cluster in three distinct regions of the sky. Two of them fall in the A1 and A3 windows of the sky where optical polarization alignments were found in Hutsemékers et al. (1998; 2001; 2005). Among sources in the JVAS/CLASS sample, only the sub-sample of QSO exhibits such large-scale correlations. If real, such alignments at radio wavelengths would support the interpretation of alignments at optical wavelengths by spin-axis alignments (Hutsemékers et al. 2014 and Chapter 4). However, our findings prove to be difficult to interpret either as resulting of biases in the data set or as being the signature of a physical effect. Indeed, one can find arguments for and against each scenario. Among them, the fact that the alignments are more pronounced in 2D than in 3D and that the mean PAs are multiple of  $45^\circ$  in some regions would suggest a biased data set whereas the detection of alignments for one class of object but not for the others and the clustering of aligned sources in a few regions of the sky consistent with those found at optical wavelengths might be seen as the signature of a physical effect.

To conclude, we highlighted correlations between the quasar radio-polarization vectors which could demonstrate the presence of the same kind of alignment effect as seen at optical wavelengths, or alternatively, which could demonstrate that the radio polarization catalogue

is affected by observational biases and thus cannot be used to study the polarization orientations of flat-spectrum radio sources. Therefore, the claim by Joshi et al. (2007) stating that, at radio wavelengths, there is no alignment signature of polarization vectors on cosmological scales of the type found at optical wavelengths should be taken with caution. The consequences regarding the optical polarization alignments of quasars and the conclusions on possible mechanisms that produce them should be revisited accordingly.

More data are clearly needed to assess either the reality of polarization alignments at radio wavelengths or the presence of residual biases in the JVAS/CLASS 8.4-GHz radio polarization samples. Furthermore, more optical polarization measurements of quasars in the regions of alignments of the radio sample, and vice versa, would help to disentangle the two possibilities and, in the mean time, allow us to perform a careful comparison of the alignments from both spectral bands.

## Chapter 4

# Alignment of quasar polarizations with large-scale structures

The reported alignments of the optical polarizations of quasars involve sources that are located in regions of the comoving space that extend over Gpc scales at redshift  $z \sim 1.0$  (Hutsemékers et al. 1998; 2001; 2005; Jain et al. 2004; Shurtleff 2013; Pelgrims & Cudell 2014). Possible effects modifying the polarization of light along the line of sight, in particular mixing with axion-like particles, have been investigated in detail (e.g., Das et al. 2005; Agarwal et al. 2012). However, because of the absence of comparable circular polarization, these mechanisms have essentially been ruled out (Hutsemékers et al. 2010; Payez et al. 2011).

Since quasar polarization is often related to the geometry of the object, another interpretation would be that quasar morphological axes themselves are aligned. This hypothesis is supported by the detection of quasars polarization alignments at radio wavelengths (Chapter 3) as this implies a mechanism of polarization alignment independent of the wavelength. Note that this is true only if the direction of the polarization vectors at the considered wavelength is correlated to the morphologies of the objects. One has then to search for a mechanism that would align the quasar structural axes over huge distances.

In the framework of the tidal torque theory, the angular momenta of the galaxies and of the massive black holes that they harbour is transferred from the surrounding matter density field during collapse and accretion into proto-galaxies and proto-clusters (e.g., White 1984; Heavens & Peacock 1988; Lee & Pen 2001). If the quasar structural axis orientations themselves are correlated due to such a mechanism of angular momentum transfer, they are then expected to correlate to the shape of the structure they belong to, which can be the filaments or the sheets that form the cosmic web.

In the concordance model of cosmology, the matter density field is not expected to contain superstructures exceeding the homogeneity scale of the Universe. Based on fractal analyses of the matter distribution, this scale is known to be at most of the order of

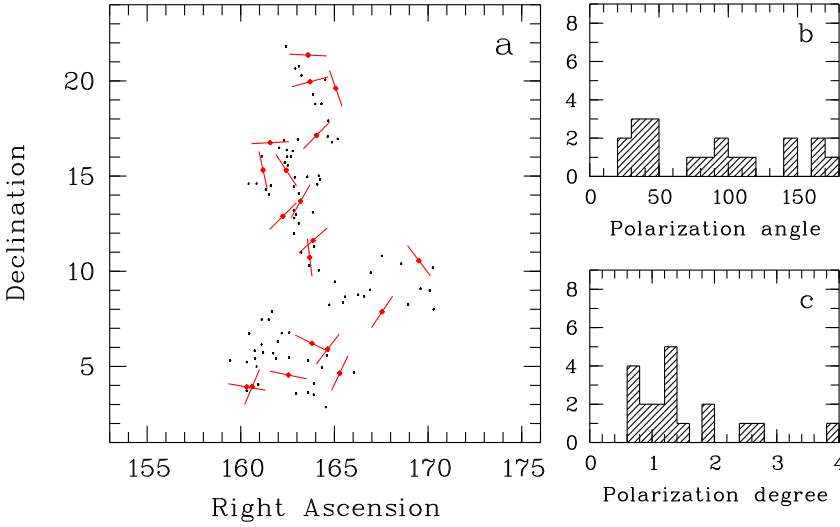


Figure 4.1: The polarization of the 19 quasars with  $p_{\text{lin}} \geq 0.6\%$ . (a) Map of polarization vectors over the large-scale structure; right ascensions and declinations are in degree; the length of the polarization vectors is arbitrary. (b) Distribution of polarization angles (in degree). (c) Distribution of polarization degrees (in %).

$\sim 370$  Mpc (Yadav, Bagla & Khandai 2010). Rationally, the angular momenta of galaxies are thus not expected to be correlated over scales larger than that. As this scale is almost one order of magnitude smaller than the typical scale of the optical polarization alignments, it seems unlikely that the aforementioned hypothesis is responsible for the quasar-structural-axis alignments. However, Clowes et al. (2013) studied the space distribution of quasars in the high-redshift sample from the Sloan Digital Sky Survey Data Release 7 (SDSS DR7) (Schneider et al. 2010) and claimed the discovery of an extreme-scale structure at redshift  $z \sim 1.3$ . This elongated large quasar group (LQG), named the Huge-LQG by the authors, has its largest axis running over more than 1 Gpc. While the physical origin of this structure, which is the largest structure in the Universe following the words of Clowes et al. (2013), and its potential to challenge the cosmological principle is still controversial (Nadathur 2013; Einasto et al. 2014; Park et al. 2015 and Enea Romano, Cornejo & Campusano 2015), this LQG offered for the first time the opportunity to test the hypothesis following which the quasar polarization alignments are correlated to the large-scale structures of the Universe and thus could reflect the alignment of the quasar structural axes over cosmological scales.

To test this hypothesis, we have measured the polarization of quasars belonging to two large quasar groups at redshift  $z \sim 1.3$  described by Clowes et al. (2013). These groups are the U1.27 and the U1.28 called the Huge-LQG and the CCLQG, respectively. It is interesting to note that the Huge-LQG as well as the smaller one located in its cosmic neighbourhood (named the CCLQG after its discovery by Clowes & Campusano 1991) are located on the outskirts of the A1 region (or equivalently the N2+ region) of the quasar-optical-polarization

alignments. Moreover, these LQGs are both located inside the RN1 window of the sky in which we found that the radio-polarization of quasars are aligned (see Section 3.3). Whether these sky locations is coincidental or physically real is still an open question.

Out of the 93 observed quasars, 19 are significantly polarized ( $p_{\text{lin}} \geq 0.6\%$ ). As we shall see in the next sections, we found from this sample that quasar polarization vectors are either parallel or perpendicular to the directions of the large-scale structures to which they belong. Statistical tests indicate that the probability that this effect is compatible with randomly oriented polarization vectors is of the order of 1%. We also found that quasars with polarization preferentially perpendicular to the host structure have large emission line widths while objects with polarization preferentially parallel to the host structure have small emission line widths. Considering that quasar polarization is usually either parallel or perpendicular to the accretion disk axis depending on the inclination with respect to the line of sight, and that broader emission lines originate from quasars seen at higher inclinations, we conclude that quasar spin axes are likely parallel to their host large-scale structures. In the next sections of this chapter, we present the polarization data and their analysis as published in Hutse

## 4.1

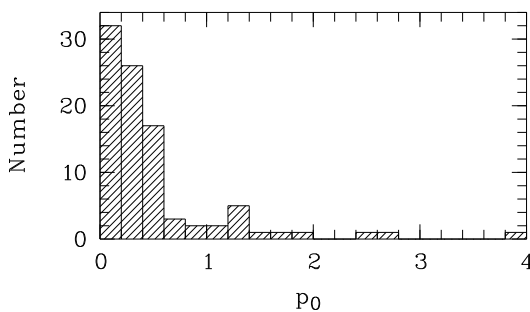


Figure 4.2: The distribution of the debiased polarization degree  $p_0$  (in %) measured for the sample of 93 quasars.

Observations were carried out at the European Southern Observatory<sup>1</sup>, Paranal, on March 22–26, 2014, using the Very Large Telescope equipped with the FORS2 instrument in the standard imaging polarimetry mode IPOL<sup>2</sup>. Linear polarimetry is performed by inserting in the parallel beam a Wollaston prism which splits the incoming light rays into two orthogonally polarized beams separated by  $22''$ . Image overlapping is avoided by inserting a special mask in the focal plane. To measure the normalized Stokes parameters  $q$  and  $u$ , four frames are obtained with the half-wave plate rotated at four position angles,  $0^\circ$ ,  $22.5^\circ$ ,  $45^\circ$  and  $67.5^\circ$ . This procedure allows us to remove most of the instrumental polarization.

<sup>1</sup><http://www.eso.org/public/unitedkingdom/>

<sup>2</sup>FORS User Manual, VLT-MAN-ESO-13100-1543, Issue 92.0

The linear polarization degree  $p_{\text{lin}}$  and the polarization position angle  $\psi$  are derived using  $p_{\text{lin}} = (q^2 + u^2)^{1/2}$  and  $\psi = (1/2) \arctan(u/q)$  so that  $q = p_{\text{lin}} \cos 2\psi$  and  $u = p_{\text{lin}} \sin 2\psi$ . Since orthogonally polarized images of the object are simultaneously recorded, the measured polarization dc

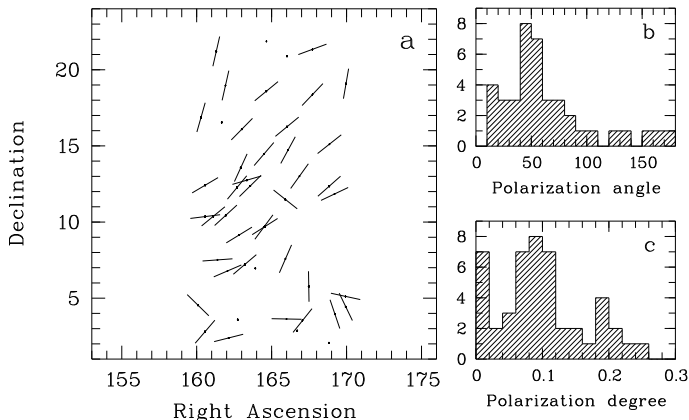


Figure 4.3: The interstellar polarization in the region of the sky corresponding to the quasar large-scale structure under study (data from Berdyugin, Piirola & Teerikorpi 2014). (a) Map of the polarization vectors; right ascensions and declinations are in degrees; the length of the polarization vectors is arbitrary. (b) Distribution of the polarization angles (in degrees). (c) Distribution of the polarization degrees (in %).

All observations were obtained using the FORS2 V<sub>high</sub> filter ( $\lambda_0 = 555$  nm, FWHM = 123 nm). Data reduction and measurements were performed as detailed in Sluse et al. (2005). The instrumental polarization was checked using the unpolarized stars WD0752–676 and WD1615–154 (Fossati et al. 2007) and found to be  $p_{\text{lin}} = 0.05 \pm 0.06\%$ , which is consistent with zero<sup>3</sup>. We did not use field stars to estimate the instrumental polarization because of spurious off-axis polarization in FORS1/2 (Patat & Romaniello 2006). To fix the zero-point of the polarization position angle, polarized standard stars have been observed: NGC 2024–1, Ve 6–23, CD–28° 13479, HD 316232, BD–14° 922 (Fossati et al. 2007). The offset –to subtract from the raw polarization angle– was determined to be  $2.5^\circ \pm 0.5^\circ$  in the V<sub>high</sub> filter.

The linear polarization of all 73 quasars of the Huge-LQG and of 20 out of the 34 quasars of the CCLQG has been obtained, i.e. for a total of 93 quasars. These measurements<sup>4</sup> were summarized in Table 1 of Hutsemékers et al. (2014). The error on the polarization degree is between 0.06% and 0.23%, with a mean value of 0.12%. The distribution of the debiased polarization degree is illustrated in Fig. 4.2. It shows a peak near the null value, in agree-

<sup>3</sup>We also observed HD 64299 which turned out to be polarized with  $p_{\text{lin}} = 0.17 \pm 0.04\%$ , in agreement with Masiero et al. (2007).

<sup>4</sup>Also publicly available in electronic form at <http://www.aanda.org>

ment with other polarization measurements of radio-quiet non-BAL quasars (Berriman et al. 1990; Hutsemékers, Lamy & Remy 1998). All objects are at Galactic latitudes higher than  $50^\circ$  which minimizes contamination by interstellar polarization. In this region of the sky, the interstellar polarization is around  $p_{\text{is}} \simeq 0.1\%$  with a peak of the polarization position angles near  $50^\circ$  (Fig. 4.3).

As in Hutsemékers et al. (1998; 2001; 2005), we consider that polarization is essentially intrinsic to the quasar when  $p_{\text{lin}} \geq 0.6\%$  (Berriman et al. 1990; Hutsemékers et al. 1998; Sluse et al. 2005). Out of 93 quasars, 19 have  $p_{\text{lin}} \geq 0.6\%$ . Their properties are given in Table 4.1 at the end of this chapter. For these 19 polarized quasars, the uncertainties on the polarization PAs (computed as in Eq. 3.3) are found to be  $\sigma_{\eta_b} \leq 10^\circ$  with an average value around

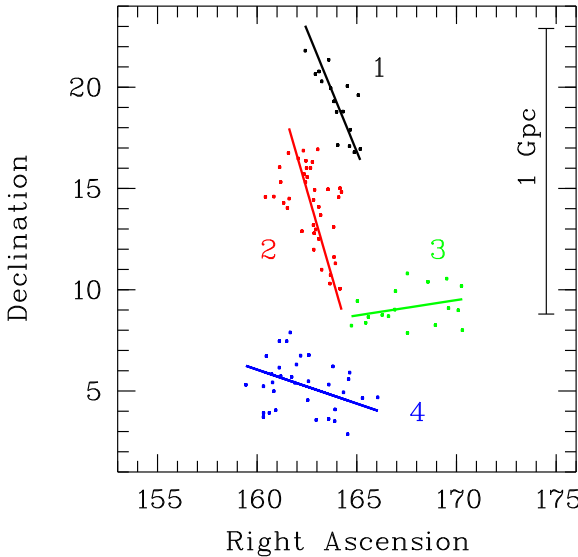


Figure 4.4: The quasar groups and their orientations on the sky. Right ascensions and declinations are in degrees. The superimposed lines illustrate the orientations of the four groups labelled 1, 2, 3, 4. The comoving distance scale at redshift  $z = 1.3$  is indicated assuming a flat Universe with  $H_0 = 70 \text{ km s}^{-1} \text{ Mpc}^{-1}$  and  $\Omega_M = 0.27$ .

## 4.2 Analysis of polarization alignments

In Fig. 4.1 we show a map of the quasar polarization vectors over the LQG structures. The map does not show any evidence of coherent orientations or alignments. The distribution of the polarization angles is flat, compatible with random orientations and with no contamination by interstellar polarization.

In order to compare the quasar polarization angles to the direction of the local structures, we consider four structures for which we determine a mean orientation, as illustrated in Fig. 4.4. Group 4 is the CCLQG defined in (Clowes et al. 2012). The Huge-LQG is divided in groups denoted 1, 2 and 3. Group 3 corresponds to the branch set of 17 quasars identified by Clowes et al. (2013). The large vertical part of the Huge-LQG is then separated

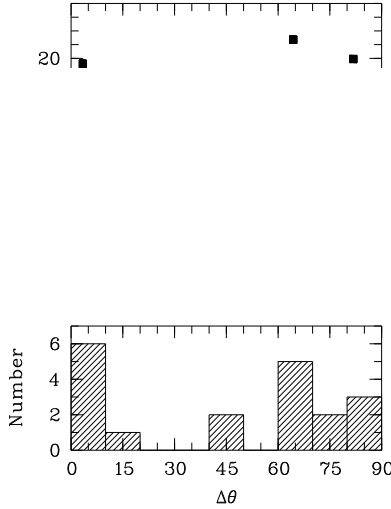


Figure 4.5: *bottom*: The distribution of the acute angle  $\Delta\psi_\chi$  (in degree) between quasar polarizations and the orientation of their host large-scale structure. *top*:  $\Delta\psi_\chi$  is plotted against the object's declination (in degrees) to illustrate the behaviour of the different quasar groups (1: squares, 2: lozenges, 3: asterisks, 4: hexagons; colors as in Fig. 4.4).

into groups 1 and 2. The mean projected direction of the structures is determined by an orthogonal regression in right ascension, declination (Isobe et al. 1990). For groups 1, 2, 3, 4, we measure the position angles  $\chi = 157^\circ$ ,  $164^\circ$ ,  $81^\circ$ , and  $109^\circ$ , respectively. We estimate the acute angle between the quasar polarization vectors and the PA of the structures to which they belong using  $\Delta\psi_\chi = \min(|\chi - \psi|, 180^\circ - |\chi - \psi|)$ .

The distribution of  $\Delta\psi_\chi$  is illustrated in Fig. 4.5 (*bottom*). It shows a bimodal distribution, with both alignments ( $\Delta\psi_\chi \simeq 0^\circ$ ) and anti-alignments ( $\Delta\psi_\chi \simeq 90^\circ$ ) in each quasar group (except group 3). The cumulative binomial probability of having nine or more quasars in the first and the last bins is  $P_{\text{bin}} = 1.4\%$ . The Kuiper test (Arsham 1988; Fisher 1993) gives a probability  $P_K = 1.6\%$  that the observed distribution is drawn from an uniform distribution. These results are robust if we consider the 28 quasars with  $p_{\text{lin}} \geq 0.5\%$  (in this case  $P_{\text{bin}} = 1.2\%$  and  $P_K = 1.0\%$ ).

A bimodal distribution of  $\Delta\psi_\chi$  is exactly what we expect if the quasar morphological axes are related to the orientation of the host large-scale structures. Indeed, the polarization of type 1 active galactic nuclei (AGN) is usually either parallel or perpendicular to the AGN accretion disk axis depending on the inclination with respect to the line of sight (e.g., Smith et al. 2004). We may assume that higher luminosity AGN (quasars) behave similarly. In Fig. 4.6, the quasar polarization angles modified according to  $\tilde{\psi} = \text{mod}(\psi, 90^\circ) + 90^\circ$  are plotted over the LQG structure, unveiling a remarkable correlation. We stress that such a behaviour cannot be due to contamination by interstellar polarization which would align all polarizations similarly.

To quantify the significance of this correlation independently of the shape of the host structure, we use the Andrews and Wasserman  $Z$  statistical test (Bietenholz 1986; Hutsemékers 1998 and Section 1.1.2 of this thesis). This test is best suited to small samples since it does



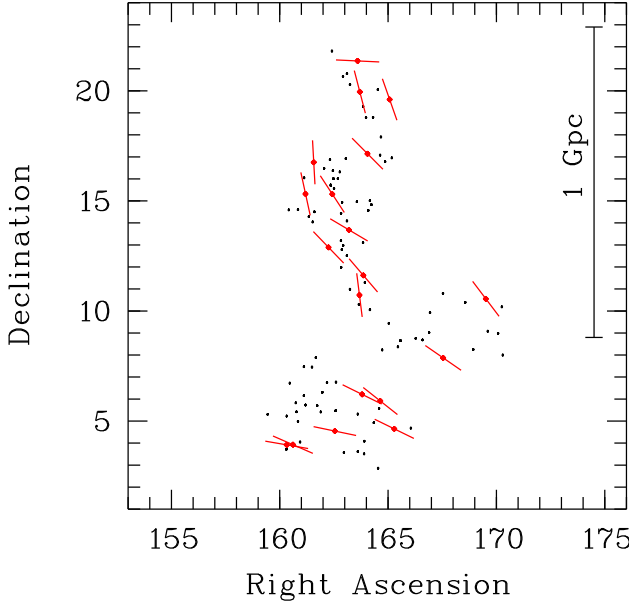


Figure 4.6: The polarization vectors of the 19 quasars with  $p_{\text{lin}} \geq 0.6\%$  are superimposed on the large-scale structure after rotation of the polarization angles according to  $\tilde{\psi} = \text{mod}(\psi, 90^\circ) + 90^\circ$ . A clear correlation is seen but we nevertheless caution against exaggerated visual impression since polarization angles are now in the range  $90^\circ - 180^\circ$ . Right ascensions and declinations are in degree. The comoving distance scale is indicated as in Fig. 4.4.

not involve angle dispersion. The idea of the Andrews & Wasserman test is to compute for each object  $i$ , the mean direction  $\bar{\psi}_i$  of its  $n_v$  nearest neighbours, and to compare this local average to the polarization angle of the object  $i$ ,  $\psi_i$ . If angles are correlated to positions, one expects, on the average,  $\psi_i$  to be closer to  $\bar{\psi}_{j=i}$  than to  $\bar{\psi}_{j \neq i}$ . As a measure of the closeness of  $\psi_i$  and  $\bar{\psi}_j$ , one uses  $D_{i,j} = \mathbf{y}_i \cdot \bar{\mathbf{Y}}_j$ , where  $\mathbf{y}_i$  is the normalized polarization vector of object  $i$  and  $\bar{\mathbf{Y}}_j$  the normalized resultant polarization vector of the  $n_v$  neighbours of object  $j$ , excluding  $j$ . Then  $Z_i$  is computed by ranking  $D_{i,j=i}$  among the  $D_{i,j=1,N}$  and the final statistics  $Z_c$  is obtained by averaging the  $Z_i$  over the sample of  $N$  objects.  $Z_c$  is expected to be significantly larger than zero when the polarization angles are not randomly distributed over positions. To make the test independent of the coordinate system, polarization vectors can be parallel transported before computing the resultant polarization vectors (Jain et al. 2004).

Here, the polarization vectors are computed using  $\mathbf{y} = (\cos \Psi, \sin \Psi)$  with the angle  $\Psi = 4 \text{ mod}(\psi, 90^\circ)$  instead of  $\Psi = 2\psi = 2 \text{ mod}(\psi, 180^\circ)$  to test for either alignments or anti-alignments (i.e., dealing with 4-axial data instead of 2-axial data, see Fisher (1993)). To estimate the statistical significance,  $10^5$  samples of 19 angles were created through Monte-Carlo simulations either by shuffling the measured angles over positions, or by randomly generating them in the  $[0^\circ, 180^\circ]$  range (Press et al. 1992). The significance level (SL) of the test is finally computed as the percentage of simulated configurations for which  $Z_c \geq Z_c^*$  where  $Z_c^*$  is the measured sample statistics. Since all quasars are in a limited redshift range, we only consider their angular positions on the sphere to build the groups of nearest neighbours.

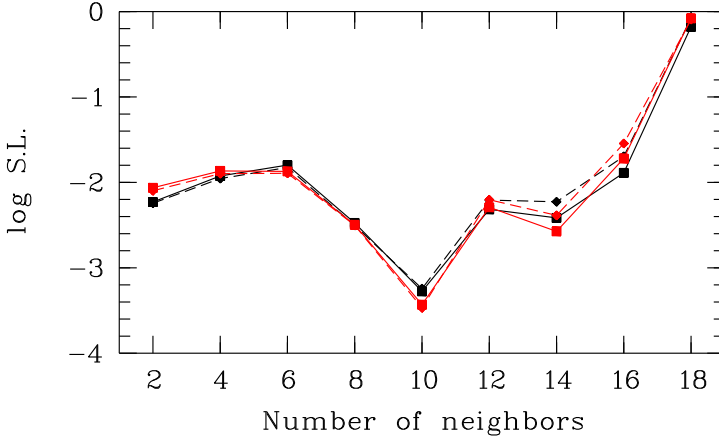


Figure 4.7: The logarithm of the significance level (SL) of the  $Z$  test applied to the sample of 19 polarized quasars, as a function of the number of nearest neighbours. The solid line refers to simulations obtained by shuffling angles over positions while the dashed line refers to simulations obtained by randomly generating angles. The statistics are computed with (in red) and without (in black) parallel transport of the polarization vectors.

The significance level of the  $Z$  test is illustrated in Fig. 4.7. It shows that the probability that the polarization angles are randomly distributed over positions is smaller than 1%. The effect is stronger ( $\text{SL} < 0.1\%$ ) when the mean orientation is computed with 10 nearest neighbours, i.e. roughly half of the sample. This number corresponds to a mean comoving distance of  $\sim 550$  Mpc, in agreement with the trend seen in Fig. 4.6. Parallel transport has little effect since all quasars lie close to each other and to the equator. We emphasize that a deviation from uniformity is only detected when using  $4 \bmod(\psi, 90^\circ)$  in the  $Z$  test and not when using  $2 \bmod(\psi, 180^\circ)$ , which means that purely parallel or perpendicular alignments are not seen (Fig. 4.1). If we consider the 28 quasars with  $p_{\text{lin}} \geq 0.5\%$ , a similar curve is obtained with the minimum shifted to  $n_v = 20$ , which corresponds to a mean comoving distance of  $\sim 650$  Mpc.

Since the width of low-ionization emission lines ( $\text{H}\beta$ ,  $\text{MgII}$ ) observed in quasar spectra correlates with the object's inclination with respect to the line of sight (Wills & Browne 1986; Brotherton 1996; Jarvis & McLure 2006; Decarli et al. 2008), we plot in Fig. 4.8 the angle  $\Delta\psi_\chi$  as a function of the quasar  $\text{MgII}$  emission line width (FWHM from Shen et al. (2011)). We see that most objects with polarization perpendicular to the host structure ( $\Delta\psi_\chi > 45^\circ$ ) have large emission line widths while all objects with polarization parallel to the host structure ( $\Delta\psi_\chi < 45^\circ$ ) have small emission line widths.

A two-sample Kolmogorov–Smirnov test indicates that there is a probability of only 1.4% that quasars with either perpendicular or parallel polarizations have emission line

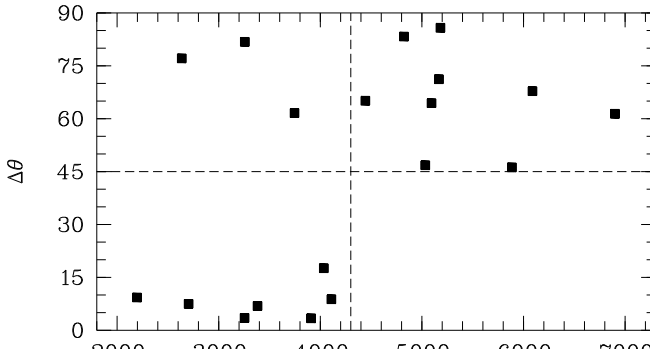


Figure 4.8: The angle  $\Delta\theta$  (in degree) between quasar polarizations and the orientation of their host large-scale structures as a function of the MgII emission line width (FWHM in  $\text{km s}^{-1}$ ).

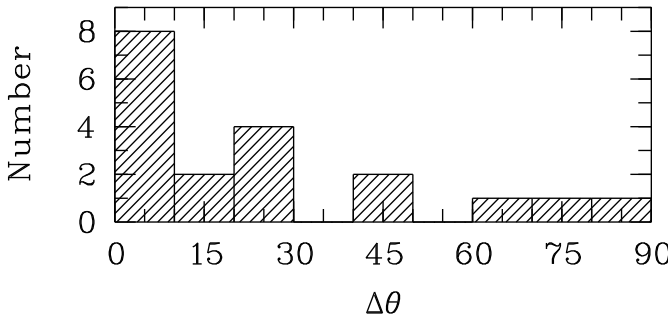


Figure 4.9: The distribution of the acute angle  $\Delta\psi\chi$  (in degrees) between quasar polarizations and the orientation of their host large-scale structure after rotating by  $90^\circ$  the polarization angles of objects with MgII emission line widths larger than  $4300 \text{ km s}^{-1}$ .

$P_K = 0.5\%$  that the observed distribution is drawn from an uniform distribution, but this value should be seen with caution since the cut at  $4300 \text{ km s}^{-1}$  is arbitrary. On the other hand, it should be emphasized that the emission line width does not only depend on inclination but also on the mass of the central black hole if the rotating disk is virialized. Quasars with lower black hole mass will have narrower emission lines whatever their inclination so that some of them may still appear anti-aligned in Fig. 4.9.

Since objects seen at higher inclinations preferentially show polarization perpendicular to their axes (Smith et al. 2004), we finally infer that quasar spin axes should be predominantly parallel to the orientation of the structures to which they belong.

<sup>5</sup>Face-on:  $i = 0^\circ$ . Edge-on:  $i = 90^\circ$ .

### 4.3 Conclusion on the alignment of optical quasar polarizations with their large-scale structure

We have measured the polarization of 93 quasars belonging to large-scale quasar groups. 19 quasars out of 93 are significantly polarized with  $p_{\text{lin}} \geq 0.6\%$ .

We found that quasar polarization vectors are either parallel or perpendicular to the large-scale structures to which they belong, and correlated to the polarization vectors of their neighbours. The probability that these results can be attributed to a random distribution of polarization angles is on the order of 1%. Such a behaviour cannot be due to contamination by interstellar polarization. Our results are robust if we consider  $p_{\text{lin}} \geq 0.5\%$  instead of  $p_{\text{lin}} \geq 0.6\%$ , or if we subtract a systematic  $p_{\text{is}} = 0.1\%$  at  $\psi_{\text{is}} = 50^\circ$  to simulate the correction of a possible contamination by interstellar polarization (Fig. 4.3).

Assuming that quasar polarization is either parallel or perpendicular to the accretion disk axis as a function of inclination, as observed in lower luminosity active galactic nuclei, and considering that broader emission lines originate from quasars seen at higher inclinations, we inferred that quasar spin axes are likely parallel to their host large-scale structures.

Galaxy spin axes are known to align with large-scale structures such as cosmic filaments (e.g., Tempel & Libeskind 2013; Zhang et al. 2013; and references therein). Till now, such alignments are detected up to redshift  $z \sim 0.6$  at scales  $\lesssim 100$  Mpc (Li et al. 2013). Detailed interpretations remain complex because the link between galaxy and halo spin axes is not straightforward, and because the strength and orientation of the alignments depend on several factors, in particular the mass of the halo and the cosmic history (e.g., Hahn et al. 2010; Trowland et al. 2013; Dubois et al. 2014). We have found that quasar accretion disk axes are likely parallel to the large-scale structures to which they belong over Gpc scales at redshift  $z \sim 1.3$ , i.e. one order of magnitude larger than currently known galaxy alignments. Although the scales involved are much larger, we may assume that similar mechanisms can explain alignments of quasar and galaxy axes with their host large-scale structure, keeping in mind that polarization-related quasar regions (accretion disk, jet, scattering region) are not necessarily well aligned with the stellar component of the host galaxy (Borguet et al. 2008; Hopkins et al. 2012), and that quasars, more prone to strong feedback mechanisms, can have a different cosmic history (Dubois et al. 2014).

Since coherent orientations of quasar polarization vectors, and then quasar axes, are found on scales larger than 500 Mpc, our results might also provide an explanation to the very large-scale polarization alignments reported by Hutsemékers et al. (1998; 2001; 2005). In this case those alignments would be intrinsic and not due to a modification of the polarization along the line of sight. The existence of correlations in quasar axes over such extreme scales would constitute a serious anomaly for the cosmological principle.

Object	$z$	LQG	$p_{\text{lin}}$ (%)	$\sigma_p$ (%)	$\psi$ ( $^\circ$ )	$\sigma_\psi$ ( $^\circ$ )	FWHM $\text{km s}^{-1}$	$\sigma_{\text{FWHM}}$ $\text{km s}^{-1}$
SDSSJ105421.90+212131.2	1.2573	1	1.04	0.08	92.6	2.2	5094	214
SDSSJ105446.73+195710.5	1.2195	1	1.89	0.23	75.2	3.5	3256	363
SDSSJ105611.27+170827.5	1.3316	1	1.29	0.08	44.8	1.8	6088	158
SDSSJ110016.88+193624.7	1.2399	1	1.14	0.23	160.4	5.9	3909	348
SDSSJ104445.03+151901.6	1.2336	2	1.25	0.11	167.5	2.5	3254	196
SDSSJ104616.31+164512.6	1.2815	2	1.25	0.11	86.9	2.5	2635	222
SDSSJ104859.74+125322.3	1.3597	2	0.72	0.13	45.6	5.3	3746	397
SDSSJ104941.67+151824.6	1.3390	2	1.31	0.13	146.4	2.9	4034	633
SDSSJ105245.80+134057.4	1.3544	2	1.32	0.11	30.2	2.4	5885	174
SDSSJ105442.71+104320.6	1.3348	2	0.73	0.11	172.8	4.4	4108	269
SDSSJ105525.68+113703.0	1.2893	2	2.55	0.10	49.1	1.1	4443	399
SDSSJ111009.58+075206.8	1.2123	3	1.81	0.17	34.2	2.7	5032	626
SDSSJ111802.11+103302.4	1.2151	3	3.97	0.10	142.4	0.7	6900	1256
SDSSJ104116.79+035511.4	1.2444	4	1.55	0.11	99.7	2.0	2195	296
SDSSJ104225.63+035539.1	1.2293	4	0.69	0.08	23.2	3.3	5182	380
SDSSJ105010.05+043249.1	1.2158	4	2.67	0.08	101.5	0.9	2703	190
SDSSJ105512.23+061243.9	1.3018	4	0.98	0.12	115.9	3.5	3381	299
SDSSJ105833.86+055440.2	1.3222	4	0.62	0.21	37.8	10.3	5167	410
SDSSJ110108.00+043849.6	1.2516	4	0.84	0.10	25.7	3.4	4823	269

Table 4.1: The sample of 19 quasars with  $p_{\text{lin}} \geq 0.6\%$ . Column 1 gives the quasar SDSS name, column 2 the redshift  $z$ , column 3 the quasar group (Fig. 4.4), columns 4 and 5 the polarization degree  $p_{\text{lin}}$  and its error  $\sigma_p$ , columns 6 and 7 the polarization position angle  $\psi$  and its error  $\sigma_\psi$ , columns 8 and 9 the MgII emission line FWHM and its error from Shen et al. (2011).



## Chapter 5

# Quasar radio polarizations align with LQG major axes

The co-evolution of the spins of galaxies with their surrounding cosmic web has been theoretically established for some time (e.g., White 1984; Heavens & Peacock 1988; Catelan & Theuns 1996; Lee & Pen 2000 and Hirata & Seljak 2004; see Joachimi et al. 2015 for a recent review). It is predicted that the spin of the dark-matter halo as well as the spin of the central supermassive black hole (SMBH) of a galaxy do not point in random directions of space, but instead point towards particular directions that are determined by the geometry of the neighbouring cosmic web (e.g., Aragón-Calvo et al. 2007; Codis et al. 2012; see Kiessling et al. 2015 for a recent review). These predictions have been supported by numerous observations (e.g., West 1994; Pen et al. 2000, Lee & Pen 2001, Faltenbacher et al. 2009, Jones et al. 2010; Li et al. 2013, Tempel & Libeskind 2013, Zhang et al. 2013; see Kirk et al. 2015 for a recent review). Unfortunately, relying on the apparent shapes of the galaxies that are used as a proxy of their spin axes, these studies are limited to the low redshift ( $z < 1$ ) Universe because the sources need to be resolved to assess their orientations with respect to their environment.

However, we have shown in the previous chapter that the orientation of the optical polarization vectors of quasars are correlated to the orientations of the large quasar groups (LQG) to which they belong, at redshift  $\sim 1.3$ . This analysis was carried out within the two large quasar groups called the CCLQG (with 34 members) and the Huge-LQG (with 73 members) identified by Clowes et al. (2013) and references therein. Given the correlation at optical wavelengths between the electric vector position angle and the morphological axis of quasar (e.g., Smith et al. 2004), we interpreted our observations as resulting from the alignment of the spin axes of the quasars with the orientation of the large-scale structure to which they belong, which is assumed to be traced by the large quasar groups.

While these alignments take place at very large scales ( $\geq 100 h^{-1}\text{Mpc}$ ), they may reflect the recognized co-evolution of the orientations of the spins of galaxies with the properties of

their surrounding large-scale structure. The study of the polarization of quasars could then constitute an additional probe of the co-evolution discussed above because it does not suffer from the observational constraints inherent to studies relying on the apparent morphologies of galaxies (Kirk et al. 2015). Moreover, studies involving quasars can be made at high redshift. Therefore, it is important to confirm the correlations that involve the polarization position angles of quasars and the characteristics of their large-scale environments, traced here by the large quasar groups. To this end, instead of measuring the polarization of all quasars belonging to a given LQG, we collect polarization measurements of quasars that belong to a sample of LQGs and compare their polarization vectors to the orientations of the groups to which the quasars belong.

In this chapter, we thus consider a large sample of LQGs built from the Sloan Digital Sky Survey (SDSS) Data Release (DR) 7 quasar catalogue in the redshift range  $1.0 - 1.8$ . For 86 quasars that are embedded in sufficiently rich LQGs, we collect radio polarization measurements with the goal to study possible correlations between quasar polarization vectors and the major axes of their host LQGs. Assuming the radio polarization vector perpendicular to the quasar spin axis (or the central SMBH spin axis), we found that the quasar spin is preferentially parallel to the LQG major axis inside LQGs that have at least 20 members. This result independently supports our observations at optical wavelengths (Chapter 4). We additionally found that when the richness of an LQG decreases, the quasar spin axis becomes preferentially perpendicular to the LQG major axis and that no correlation is detected for quasar groups with fewer than 10 members. This chapter contains the details of our analysis also presented in Pelgrims & Hutsemékers (2016).

## 5.1 Data samples and premises

The CCLQG and the Huge-LQG have first been identified with a hierarchical clustering method in the quasar catalogue of the SDSS DR7. Their detection is supported by spatial coincidence with Mg II absorbers (Clowes et al. 2013) and with a temperature anomaly in the cosmic microwave background (Enea Romano, Cornejo & Campusano 2015). These large quasar groups have been independently confirmed (Nadathur 2013; Einasto et al. 2014; Park et al. 2015) using other friends-of-friends algorithms (e.g., Huchra & Geller 1982). However, it is worth mentioning that these studies have revisited the original claim which stated that these quasar groups challenge the cosmological principle. It turned out that, following these studies, the cosmological principle is still safe.

In particular, Einasto et al. (2014) used a reliable subset of the SDSS DR7 quasar catalogue to perform their analysis. Their sample of quasars is defined in the redshift range of  $z = 1.0 - 1.8$ , in the window of the sky determined by  $\lambda_{SDSS} \in [-55^\circ, 55^\circ]$  and  $\eta_{SDSS} \in [-32^\circ, 33^\circ]$ , where  $\lambda_{SDSS}$  and  $\eta_{SDSS}$  are the SDSS latitude and longitude, re-



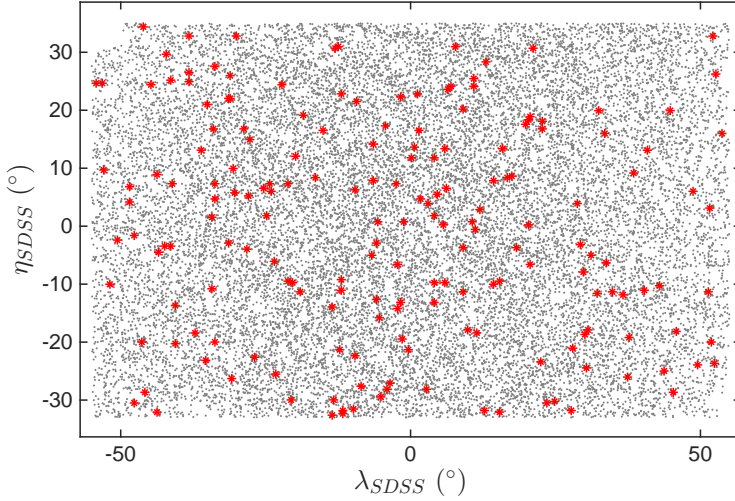


Figure 5.1: Sky map in SDSS coordinates of the 22 381 quasars contained in the Einasto sample. The 185 quasars for which we retrieved radio polarization measurement in the JVAS/CLASS 8.4-GHz surveys are highlighted in red.

spectively<sup>1</sup>, and with an additional cut in  $i$ -magnitude,  $i \leq 19.1$ . For this sample of 22 381 quasars, which we call the Einasto sample, they produced publicly available<sup>2</sup> catalogues of LQGs that are found with a friends-of-friends algorithm using different values of the linking length ( $LL$ ).

We used the sample of large quasar groups built by Einasto et al. (2014), focusing on those groups defined by  $LL = 70 h^{-1}\text{Mpc}$ . This choice is motivated by two different reasons. First, in Hutsemékers et al. (2014), the alignment of quasar morphological axes with the large-scale structures was found in the Huge-LQG and the CCLQG. These two groups are retrieved in the Einasto sample by using a friends-of-friends algorithm with that value of the linking length. Second, the richness (the number of members) of the LQGs has to be sufficiently high to allow reliable determination of their geometrical properties. For values of the linking length below  $70 h^{-1}\text{Mpc}$ , there are at most a few LQGs with a richness above 10 and none above 20. For  $LL = 70 h^{-1}\text{Mpc}$  there are several tens of rich LQGs. Above that linking length, the percolation process occurs (Nadathur 2013, Einasto et al. 2014). The large quasar groups stop to grow by including neighbouring sources and instead merge among themselves. The number of independent rich large quasar groups thus starts to decrease rapidly for  $LL \gtrsim 75 h^{-1}\text{Mpc}$ .

We searched for polarization measurements of quasars that belong to the Einasto sample

<sup>1</sup><https://www.sdss3.org/dr8/algorithms/surveycoords.php>

<sup>2</sup><http://cdsarc.u-strasbg.fr/viz-bin/qcat?J/A+A/568/A46>

to compare the polarization position angles to the position angles of the groups. At optical wavelengths, there are unfortunately too few LQG members with polarization measurements in the compilation of Hutsemékers et al. (2005). Since there is a correlation between the orientation of the radio polarization vector and the axis of the system similar to what occurs at optical wavelengths (Rusk & Seaquist, 1985), we decided to consider quasar polarization measurements from the JVAS/CLASS 8.4-GHz surveys compiled by Jackson et al. (2007), adopting their quality criterion on the polarized flux ( $\geq 1$  mJy). The choice of this sample is further motivated below.

For the Einasto sample, we therefore searched for JVAS/CLASS polarization measurements of quasars with a search radius of 0.5 arcsec. As in Chapter 3, we constrained our sample even more by only retaining polarization measurements if the condition  $\sigma_\psi \leq 14^\circ$  was satisfied, where  $\sigma_\psi$  is the error on the position angle of the polarization vector (Eq. 3.3). After verifying the reliability of the identifications, 185 objects were found. We show them in Fig. 5.1 along with all the quasars from the Einasto sample. For these 185 sources, the median of  $\sigma_\psi$  is  $1.7^\circ$ . With  $LL = 70 h^{-1} \text{Mpc}$ , 30 of the 185 quasars are found to be isolated sources and 155 belong to quasar groups with richness  $m \geq 2$ . To determine meaningful morphological position angles for the LQGs, we considered at least five members as necessary. The 86 quasars belonging to 83 LQGs with richness  $m \geq 5$  constitute our core sample in which we investigate the possible correlation between the quasar polarization vectors and the LQG orientations. According to Shen et al. (2011), these sources are all radio-loud quasars and have SMBH masses in the ranges  $\log_{10} \left( \frac{M_{\text{BH}}}{M_\odot} \right) \in [8.24, 10.12]$  and bolometric luminosities in the range  $\log_{10} L_{\text{bol}} \in [45.9, 47.7]$ , where  $L_{\text{bol}}$  is in  $\text{erg s}^{-1}$ .

The principal contamination source of the polarization position angle measurements at radio wavelengths is the Faraday rotation, which takes place in our Galaxy, but also at the source. The Faraday rotation is undesired in our study because it smears out any intrinsic correlation of the polarization vectors with other axes. Jackson et al. (2007) and Joshi et al. (2007) proved the reliability of the JVAS/CLASS 8.4-GHz surveys against any sort of biases and also showed that the Faraday rotation at this wavelength is negligible along the entire path of the light, from the source to us. Given our conclusion in Chapter 3, we verify that this is also the case for the quasar sub-sample that we consider in this chapter.

The radio polarization vector from the core of a quasar is expected to be essentially perpendicular to the (projected) spin axis of its central engine (e.g., Wardle 2013; McKinney et al. 2013). The latter can also be traced by the radio-jet axis when it is observed in the sub-arcsecond core of the quasar. The fact that radio polarization and jet axis are preferentially perpendicular supports the view that the radio polarization vectors can be used to trace the quasar spin axes. Radio polarization vectors and radio jets are known to be essentially perpendicular (Rusk & Seaquist 1985; Saikia & Salter 1988; Pollack et al. 2003; Helmboldt et al. 2007). This holds for the sources contained in the JVAS/CLASS 8.4-GHz surveys, as shown by Joshi et al. (2007). We verified that this is also true for the sub-sample

that we use here.

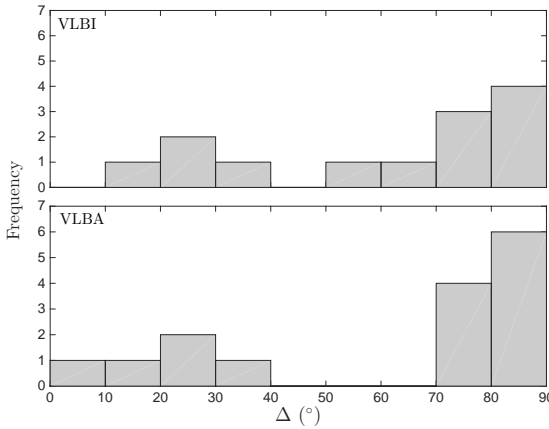


Figure 5.2: Distributions of the acute angles between the radio polarization vectors and the jet axes of the 13 quasars from the VLBI compilation of Joshi et al. (2007) (*top*) and of the 15 quasars from the VLBA sample of Helmboldt et al. (2007) (*bottom*), with correction for SDSS J122127.04+441129.7..

For our sample of 41 quasars<sup>3</sup> in LQGs with  $m \geq 10$ , we searched for jet axis information in the VLBI compilation of Joshi et al. (2007) and in the VLBA sample of Helmboldt et al. (2007). In these catalogues, we found 13 and 15 sources with jet position angle measurements, respectively<sup>4</sup>. For these objects, we computed the acute angle between the polarization vector and the jet axis. The distribution of these angles, shown in Fig. 5.2, demonstrates that even within our small sample the radio polarizations show a strong tendency to be perpendicular to the radio jets. Therefore, we safely conclude that in our sample the radio polarization vectors of the quasars trace the spin axes of the quasars and thus of their central supermassive black holes (SMBH). Any correlation found with the polarization vectors could then be interpreted in terms of the quasar spin axes.

### 5.1.1 Faraday contamination

Although Jackson et al. (2007) and Joshi et al. (2007) stated that the Faraday rotation that take place either in our Galaxy or within the source can be neglected for quasars observed at 8.4 GHz, it is important to verify that these contaminations are indeed negligible for our sample.

<sup>3</sup>The cut at  $m = 10$  is justified below.

<sup>4</sup>These two sub-samples are not independent. For the 9 objects in common, the jet position angles agree within  $\sim 20^\circ$ , except for one source that shows an offset of about  $72^\circ$  (SDSS J122127.04+441129.7). After inspecting the VLBA maps (Helmboldt et al., 2007), we realized that the sign of the position angle of the VLBA jet needs to be changed for this object.

### Faraday rotation at the source level

It was stated in Jackson et al. (2007) and Joshi et al. (2007) that the Faraday rotation of the polarization vectors that takes place within the source can be neglected for quasars observed at 8.4 GHz. However, according to Pollack et al. (2003), Zavala & Taylor (2004) and Helmboldt et al. (2007), some active galactic nuclei can harbour very strong magnetic fields that imply very high rotation measures of the order of  $\sim 500$  to few thousand  $\text{rad m}^{-2}$ . At 8.4 GHz, this would lead to high Faraday rotation, up to  $\sim 30^\circ$ , which would be dramatic for our purpose. Nevertheless, Fig. 5.2 shows that the polarization vectors at 8.4 GHz have a significant tendency to be perpendicular to the jet axes. The Faraday rotation taking place at the source might explain the observed dispersion in Fig. 5.2 but is not high enough to smear out the expected correlation between the radio-jet axes and the polarization vectors of the quasars. Moreover, an additional scatter in the polarization-vector-jet-axis correlation might arise due to curved jets (McKinney et al. 2013).

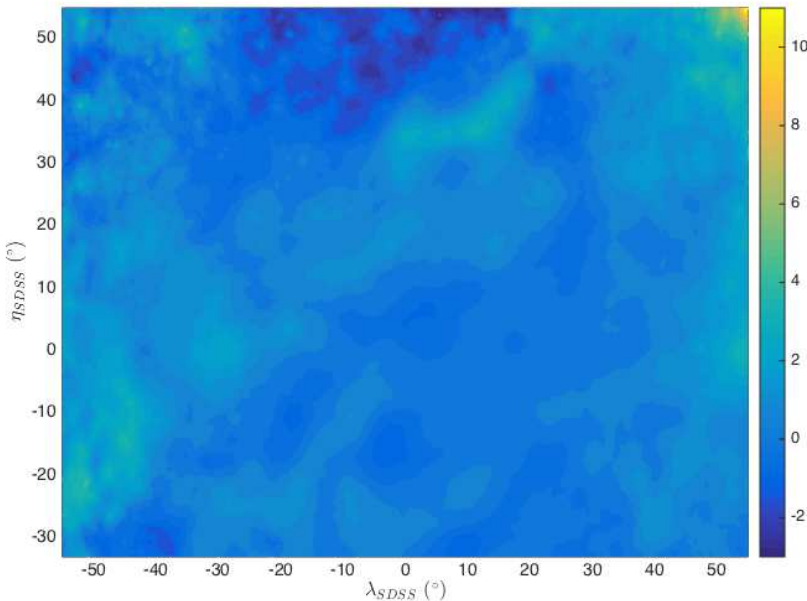


Figure 5.3: Contour plot in SDSS coordinates of the expected Faraday rotation angles at 8.4 GHz within the sky window of the Einasto sample, extracted from the whole sky rotation measure map of Oppermann et al. (2015). Colour-coded rotation angles are in degrees.

### Galactic Faraday rotation

We used the all-sky Galactic Faraday map produced by Oppermann et al. (2015) to verify that the Galactic Faraday rotation can be neglected in our analysis. From their map of ro-

tation measures, we extracted the whole sky window covered by the Einasto sample. We show in Fig. 5.3 the map of the Faraday rotation angles expected at 8.4 GHz. For the entire window, the distribution of the Faraday rotation angles that is due to the Galactic magnetic field has a mean of  $0.6^\circ$  and a standard deviation of about  $1^\circ$ .

For the source locations of our sample with JVAS/CLASS polarization measurements (the 185 sources), the contamination is even lower with a distribution having a mean of  $0.5^\circ$  and a standard deviation of  $0.6^\circ$ . We conclude that the Galactic Faraday rotation can be neglected because the rotation angles are within the error bars of the polarization data.

## 5.2 Position angles of LQGs

To define the position angle of an LQG, we can proceed in two ways. We can consider a group of quasars as a cloud of points on the celestial sphere, or we can take the three-dimensional comoving positions of the sources into account. For either approach we determine the morphological position angle (MPA) of an LQG through the eigenvector of the inertia tensor corresponding to the major axis of the set of points.

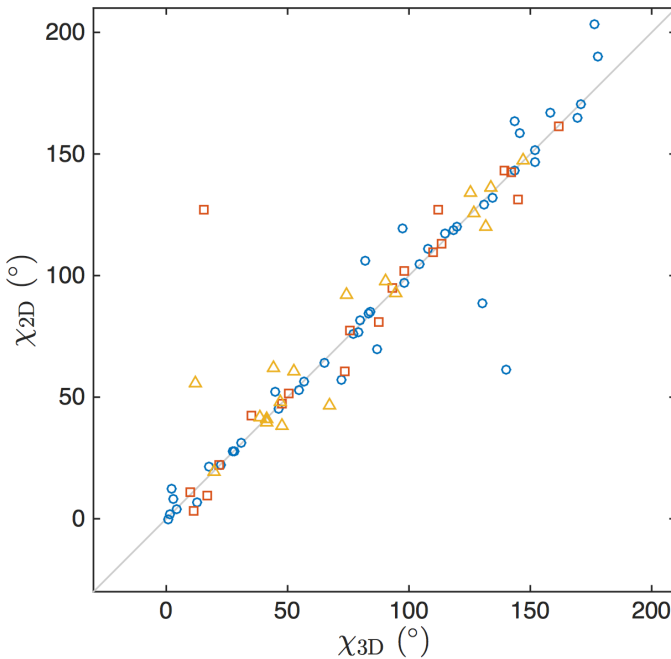


Figure 5.4: Morphological position angles (in degrees) of the large quasar groups determined with the two-dimensional method ( $\chi_{2D}$ ) as a function of those determined with the three-dimensional one ( $\chi_{3D}$ ) for the 83 LQGs with  $m \geq 5$ . Circles, squares and triangles show LQGs with richness  $m < 10$ ,  $10 \leq m < 20$  and  $m \geq 20$ , respectively. Some values of  $\chi_{2D}$  have been adjusted by  $180^\circ$  for clarity.

For the two-dimensional approach, the quasar positions are projected onto the plane tangent to the celestial sphere. The orientation of the two-dimensional cloud of points is determined by computing its inertia tensor, assuming quasars to be unit point-like masses. The position angle of the eigenvector corresponding to the most elongated axis defines the

morphological position angle of the large quasar group. We checked that this method returns position angles that are in excellent agreement (within 1 degree) with those obtained with an orthogonal regression (Isobe et al., 1990). The latter method was used in the previous chapter to define the position angles of the quasar groups.

For the second approach, the three-dimensional comoving positions (see Section 1.1.3) of the quasars are used to determine the geometrical shape of an LQG by considering its tensor of inertia, assuming quasars to be unit point-like masses. The decomposition of the tensor in terms of its eigenvalues and eigenvectors allows us to define the three principal axes of the group. A simple projection on the plane orthogonal to the line of sight of the major axis defines the position angle of the large quasar group.

As a result of the inclination of the system with respect to the line of sight, the MPAs determined by the two methods may differ. In our case, we found that they generally agree well. Indeed, we show in Fig. 5.4 a comparison of the position angles of the LQGs that we obtained by the two- and three-dimensional procedures. While the two methods often return MPAs that agree well, these quantities can be largely different owing to the apparent shape and to the inclination of the system w.r.t. the line of sight. Because the two methods return similar results, we base our discussion on the three-dimensional approach, which is more physically motivated. In our calculation, we assume the same cosmological model as in Einasto et al. (2014), that is, a flat  $\Lambda$ CDM Universe with  $\Omega_M = 0.27$ . The reduced Hubble parameter  $h$  acts only as a global scaling factor which is irrelevant for our purpose.

For either approach, the morphological position angle of each large quasar group is derived at the centre of mass of the group. In general, a quasar for which we retrieved radio polarization measurement is angularly separated from the centre of mass of its hosting group. Hence, the acute angle between the two orientations (the polarization vector and the projected major axis) depends on the system of coordinates that is used. To overcome this coordinate dependence, we used parallel transport on the celestial sphere to move the projected eigenvector from the centre of mass of the group to the location of the quasar with polarization data. By introducing  $\psi$  for the polarization position angle of a quasar and  $\chi$  for the (parallel-transported) position angle of the LQG to which it belongs, we compute the acute angle between the two orientations as

$$\Delta_{\psi\chi} = 90^\circ - |90^\circ - |\psi - \chi||. \quad (5.1)$$

The use of the parallel transport before evaluating the acute angle leads to coordinate-independent statistics. Both  $\psi$  and  $\chi$  are defined in the range  $0^\circ - 180^\circ$  and are computed in the east-of-north convention.

### 5.3 Correlation between polarization and LQG position angles

In Fig. 5.5 (top) we show the distribution of  $\Delta_{\psi\chi}$  for the 86 quasars with polarization and LQG position-angle measurements. The distribution of the full sample (top) does not show

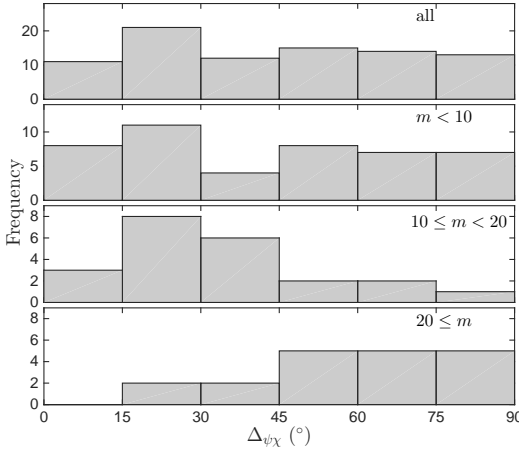


Figure 5.5: Histogram of the distribution of  $\Delta\psi_\chi$  (in degrees) for the 86 quasars with polarization–LQG position-angle measurements (*top*) and for the three sub-samples having richness  $m < 10$ ,  $10 \leq m < 20$  and  $m \geq 20$ .

any departure from uniformity. The probability given by a one-sample Kolmogorov-Smirnov (KS) test that the distribution is drawn from a uniform parent distribution is  $P_{\text{KS}} = 88\%$ . Since the alignment of optical polarization vectors with LQG orientations was found in very rich groups, and as the accuracy of the position angle of an LQG most likely depends on its richness, we divided our sample into three sub-samples with  $m < 10$  (45 objects),  $10 \leq m < 20$  (22 objects) and  $m \geq 20$  (19 objects). For the smallest LQGs ( $m < 10$ ), the distribution of  $\Delta\psi_\chi$  does not show any departure from uniformity. The probability given by a one-sample KS test that the distribution is drawn from a uniform parent distribution is  $P_{\text{KS}} = 54\%$ . However, for the larger groups, a dichotomy is observed between the two sub-samples. The polarization vector of a quasar belonging to a very rich LQG ( $m \geq 20$ ) appears preferentially perpendicular to the projected major axis of the group ( $\Delta\psi_\chi > 45^\circ$ ), whereas the polarization vector of a quasar belonging to an LQG with medium richness ( $10 \leq m < 20$ ) seems to be preferentially parallel ( $\Delta\psi_\chi < 45^\circ$ ). A two-sample KS test tells us that the probability that the two parts of the sample with  $10 \leq m < 20$  and  $m \geq 20$  have their distributions of  $\Delta\psi_\chi$  drawn from the same parent distribution is  $0.05\%$ .

For the 19 data points of the sub-sample of LQGs with  $m \geq 20$ , 15 show  $\Delta\psi_\chi > 45^\circ$ . The cumulative binomial probability of obtaining 15 or more data points with  $\Delta\psi_\chi > 45^\circ$  by chance is  $P_{\text{bin}} = 0.96\%$ . Of 22 data points of the sub-sample of LQGs with  $10 \leq m < 20$ , 17 show  $\Delta\psi_\chi < 45^\circ$ , which gives the cumulative binomial probability  $P_{\text{bin}} = 0.85\%$ . These results indicate a correlation between the position angle of the major axis of an LQG and the radio polarization position angle of its members in rich ( $m \geq 10$ ) quasar groups.

The dichotomy between the two sub-samples of LQGs with  $10 \leq m < 20$  and  $m \geq 20$  is also illustrated in Fig. 5.6, where we plot the  $\Delta\psi_\chi$  of each quasar against the richness of its corresponding LQG. Surprisingly, for  $m \geq 11$ , we even see a possible linear correlation of  $\Delta\psi_\chi$  with the richness of the large quasar groups. A Spearman correlation test on the pairs  $\Delta\psi_\chi - m$  gives a rank-order correlation coefficient of 0.54 with a probability of obtaining

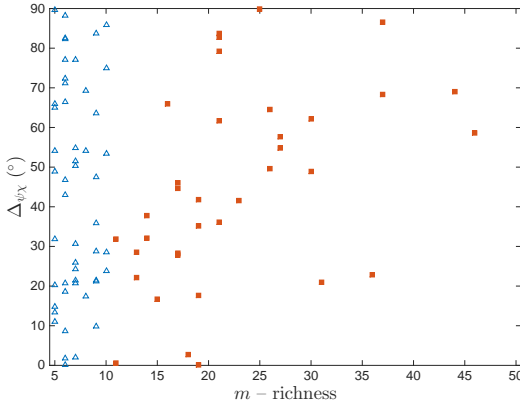


Figure 5.6:  $\Delta\psi_\chi$  versus the richness  $m$  of the LQGs. For  $m \leq 10$  and  $m \geq 11$ , symbols are triangles and filled squares, respectively.

this result by chance of 0.08 %. For  $m < 10$ , there is no specific trend of  $\Delta\psi_\chi$  with the richness in agreement with the distribution seen in Fig. 5.5. To understand whether this lack of correlation for  $m < 10$  is due to the uncertainty on the determination of the major axis position angle of the LQG, as might naively be expected for the smallest groups, we estimated the confidence interval of the morphological position angle using the bootstrap method described in the sub-section below. Keeping only MPAs for which the half-width confidence interval is lower than  $20^\circ$  (27 objects out of 45), the distribution of  $\Delta\psi_\chi$  remains uniform with  $P_{KS} = 72\%$ . The absence of alignments in quasar groups with richness  $m < 10$  is therefore likely to be real.

On the other hand, the uncertainties, both on the position angles of the major axes of the LQGs and on the polarization position angles, cannot account for the correlations that we report. The introduction of poorly defined orientations in our analysis can only scramble an existing correlation. The same argument applies to the contamination of the polarization position angles by Faraday rotation, which was found to be negligible in the previous section.

In summary, our analysis shows that the quasars that belong to very rich ( $m \geq 20$ ) large quasar groups have polarization vectors preferentially perpendicular to the projected major axis of their hosting LQGs. The polarization vectors then become more often parallel to the LQG axes when  $m$  decreases before no correlation is observed for the smallest ones ( $m < 10$ ).

In Table 5.1, we summarize the data for the 41 quasars hosted in LQGs with  $m \geq 10$ . For each quasar for which we collected polarization measurements, we list its SDSS name, its redshift, the position angle of its polarization vector, the identification index of the LQG to which it belongs (following the numbering of Einasto et al. (2014)), the richness of the group and the position angle of the projected major axis (MPA). In Fig. 5.9 we show the projection on the sky of the low and high richness parts of the LQG sample defined with  $LL = 70 h^{-1} \text{Mpc}$  that show correlations, i.e. with  $10 \leq m < 20$  and  $m \geq 20$ , respectively. We highlighted those for which we retrieved the radio polarization for at least one member



and show the orientations of the projected major axes along with the polarization vectors of the quasars.

### 5.3.1 Morphological position angles and their uncertainties

To quantify the uncertainties of the morphological position angles that characterize the large quasar groups, we use the bootstrap method. This procedure allows properly accounting for the circular nature of the data (Fisher 1993). For a given LQG of richness  $m$ , we produce  $N_{\text{sim}}$  bootstrap LQGs with the same number of members, allowing replicates. The position angle of each bootstrap LQG is determined through the inertia tensor procedure used for real groups. As this procedure is not properly defined for groups resulting from only one point, we take care in the generation of LQGs to avoid bootstrap samples that consist of  $m$  replications of the same source. The probability that such a configuration occurs is  $m^{1-m}$ . Hence, the rejection procedure can only affect poor large quasar groups. We note that even for those poor LQGs, the effect of these configurations on the evaluation of the confidence interval is negligible ( $\ll 1^\circ$ ).

For a given group of quasars, we therefore collect a corresponding distribution of  $N_{\text{sim}}$  estimates of the morphological position angle. From this distribution, we evaluate the mean and its corresponding confidence interval. For a distribution of axial-circular quantities  $\chi_k$  such as the position angle of the LQG major axes, the mean is computed as (Fisher 1993)

$$\bar{\chi} = \frac{1}{2} \arctan \left( \frac{\sum_{k=1}^m \sin 2\chi_k}{\sum_{k=1}^m \cos 2\chi_k} \right). \quad (5.2)$$

Since there is no proper definition of the standard deviation for axial-circular data, we evaluate the confidence interval of the unknown mean at the  $100(1 - \alpha)\%$  level as follows<sup>5</sup>. We define

$$\gamma_k = \frac{1}{2} \arctan \left( \frac{\sin(2(\chi_k - \bar{\chi}))}{\cos(2(\chi_k - \bar{\chi}))} \right) \quad (5.3)$$

where  $k = 1, \dots, N_{\text{sim}}$ . The  $\gamma_k$ 's are defined in the range  $[-90^\circ, 90^\circ]$ . Then we sort the  $\gamma_k$  in increasing order to obtain  $\gamma_{(1)} \leq \dots \leq \gamma_{(N_{\text{sim}})}$ . If  $l$  is the integer part of  $(N_{\text{sim}}\alpha + 1)/2$  and  $u = N_{\text{sim}} - l$ , the confidence interval for  $\bar{\chi}$  is  $[\bar{\chi} + \gamma_{(l+1)}, \bar{\chi} + \gamma_{(u)}]$ . We choose to compute the confidence interval of  $\bar{\chi}$  at the 68% confidence level. We define the half-width of the confidence interval as  $\text{HWCI} = (\gamma_{(u)} - \gamma_{(l+1)})/2$ .

Using the bootstrap method with 10 000 simulations, we evaluated the half-width confidence intervals for the 83 LQGs of our sample. The distribution of HWCI corresponding to the three-dimensional evaluation of the morphological position angles is shown in Fig. 5.7 for different cuts in richness and is compared to those obtained from the two-dimensional procedure. In general, the confidence intervals are lower when the two-dimensional procedure is chosen to estimate the LQG position angles. The highest values of the HWCI's ( $\geq 20^\circ$ ) can in general mostly be attributed to poor LQGs with  $m < 10$ , as naively expected.

<sup>5</sup>This procedure is based on the method described in (Fisher 1993).

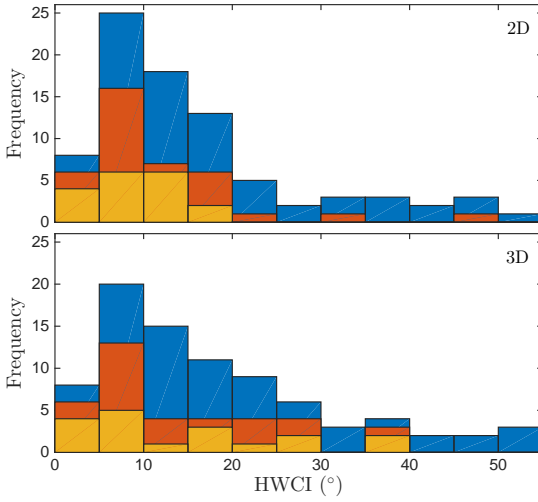


Figure 5.7: Histograms of the HWCI's for the MPA values obtained for the 83 independent LQGs with the two- (*top*) and three-dimensional (*bottom*) approaches (see Section 5.2). The HWCI's are evaluated using the bootstrap method as explained in the text. Histograms are for  $m \geq 5$  (blue),  $m \geq 10$  (orange) and  $m \geq 20$  (yellow).

## 5.4 Discussion

As discussed in Section 5.1, the radio polarization vector of a quasar is expected to be essentially perpendicular to the spin axis of its central engine. The correlation that we found between the polarization vectors and the major axes of the host large quasar groups might thus reflect an existing link between the spin axes of the quasars and the major axes of the host LQGs.

Our analysis independently supports the view that the spin axis of quasars that belong to very rich LQGs are preferentially parallel to the major axes of their hosting LQGs, as found in Chapter 4. In addition, we found that the quasar-spin axes become preferentially perpendicular to the LQG's major axes as the richness of the LQGs decreases, down to  $m \geq 10$ .

Regardless of the richness dependence that we discuss below, our observation also suggests that the quasar spin axes have an intrinsic tendency to align themselves within their host large quasar groups. The observations of Jagannathan & Taylor (2014) that radio jets in the GRMT ELAIS N1 Deep Field align with each other over scales of  $50 - 75 h^{-1} \text{ Mpc}$  at redshift  $z \gtrsim 1$  support our interpretation (Taylor & Jagannathan, 2016).

As discussed in the introduction, the fact that the spin axes of black holes are found to align with their surrounding large-scale structures, which are assumed to be traced by LQGs, could be understood in the framework of the tidal torque theory if we accept that these predictions can be extrapolated to larger scales. However, and as far as we know, a richness dependence of the relative orientation is not a predicted feature of this theory. We therefore explore our data set to determine whether the richness dependence hides another dependence that could be more physically motivated.

For this exploratory analysis, we relied on our core sample of LQGs with  $m \geq 10$  and for which we have radio polarization measurements for at least one of their quasar member (Table 5.1). For LQGs with  $m \geq 10$ , the median of the diameters (the largest separation between two members in groups) is about  $310 h^{-1}$  Mpc and the median separation of the closest pairs is about  $45 h^{-1}$  Mpc.

### Richness dependence and quasar intrinsic properties

N-body simulations have shown that the direction towards which the spin axes of dark-matter haloes preferentially point relative to the large-scale structure depends on their mass (Codis et al. 2015). As the masses of the SMBH and the host dark-matter halo are thought to be linked and as their spin axes might be aligned at high redshift (Dubois et al. 2014), we searched for a possible dependence of  $\Delta_{\psi\chi}$  with the black hole mass. Using the Spearman correlation test, we found that the SMBH masses (from Shen et al. 2011) do not show any correlation with  $\Delta_{\psi\chi}$  or with the richness of the host LQG. The same conclusion is reached if we consider other quasar properties reported in Shen et al. (2011), such as the radio-loudness, the width of the emission lines, or the redshift. There is thus apparently no hidden relation of  $\Delta_{\psi\chi}$  with quasar properties that could explain the richness dependence of  $\Delta_{\psi\chi}$ .

### Richness dependence and LQG characteristics

In Section 5.2 we used the inertia tensors of the large quasar groups to assign their orientations in the three-dimensional comoving space. This resulted in fitting ellipsoids to the quasar systems. In this subsection, we use the relative lengths of the principal axes of the ellipsoids to characterize their shapes.

The richness of LQGs is of course correlated with their size, both in comoving space and in the projection on the sky. The larger the comoving volume of the ellipsoid or the larger the projected area on the celestial sphere, the better the black hole spins align with the major axis of the system. However, the correlations of the acute angles between the polarization vectors and the projected LQG major axes with these quantities are not stronger than with the richness of the groups that we observed in Fig. 5.6.

Analyses studying the alignments of galaxy axes in the low-redshift Universe found evidence for a dependence on the geometrical properties of their surroundings. Namely, given that the studied galaxies are in the neighbourhood of filaments or sheets (walls) of the cosmic web, their spin axes tend to point preferentially in different directions with respect to those defined by their cosmic environment (e.g., Tempel & Libeskind 2013; Zhang et al. 2013; Li et al. 2013; see Kirk et al. 2015). For instance, these studies show that the spin axes of spiral galaxies in sheets are not correlated to the vectors normal to the sheets but that they are significantly correlated with the axes of the neighbouring filaments. Furthermore, the importance of this correlation is likely to be dependent on the distances of the galaxies

to the filaments. These behaviours are predicted from theory and are observed in simulated universes (e.g., Codis et al. 2012).

Let  $a$ ,  $b$  and  $c$  be the comoving lengths of the major, intermediate and minor axes of the ellipsoids fitted to the LQGs, respectively. By definition:  $a \geq b \geq c$ . The geometries of the LQGs can be characterized through parameters derived from the ratio of these lengths. We define  $\tilde{b} = b/a$  and  $\tilde{c} = c/a$ , which implies  $1 \geq \tilde{b} \geq \tilde{c}$ . We further introduce the parameter  $\mathcal{O}$  related to the oblateness of the system. This parameter is defined as

$$\mathcal{O} = \frac{2\tilde{b} - (1 + \tilde{c})}{1 - \tilde{c}} \quad (5.4)$$

and takes values in the range  $[-1, 1]$ .  $\mathcal{O} = 0$  corresponds to the cases where the length of the intermediate axis of the ellipsoid is precisely at the middle of the lengths of the minor and major axes. This value corresponds to the transition between prolate ( $\mathcal{O} < 0$ ) and oblate ( $\mathcal{O} > 0$ ) systems. The asymptotic configurations  $\mathcal{O} = -1$  and  $\mathcal{O} = 1$  correspond respectively to (thick) filaments and to (thick) sheets, i.e. to cylindrical and disk-like systems.

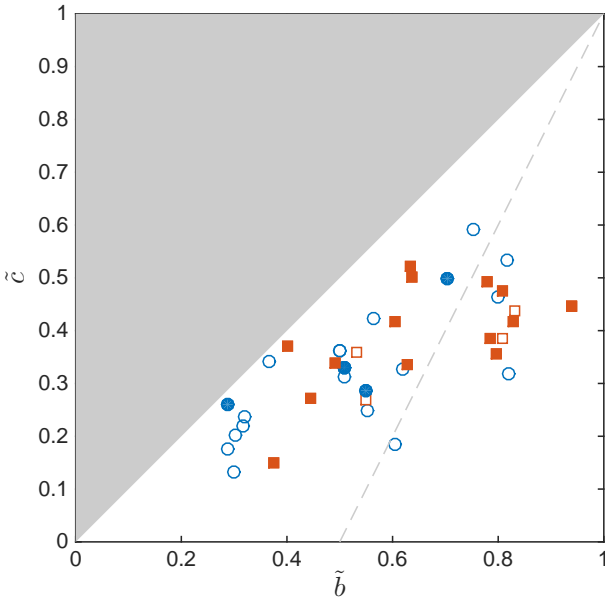


Figure 5.8: Morphological plane summarizing the geometrical properties of the LQGs containing at least one polarized quasars and having  $m \geq 10$ . The grey region is forbidden by definition of the parameters  $\tilde{b}$  and  $\tilde{c}$ . The dashed-grey line is for  $\mathcal{O} = 0$  and marks the transition between prolate and oblate systems (see text). LQGs with  $m$  below and above 20 are displayed by circles and squares, respectively. Filled symbols are for those where  $\Delta\psi_\chi > 45^\circ$ .

We show in Fig. 5.8 the distribution in the plane  $(\tilde{b}, \tilde{c})$  of the 38 independent LQGs that contain at least one quasar for which we retrieved radio polarization measurements and that have richness  $m \geq 10$ . As seen from this figure, there is no significant difference in the geometrical properties between LQGs that have a richness  $10 \leq m < 20$  and those that have  $m \geq 20$ . Similarly, the large quasar groups with  $\Delta\psi_\chi > 45^\circ$  or  $\Delta\psi_\chi \leq 45^\circ$  do not distribute differently in the morphological plane.

Inside this sample of 41 LQGs, we also searched for correlations between the acute angles  $\Delta_{\psi\chi}$  and the geometrical characteristics of the LQGs such as oblateness or departure from spherical or cylindrical symmetry and also considered the position of quasars with radio polarization measurements relative to their host large quasar groups. We did not find any convincing correlation with these physical properties that could be hidden in the richness dependence.

A quantity that is related to the richness of an LQG and that could have a better physical meaning is its density. We can naively define the density of an LQG as  $\rho = m/V$ , where  $V$  is the comoving volume of its fitted ellipsoid. In our core sample of LQGs, there is a relation between the richness and the density: the richer a large quasar group, the lower its density. We then applied a Spearman correlation test to the pairs  $\Delta_{\psi\chi} - \rho$ , which resulted in rank-order correlation coefficient of  $-0.50$  with a probability of obtaining this result by chance of  $0.19\%$ , if we consider all the LQGs with  $m \geq 11$  and at least one  $\Delta_{\psi\chi}$  measurement (the sub-sample studied in Section 5.3). SMBHs spin axes are thus parallel to the host LQG axis when the density of the latter is low and perpendicular when the density is high. The strength of this correlation is similar to the strength of the  $\Delta_{\psi\chi} - m$  correlation. The dependence between  $\Delta_{\psi\chi}$  and the richness  $m$  could then reflect a dependence between  $\Delta_{\psi\chi}$  and  $\rho$ , which might be easier to interpret. Codis et al. (2015) have shown that the spin axes of the dark-matter haloes of galaxies are preferentially parallel to their neighbouring filaments when the halo masses are low or, equivalently, when the density of their cosmic environment is low. When the density of the environment increases, the halo spin axis starts to avoid alignment with the filaments to finally point preferentially perpendicular to them. Our observations might thus support these predictions if we assume that, at least at redshift  $z \geq 1.0$ , (i) a similar behaviour can be expected for the spin axes of the central SMBH of quasars, (ii) the density of an LQG reflects the density of the surrounding cosmic web, (iii) the LQGs can be used to trace the large-scale structures, and (iv) correlations that occur between the galaxy spin axes and filaments also occur at larger scales between quasar-spin axes and LQG major axes.

## 5.5 Concluding remarks

In this chapter, we have further studied the correlation between the spin-axis orientations of the supermassive black holes at the centres of quasars with the orientations of the large quasar groups to which they belong. To do this, we considered a large sample of LQGs drawn from a reliable sub-sample of the SDSS DR7 quasar catalogue in the redshift interval  $[1.0, 1.8]$  to which a friends-of-friends algorithm has been applied with a linking length of  $70 h^{-1}\text{Mpc}$  (Einasto et al. 2014). We chose this value of the linking length because it allows to recover the LQGs in which we found the correlation at optical wavelengths. Because too few optical polarization data are available for the quasars that belong to the Einasto sample, we used radio polarization measurements from the JVAS/CLASS 8.4-GHz surveys

(Jackson et al. 2007). This sample is claimed to be free of biases that might affect the polarization angles. Furthermore, the polarization vectors at 8.4 GHz have a strong tendency to be perpendicular to the spin axes of the SMBHs in the quasar cores.

We retrieved reliable polarization measurement for 185 quasars belonging to the Einasto sample. Among these, 86 were found in LQGs populated by at least five members, a minimum value to determine reliable position angles. To compare the position angles of the quasar polarization vectors with the position angles of the system to which the quasars belong, we studied the LQGs through their inertia tensors in the three-dimensional comoving space.

For rich quasar groups ( $m \geq 20$ ), we found that the spin axes of the supermassive black holes are preferentially parallel to the major axes of their host large quasar groups. This result adds weight to the previous finding at optical wavelengths that in two large quasar groups the quasar spin axes (inferred from polarizations) align with the group axes. Combined with the initial discovery, our analysis indicates that the alignments of the SMBH spins axes with the LQG major axes do not depend on the quasar radio loudness.

Additionally, the use of a large sample of LQGs allowed us to probe the alignments for a wide variety of quasar systems. We unveiled a surprising correlation: the relative orientations of the spin axes of quasars with respect to the major axes of their host LQGs appear to depend on the richness of the latter, or equivalently on the density of objects. The spin axes of SMBHs appear preferentially parallel to the major axes of their host LQGs when the latter are very rich (or have a very low density), while the spin axes become preferentially perpendicular to the LQG major axes when the richness decreases to  $m \geq 10$  or, equivalently, when the quasar density increases to  $1.5 \cdot 10^{-5} (h^{-1} \text{ Mpc})^{-3}$ . No correlation is observed below this richness or above this density. Possible interpretations were discussed in Section 5.4, but this intriguing feature needs to be confirmed.

Numerical simulations show that the spin axes of the dark-matter haloes align with preferred directions of the cosmic web (e.g., Codis et al. 2012). At high redshift, the axes of the supermassive black hole spin and of the dark-matter halo spin are predicted to align (e.g., Dubois et al. 2014). At high redshift, thus, the SMBH spin axes might preferentially align with specific directions of the neighbouring large-scale structures as suggested by Lagos et al. (2009). While happening at much larger scales, our observations are in qualitative agreement with this expectation which could, in principle, be tested from simulation. Note that, if simulations catch properly the physics of structure formation, no alignment of the black hole spins with their large-scale structures are expected at low redshift due to consecutive mergers and black hole coalescence (e.g., Dubois et al. 2014).

In agreement with the view that the richest large quasar groups at high redshift most likely represent the progenitors of complexes or chains of superclusters (Einasto et al., 2014), the correlation that we found might be the high-redshift counterpart of the alignments at  $z \sim 0$  of clusters of galaxies with the superclusters in which they are embedded (e.g., Einasto et al. 1980; West 1999).

The study of quasar polarization appears to be a promising tool to probe the correlation of the spins of extragalactic objects across a very broad range of redshift. It is mandatory, however, to understand better the connection between the cosmic web and the large quasar groups that are defined via friends-of-friends algorithms.

SDSS name	$z$	PPA ( $^{\circ}$ )	LQG ID	$m$	MPA ( $^{\circ}$ )
074809.46+300630.4	1.6942	13.3	7	18	15.9
083740.24+245423.1	1.1254	58.0	184	15	74.8
090910.09+012135.6	1.0255	130.4	410	10	36.2
091204.62+083748.2	1.5388	103.3	356	30	41.1
091439.42+351204.5	1.0738	127.6	267	14	95.5
091641.76+024252.8	1.1019	162.0	410	10	35.5
091648.90+385428.1	1.2656	163.7	396	17	12.1
093105.33+141416.4	1.0997	56.2	548	17	10.2
094148.11+272838.8	1.3063	161.5	652	19	143.9
095956.04+244952.4	1.4803	91.1	844	19	49.3
104552.72+062436.4	1.5091	25.7	1199	21	126.6
104831.29+211552.2	1.4810	0.2	1215	14	142.3
105431.89+385521.6	1.3662	82.3	1266	23	123.8
112229.70+180526.4	1.0414	156.1	1437	21	94.3
112814.74+225148.9	1.0809	112.7	1453	26	48.2
113053.28+381518.6	1.7413	44.7	1507	13	22.7
114658.29+395834.2	1.0882	89.3	1501	11	89.8
115232.86+493938.6	1.0931	139.0	1643	10	162.7
115518.29+193942.2	1.0188	16.0	1716	11	47.8
120518.69+052748.4	1.2956	166.9	1857	13	15.5
121106.69+182034.2	1.5150	163.0	1925	21	19.1
122127.04+441129.7	1.3444	57.9	2002	36	35.0
122847.42+370612.0	1.5167	70.7	1996	17	98.5
123505.80+362119.3	1.5983	54.2	1996	17	98.8
123736.42+192440.5	1.5334	178.2	2011	37	66.5
123757.94+223430.1	1.4175	155.0	2011	37	68.3
123954.13+341528.8	1.1698	111.6	2151	19	111.7
130020.91+141718.5	1.1060	125.5	2136	21	41.7
133915.90+562348.1	1.4254	115.3	2287	31	94.3
134208.36+270930.5	1.1898	18.0	2650	44	129.0
134821.89+433517.1	1.1140	8.4	2563	10	113.5
135116.91+083039.8	1.4398	97.5	2580	26	47.9
135351.58+015153.9	1.6089	111.9	2714	21	14.7
140214.81+581746.9	1.2673	137.9	2809	16	71.9
142251.89+070025.9	1.4505	145.0	2813	19	109.9
142330.09+115951.2	1.6127	15.3	2961	30	146.4
145420.85+162424.3	1.2763	110.5	3198	10	139.0
150124.63+561949.7	1.4670	166.2	3126	27	43.8
150910.11+161127.7	1.1474	75.3	3219	46	134.0
152037.06+160126.6	1.4669	103.1	3408	27	48.4
152523.55+420117.0	1.1946	164.8	3375	25	74.8

Table 5.1: Data for the 41 quasars with  $\Delta\psi_{\chi}$  measurements and belonging to rich ( $m \geq 10$ ) LQGs. Column 1 gives the SDSS quasar name, Col. 2 the redshift  $z$ , Col. 3 the polarization position angle (PPA) in degrees (East-of-North), Col. 4 the identification index from the catalogue of Einasto et al. (2014) of the LQG to which the quasar belong, Col. 5 the number of member in that LQG  $m$  and Col. 6 the position angle (in degrees, East-of-North) of the major axis of the LQG when projected on the sky and parallel transported at the location of the quasar for which we collected polarization measurements.



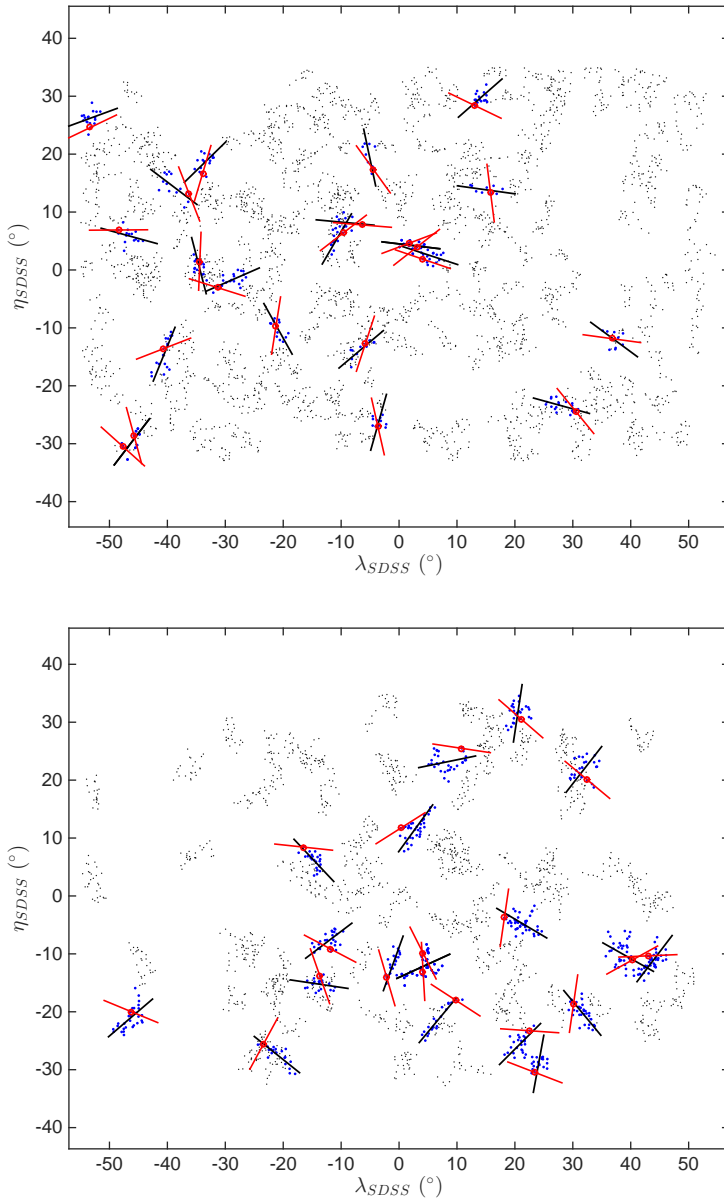


Figure 5.9: Projection on the sky, in SDSS coordinates, of the LQGs having richness in the range 10–19 (*top*) and larger than 20 (*bottom*). The LQGs (clouds of grey dots) containing at least one quasar with polarization measurements (circled in red) are highlighted in blue. The black lines trace the orientation of the projected major axes of the groups (here at the centres of masses). The red lines give the orientations of the polarization vectors. All lines are of equal lengths for visualization. The polarization vectors are preferentially parallel to the MPAs of the groups (*top*) and preferentially perpendicular (*bottom*).



# Conclusion and outlook

Quasars, as well as less luminous active galactic nuclei, have the particularity to emit polarized light due to the anisotropic geometrical configuration of their components or to their inherent magnetic fields. The study of polarization thus provides a unique tool to probe the characteristics of the sources of electromagnetic radiation in quasars and of the medium through which this radiation propagates. Along the years, the study of the polarization of quasars has proven its power to infer their morphology and their orientation with respect to the line of sight of the observer while they are too far to be resolved by telescopes.

The comparison of the orientations of the polarizations from quasars that are separated by billions of light-years has led to the striking discovery that they are aligned instead of being randomly distributed as expected (Hutsemékers 1998). Since then, this discovery has been confirmed and the significance of the correlations enhanced (Hutsemékers & Lamy 2001; Jain et al. 2004 and Hutsemékers et al. 2005). These alignments may challenge our current understanding of the Universe as they imply correlations over cosmological scales ( $\gtrsim 1$  Gpc), much beyond the hypothesized homogeneity scales of the Universe.

These alignments of quasar-polarization vectors did not find obvious explanation as the variety of scenarios that have been proposed among the years shows. A non-exhaustive list of these includes: fundamental constant variation, cosmic strings, cosmic birefringence, cosmological magnetic fields, new dark-matter particle candidates, anisotropic or rotational cosmological models, bad sampling of the data set,... (see e.g., Chang et al. 2012; Poltis & Stojkovic 2010; di Serego Alighieri 2015; Urban & Zhitnitsky 2010; Tiwari & Jain 2015; Das et al. 2005; Payez, Cudell & Hutsemékers 2008; Hutsemékers et al. 2011; Agarwal, Kamal & Jain 2011; Hutsemékers et al. 2005; Ciarcelluti 2012; Kuvshinova & Panov 2014; Joshi et al. 2007). Nevertheless, none have been successful to account properly for the observational specificities of the alignments (e.g., Hutsemékers et al. 2010; di Serego Alighieri 2015).

We devoted this work to a careful analysis of this intriguing and unsolved anomaly. In Chapter 1, we reviewed statistical tests that have been extensively used to characterize the polarization alignments. We then introduced a new and independent statistical method. The latter allowed us to re-analyse independently the current data set of optical-polarization measurements of 355 quasars in Chapter 2. It further allowed us to proceed to an unbiased identification of the regions of the space where the alignments of the quasar polarization

vectors are the more significant. As a result of our analysis, the very-large-scale alignments of the quasar-optical-polarization vectors are put on stronger grounds.

Given that the status of such alignments at radio wavelengths was not clear, and especially that the redshift of the sources had never been properly taken into account, we proceeded in Chapter 3 to a new analysis of the polarization vectors of a large sample of flat-spectrum radio sources drawn from the JVAS/CLASS 8.4-GHz surveys which is (claimed) free of biases (Jackson et al. 2007). Contrary to previous studies, we found significant large-scale alignment patterns within this sample. Interestingly, these alignments involve only quasars among the variety of flat-spectrum radio sources contained in the sample. While our findings prove difficult to explain either by biases in the data set or by physical effects, the fact that regions of quasar-radio-polarization alignments are found either nearby or within the regions of the sky where optical-polarization alignments are the most significant is striking and suggests a common explanation. Unfortunately, as we discussed in Chapter 3 a combination of the two data sets and a comparison of the alignments at optical and radio wavelengths turned out to be difficult because of poor overlap of the full samples. A systematic comparison of the alignments from both radio and optical samples is still lacking and should be investigated in the future when more data are available. Meanwhile, the fact that the alignments features from both spectral bands may be due to the same physical mechanism is worth keeping in mind and would imply strong phenomenological constraints on possible scenarios.

More polarization data are thus clearly needed to provide a better assessment. A more homogeneous sample is required at optical wavelengths and an observational confirmation of the reliability of the radio data set is mandatory. In this respect, we are looking forward to the upcoming compilation of quasar optical polarization measurements which will increase the sample size and provide a better sampling in redshift (Sluse 2015, private communication).

As we were searching for the mechanism responsible for these very large-scale alignments of the polarization vectors, we measured the optical polarizations of the quasars belonging to two very large quasar groups (LQG) at a cosmological redshift  $z \sim 1.3$ , i.e. when the Universe was about one third of its age (Clowes et al. 2013). As we showed in Chapter 4, quasar polarization orientations were found to be either parallel or perpendicular to the orientations of the LQGs. Given the established relation between the orientations of the optical polarization vectors of quasars and the directions of their structural axes, we inferred that the spin axes of the supermassive black hole at the centre of quasars tend to align themselves with their neighbouring large-scale structures assumed to be traced by the LQGs. This interpretation is supported by spectral properties of the targeted quasars. Indeed, those that show a broader Mg II emission spectral line, and thus that are viewed with higher inclinations, are those that have polarization vectors preferentially perpendicular to the LQG axes, so that the black-hole spins are parallel. To confirm our observations and interpretations we submitted a proposal for new optical polarization measurements of quasars that belong to another very rich large quasar group that has an average redshift of  $\sim 1.6$  from the LQG sample of

Einasto et al. (2014). Unfortunately, the survey has not been completed and only three new reliable data points have been obtained. It is worth mentioning that the three new data points confirm our expectations.

In order to confirm independently our previous results and to question further the correlations that the black hole spin axes have with the major axes of the LQGs they belong to, we used quasar radio polarization measurements from the JVAS/CLASS 8.4-GHz surveys (Jackson et al. 2007) and a large sample of LQGs drawn from the high-redshift part of the SDSS DR7 quasar catalogue (Einasto et al. 2014). Polarization in this radio sample is thought to be due to synchrotron emission in the core of the active galactic nucleus where the magnetic field is expected to be parallel to the central black hole spin axis (Jackson et al. 2007; Wardle 2013). Hence, irrespective of the inclination of the sources with respect to the line of sight of the observer, the polarization vectors are expected to be perpendicular to the spin axes of the black holes and therefore perpendicular to the LQG major axes if the black hole spin axes actually align with them. Our analysis, presented in Chapter 5, reinforces our previous study at optical wavelengths. We indeed found that black hole spin axes of quasars that belong to very rich groups align with the major axes of the large quasar groups. We additionally found that the preferred spin axis orientations significantly depend on the richness of the quasar groups.

As discussed in Chapters 4 and 5, what could cause the spin axes of the black holes at the centre of quasars to be aligned with the large quasar group axes is the angular momentum transfer from matter during its gravitational collapse to form galaxies in the young Universe. Supported by N-body Monte Carlo simulations, the tidal torque theory tells how galaxies acquire their spin during their formation and how it evolves while they drift through the cosmic web which is in constant evolution (e.g., White 1984; Heavens & Peacock 1988; Codis et al. 2012; Laigle et al. 2015). Given this scenario the spin of the galaxies and so their apparent morphologies are expected to be correlated to specific directions in space. These are defined by the geometrical characteristics of the gravitational potential of the surrounding matter. Such an arrangement of matter and angular momentum is not only observed in simulations but is also inferred from real observations in the low redshift Universe (e.g., Tempel & Libeskind 2013; Zhang et al. 2013; Li et al. 2013). Our analyses provide the first high-redshift observational confirmation of this effect, but on larger scales than predicted. Indeed, according to theory, the intrinsic alignments between the spins of galaxies are observed to drop rapidly as their separation increases (see Kirk et al. 2015 for a review). Our observations show that the story might be different and that these correlations may happen at much larger scales. This would be true at least in the young Universe and for galaxies that harbour active nuclei. Our results constitute a hint that there might be a missing ingredient in our understanding of the large-scale structure formation and more generally in the current cosmological paradigm.

Moreover, our analyses imply that the intrinsic alignments could have non-vanishing effects for the upcoming experiments that intend to constrain the cosmological parame-

ters. This is especially relevant for those that will investigate the nature of the dark energy through the study of the deformation of the galaxy images induced by massive objects located along the path of the light, deformation known as the weak gravitational lensing effect (Laureijs et al. 2011; Amendola et al. 2013; Kirk et al. 2015). It is therefore of prime importance to understand these large-scale correlations. In particular, this requires a better understanding of the relation between the large-scale structures of the Universe and the large quasar groups defined through friends-of-friends algorithms from the quasar distribution. Indeed, the link between the quasars and the large-scale structures is not well established. While quasars are expected to be located in sufficiently dense regions of the matter distribution for the supermassive black holes to form, it is not guaranteed that they trace the highest density regions and hence, the large-scale structures of the Universe (Fanidakis et al. 2013). This assumption actually underlaid the interpretation given in Chapters 4 and 5.

As shown by analyses in the local Universe, quasars are likely to be located at the peripheries of the clusters and filaments. Nearby quasars, typically found in small groups and poor clusters of galaxies, are indeed located in relatively low-density and large-scale environments that surround the supercluster of galaxies (e.g., Söchting, Clowes & Campusano 2002, 2004; Coldwell & Lambas 2006; Lietzen et al. 2009, 2011). It has been suggested that, at high redshift, the large quasar groups mark the precursors of the superclusters that we observe in the local Universe (e.g., Einasto, Joeveer & Saar 1980; West [1994; 1999]) and that they are perhaps the seeds of supercluster complexes such as the famous Sloan Great Wall (Einasto et al. 2011). This still needs to be confirmed. Forthcoming deep and wide galaxy surveys will definitely help to understand better the interplay between quasars and their surroundings as well as to question the physical nature of the large quasar groups. In this respect, cross-correlations of the quasar distributions with maps of the cosmic microwave background may help.

Indeed, the photons from the cosmic microwave background (CMB) have travelled from the surface of last scattering to Earth, have been deflected, redshifted and blue shifted by the gravitational potentials of massive structures and have been heated up by energetic free electrons filling the haloes of these structures (e.g., Challinor, Ford & Lasenby 2000; Gawiser & Silk 2000; Wands et al. 2015). These phenomena, encoded in the CMB and known as the weak lensing, the integrated Sachs-Wolfe and the thermal Sunyaev-Zel'dovich effects, have been successfully mapped by the Planck satellite and contain information about the large-scale structures. If the large quasar groups somehow trace the cosmic web, then characteristic anisotropies in the CMB should correspond to them. These imprints could be detected by stacking methods such as those that allowed the discovery of the integrated Sachs-Wolfe effect induced by low-redshift superstructures embedded in our accelerated-expanding Universe (Padmanabhan et al. 2005; Granett et al. 2008; Planck Collaboration XXI 2015). Recent pioneering work have been done in that direction (e.g., DiPompeo et al. 2015; Enea Romano, Cornejo & Campusano 2015). They demonstrate that such an analysis can be conducted to understand better what is the role of quasars in the evolution of the large-scale

structures and, more importantly for our purpose, to investigate the physical reality of the large quasar groups.

With respect to this, our observation of the correlation of quasar polarization orientations with the axes of the large quasar groups can be read as an argument in favour of the reality of these large-scale quasar structures. Still, many questions need to be carefully addressed. An important one is the choice of the linking length used to define the groups. Furthermore, at optical wavelengths, we have considered the LQGs as clouds of points on the celestial sphere and we have split the Huge-LQG into three different branches. This suggests that the Huge-LQG might actually be a complex of large quasar groups defined with a smaller linking length as noted by Park et al. (2015). When we compared the axes of the large quasar groups to the radio polarizations, though, we did not consider such subdivision of the largest quasar groups. It is clear that we have to address the implication on our results of such procedures and, more generally, of the impact of the linking length which is chosen to build the large quasar groups. Such detailed analysis will require dedicated algorithms and statistical methods.

In Chapters 3 and 4, we mentioned that the alignments between the supermassive black hole spins and the LQG axes could provide an explanation for the very large-scale-quasar-polarization-vector alignments (discussed in the first chapters of this work). This would constitute an important result. However, the scales at which the correlations are observed do not match. Indeed, the very large-scale alignments involve distances that are two to four times larger than the diameters of the large quasar groups in which we found correlations. Besides, one may wonder why the optical polarization vectors inside the very large-scale regions of alignments have been reported to be parallel to each other rather than parallel and perpendicular as it is the case inside LQGs. One possibility to reconcile these two kinds of alignments could be selection biases inside the sample of the 355 quasar-optical-polarization measurements (Hutsemékers 2015, private communication). If this hypothesis turns out to be correct, it would imply coherence of the orientations of the LQGs over cosmological scales, at least for some regions of the comoving space.

To conclude, we started this work with an intriguing anisotropy in the distribution of the quasar polarization vectors which challenges the current cosmological paradigm. We confirmed this anomaly and provided evidence for similar alignments at radio wavelengths. We then found correlations linking the quasar polarization vectors and the orientations of large quasar groups. The possibility that the very-large-scale alignments of quasar-polarization vectors and their correlations with the large quasar groups are due to the alignment of the supermassive black hole spin axis with the cosmic web may open a new chapter in the detection and the characterization of the large-scale structures and lead to new questions about the evolution of the Universe.





# Bibliography

- Agarwal N., Aluri P. K., Jain P., Khanna U., Tiwari P., 2012, European Physical Journal C, 72, 1928
- Agarwal N., Kamal A., Jain P., 2011, Phys. Rev. D, 83, 065014
- Amendola L., Appleby S., Bacon D., Baker T., Baldi M., Bartolo N., Blanchard A., Bonvin C., et al., 2013, Living Reviews in Relativity, 16, 6
- Antoniou I., Perivolaropoulos L., 2010, J. Cosmology Astropart. Phys., 12, 12
- Aragón-Calvo M. A., van de Weygaert R., Jones B. J. T., van der Hulst J. M., 2007, ApJ, 655, L5
- Arsham H., 1988, Journal of Applied Statistics, 15, 131
- Battye R. A., Browne I. W. A., Jackson N., 2008, MNRAS, 385, 274
- Berdyugin A., Piirola V., Teerikorpi P., 2014, A&A, 561, A24
- Berriman G., Schmidt G. D., West S. C., Stockman H. S., 1990, ApJS, 74, 869
- Bietenholz M. F., 1986, AJ, 91, 1249
- Borguet B., Hutsemékers D., Letawe G., Letawe Y., Magain P., 2008, A&A, 478, 321
- Brans C. H., 1975, ApJ, 197, 1
- Brotherton M. S., 1996, ApJS, 102, 1
- Catelan P., Theuns T., 1996, MNRAS, 282, 436
- Challinor A. D., Ford M. T., Lasenby A. N., 2000, MNRAS, 312, 159
- Chang Z., Wang S., Li X., 2012, European Physical Journal C, 72, 1838
- Chen S. X., Liu J. S., 1997, Stat. Sin., 7, 875
- Ciarcelluti P., 2012, Modern Physics Letters A, 27, 50221

- Clowes R. G., Campusano L. E., 1991, MNRAS, 249, 218
- Clowes R. G., Campusano L. E., Graham M. J., Söchting I. K., 2012, MNRAS, 419, 556
- Clowes R. G., Harris K. A., Raghunathan S., Campusano L. E., Söchting I. K., Graham M. J., 2013, MNRAS, 429, 2910
- Codis S., Pichon C., Devriendt J., Slyz A., Pogosyan D., Dubois Y., Sousbie T., 2012, MNRAS, 427, 3320
- Codis S., Pichon C., Pogosyan D., 2015, MNRAS, 452, 3369
- Coldwell G. V., Lambas D. G., 2006, MNRAS, 371, 786
- Das S., Jain P., Ralston J. P., Saha R., 2005, J. Cosmology Astropart. Phys., 6, 2
- Decarli R., Labita M., Treves A., Falomo R., 2008, MNRAS, 387, 1237
- di Serego Alighieri S., 2015, International Journal of Modern Physics D, 24, 30016
- DiPompeo M. A., Myers A. D., Hickox R. C., Geach J. E., Holder G., Hainline K. N., Hall S. W., 2015, MNRAS, 446, 3492
- Dubois Y., Pichon C., Welker C., Le Borgne D., Devriendt J., Laigle C., Codis S., Pogosyan D., et al. 2014, MNRAS, 444, 1453
- Dubois Y., Volonteri M., Silk J., 2014, MNRAS, 440, 1590
- Einasto J., Joeveer M., Saar E., 1980, MNRAS, 193, 353
- Einasto M., Liivamägi L. J., Tempel E., Saar E., Tago E., Einasto P., Enkvist I., Einasto J., et al., 2011, ApJ, 736, 51
- Einasto M., Tago E., Lietzen H., Park C., Heinämäki P., Saar E., Song H., Liivamägi L. J., Einasto J., 2014, A&A, 568, A46
- Enea Romano A., Cornejo D., Campusano L. E., 2015, ArXiv e-prints
- Faltenbacher A., Li C., White S. D. M., Jing Y.-P., Shu-DeMao Wang J., 2009, Research in Astronomy and Astrophysics, 9, 41
- Fanidakis N., Macciò A. V., Baugh C. M., Lacey C. G., Frenk C. S., 2013, MNRAS, 436, 315
- Fisher N. I., 1993, Statistical Analysis of Circular Data
- Fisher N. I., Lewis T., Embleton B. J. J., 1993, Statistical Analysis of Spherical Data

- Fossati L., Bagnulo S., Mason E., Landi Degl'Innocenti E., 2007, in Sterken C., ed., *The Future of Photometric, Spectrophotometric and Polarimetric Standardization* Vol. 364 of *Astronomical Society of the Pacific Conference Series*, *Standard Stars for Linear Polarization Observed with FORS1*. p. 503
- Gawiser E., Silk J., 2000, *Phys. Rep.*, 333, 245
- Godłowski W., 2012, *ApJ*, 747, 7
- Granett B. R., Neyrinck M. C., Szapudi I., 2008, *ApJ*, 683, L99
- Hahn O., Teyssier R., Carollo C. M., 2010, *MNRAS*, 405, 274
- Hawley D. L., Peebles P. J. E., 1975, *AJ*, 80, 477
- Heavens A., Peacock J., 1988, *MNRAS*, 232, 339
- Helmboldt J. F., Taylor G. B., Tremblay S., Fassnacht C. D., Walker R. C., Myers S. T., Sjouwerman L. O., Pearson T. J., Readhead A. C. S., Weintraub L., Gehrels N., Romani R. W., Healey S., Michelson P. F., Blandford R. D., Cotter G., 2007, *ApJ*, 658, 203
- Hirata C. M., Seljak U., 2004, *Phys. Rev. D*, 70, 063526
- Hogg D. W., 1999, *ArXiv Astrophysics e-prints*
- Hopkins P. F., Hernquist L., Hayward C. C., Narayanan D., 2012, *MNRAS*, 425, 1121
- Howard S., 1972, *J. Roy. Statist. Soc. Ser. B*, 34, 210
- Huchra J. P., Geller M. J., 1982, *ApJ*, 257, 423
- Hutsemékers D., 1998, *A&A*, 332, 410
- Hutsemékers D., Borguet B., Sluse D., Cabanac R., Lamy H., 2010, *A&A*, 520, L7
- Hutsemékers D., Braibant L., Pelgrims V., Sluse D., 2014, *A&A*, 572, A18
- Hutsemékers D., Cabanac R., Lamy H., Sluse D., 2005, *A&A*, 441, 915
- Hutsemékers D., Lamy H., 2001, *A&A*, 367, 381
- Hutsemékers D., Lamy H., Remy M., 1998, *A&A*, 340, 371
- Hutsemékers D., Payez A., Cabanac R., Lamy H., Sluse D., Borguet B., Cudell J., 2011, in Bastien P., Manset N., Clemens D. P., St-Louis N., eds, *Astronomical Polarimetry 2008: Science from Small to Large Telescopes* Vol. 449 of *Astronomical Society of the Pacific Conference Series*, *Large-Scale Alignments of Quasar Polarization Vectors: Evidence at Cosmological Scales for Very Light Pseudoscalar Particles Mixing with Photons ?*. p. 441

- Impey C. D., Lawrence C. R., Tapia S., 1991, *ApJ*, 375, 46
- Isobe T., Feigelson E. D., Akritas M. G., Babu G. J., 1990, *ApJ*, 364, 104
- Jackson N., Battye R. A., Browne I. W. A., Joshi S., Muxlow T. W. B., Wilkinson P. N., 2007, *MNRAS*, 376, 371
- Jagannathan P., 2014, Master's thesis, Department of physics and astronomy, Calgary, Alberta
- Jagannathan P., Taylor R., 2014, in *Alignments of Radio Sources in the GMRT ELAIS N1 Deep Field Vol. 223 of American Astronomical Society Meeting Abstracts*. p. 150
- Jain P., Narain G., Sarala S., 2004, *MNRAS*, 347, 394
- Jain P., Ralston J. P., 1999, *Mod. Phys. Lett. A*, 14, 417
- Jarvis M. J., McLure R. J., 2006, *MNRAS*, 369, 182
- Joachimi B., Cacciato M., Kitching T. D., Leonard A., Mandelbaum R., Schäfer B. M., Sifón C., Hoekstra H., Kiessling A., Kirk D., Rassat A., 2015, *Space Sci. Rev.*, 193, 1
- Jones B. J. T., van de Weygaert R., Aragón-Calvo M. A., 2010, *MNRAS*, 408, 897
- Joshi S. A., Battye R. A., Browne I. W. A., Jackson N., Muxlow T. W. B., Wilkinson P. N., 2007, *MNRAS*, 380, 162
- Keegstra P. B., Smoot G. F., Gorski K. M., Hinshaw G., Tenorio L., 1997, in Hunt G., Payne H., eds, *Astronomical Data Analysis Software and Systems VI Vol. 125 of Astronomical Society of the Pacific Conference Series, Generalized Spherical Harmonics for All-Sky Polarization Studies*. p. 198
- Kiessling A., Cacciato M., Joachimi B., Kirk D., Kitching T. D., Leonard A., Mandelbaum R., Schäfer B. M., Sifón C., Brown M. L., Rassat A., 2015, *Space Sci. Rev.*, 193, 67
- Kirk D., Brown M. L., Hoekstra H., Joachimi B., Kitching T. D., Mandelbaum R., Sifón C., Cacciato M., Choi A., Kiessling A., Leonard A., Rassat A., Schäfer B. M., 2015, *Space Sci. Rev.*, 193, 139
- Kuvshinova E. V., Panov V. F., 2014, *Russian Physics Journal*, 57, 418
- Lagos C. D. P., Padilla N. D., Cora S. A., 2009, *MNRAS*, 395, 625
- Laigle C., Pichon C., Codis S., Dubois Y., Le Borgne D., Pogosyan D., Devriendt J., Peirani S., et al., 2015, *MNRAS*, 446, 2744
- Lamy H., Hutsemékers D., 2000, *A&AS*, 142, 451

- Land K., Magueijo J., 2007, MNRAS, 378, 153
- Laureijs R., Amiaux J., Arduini S., Auguères J. ., Brinchmann J., Cole R., Cropper M., Dabin C., et al., 2011, ArXiv e-prints [1110.3193]
- Lee J., Pen U.-L., 2000, ApJ, 532, L5
- Lee J., Pen U.-L., 2001, ApJ, 555, 106
- Li C., Jing Y. P., Faltenbacher A., Wang J., 2013, ApJ, 770, L12
- Lietzen H., Heinämäki P., Nurmi P., Liivamägi L. J., Saar E., Tago E., Takalo L. O., Einasto M., 2011, A&A, 535, A21
- Lietzen H., Heinämäki P., Nurmi P., Tago E., Saar E., Liivamägi J., Tempel E., Einasto M., et al., 2009, A&A, 501, 145
- Lister M. L., 2001, ApJ, 562, 208
- Marin F., 2014, MNRAS, 441, 551
- Masiero J., Hodapp K., Harrington D., Lin H., 2007, PASP, 119, 1126
- McKinney J. C., Tchekhovskoy A., Blandford R. D., 2013, Science, 339, 49
- Nadathur S., 2013, MNRAS, 434, 398
- Naghizadeh-Khouei J., Clarke D., 1993, A&A, 274, 968
- Oppermann N., Junklewitz H., Greiner M., Enßlin T. A., Akahori T., Carretti E., Gaensler B. M., Goobar A., Harvey-Smith L., Johnston-Hollitt M., Pratley L., Schnitzeler D. H. F. M., Stil J. M., Vacca V., 2015, A&A, 575, A118
- Padmanabhan N., Hirata C. M., Seljak U., Schlegel D. J., Brinkmann J., Schneider D. P., 2005, Phys. Rev. D, 72, 043525
- Park C., Song H., Einasto M., Lietzen H., Heinamaki P., 2015, Journal of Korean Astronomical Society, 48, 75
- Patat F., Romaniello M., 2006, PASP, 118, 146
- Payez A., Cudell J. R., Hutsemékers D., 2008, in Cugon J., Lansberg J.-P., Matagne N., eds, American Institute of Physics Conference Series Vol. 1038 of American Institute of Physics Conference Series, Axions and polarisation of quasars. pp 211–219
- Payez A., Cudell J. R., Hutsemékers D., 2011, Phys. Rev. D, 84, 085029
- Peebles P. J. E., 1993, Principles of Physical Cosmology

- Pelgrims V., 2014, in IAU Symposium Vol. 306 of IAU Symposium, A new test of uniformity for object orientations in astronomy. pp 276–278
- Pelgrims V., Cudell J. R., 2014, MNRAS, 442, 1239
- Pelgrims V., Hutsemékers D., 2015, MNRAS, 450, 4161
- Pelgrims V., Hutsemékers D., 2016, ArXiv e-prints [1604.03937],  
(A&A accepted : <http://dx.doi.org/10.1051/0004-6361/201526979>)
- Pen U.-L., Lee J., Seljak U., 2000, ApJ, 543, L107
- Planck Collaboration Int. XIX 2015, A&A, 576, A104
- Planck Collaboration XVI 2014, A&A, 571, A16
- Planck Collaboration XXI 2015, ArXiv e-prints [1502.01595]
- Planck Collaboration XXIII 2014, A&A, 571, A23
- Pollack L. K., Taylor G. B., Zavala R. T., 2003, ApJ, 589, 733
- Poltis R., Stojkovic D., 2010, Phys. Rev. Lett., 105, 161301
- Press W. H., Teukolsky S. A., Vetterling W. T., Flannery B. P., 1992, Numerical recipes in C. The art of scientific computing
- Ralston J. P., Jain P., 2004, International Journal of Modern Physics D, 13, 1857
- Rusk R., 1990, J. R. Astron. Soc. Can., 84, 199
- Rusk R., Seaquist E. R., 1985, ApJ, 90, 30
- Saikia D. J., Salter C. J., 1988, ARA&A, 26, 93
- Schneider D. P., Richards G. T., Hall P. B., Strauss M. A., Anderson S. F., Boroson T. A., Ross N. P., Shen Y., et al., 2010, AJ, 139, 2360
- Serkowski K., 1958, Acta Astron., 8, 135
- Shen Y., Richards G. T., Strauss M. A., Hall P. B., Schneider D. P., Snedden S., Bizyaev D., Brewington H., et al., 2011, ApJS, 194, 45
- Shurtleff R., 2013, ArXiv e-prints [1311.6118]
- Shurtleff R., 2014, ArXiv e-prints [1408.2514]
- Sluse D., Hutsemékers D., Lamy H., Cabanac R., Quintana H., 2005, A&A, 433, 757

- Smith J. E., Robinson A., Alexander D. M., Young S., Axon D. J., Corbett E. A., 2004, *MNRAS*, 350, 140
- Söchting I. K., Clowes R. G., Campusano L. E., 2002, *MNRAS*, 331, 569
- Söchting I. K., Clowes R. G., Campusano L. E., 2004, *MNRAS*, 347, 1241
- Taylor A. R., Jagannathan P., 2016, *MNRAS*
- Tegmark M., de Oliveira-Costa A., Hamilton A. J., 2003, *Phys. Rev. D*, 68, 123523
- Tempel E., Libeskind N. I., 2013, *ApJ*, 775, L42
- Tiwari P., Jain P., 2013, *International Journal of Modern Physics D*, 22, 50089
- Tiwari P., Jain P., 2015, *ArXiv e-prints* [1505.00779]
- Trowland H. E., Lewis G. F., Bland-Hawthorn J., 2013, *ApJ*, 762, 72
- Urban F. R., Zhitnitsky A. R., 2010, *Phys. Rev. D*, 82, 043524
- Vollmer F. W., 1995, *Computers and Geosciences*, 21, 31
- Wands D., Piattella O. F., Casarini L., 2015, *ArXiv e-prints* [1504.06335]
- Wardle J. F. C., 2013, in *European Physical Journal Web of Conferences Vol. 61 of European Physical Journal Web of Conferences, Magnetic fields and polarization in AGN jets.* p. 6001
- West M. J., 1994, *MNRAS*, 268, 79
- West M. J., 1999, in Röttgering H. J. A., Best P. N., Lehnert M. D., eds, *The Most Distant Radio Galaxies The Formation of High-Redshift Radio Galaxies: Clues from the Low-Redshift Universe.* p. 365
- White S. D. M., 1984, *ApJ*, 286, 38
- Wills B. J., Browne I. W. A., 1986, *ApJ*, 302, 56
- Yadav J. K., Bagla J. S., Khandai N., 2010, *MNRAS*, 405, 2009
- Zavala R. T., Taylor G. B., 2004, *ApJ*, 612, 749
- Zhang Y., Yang X., Wang H., Wang L., Mo H. J., van den Bosch F. C., 2013, *ApJ*, 779, 160